NOVEL SYNTHETIC TECHNIQUES FOR Fe(II) TRIAZOLE SPIN CROSSOVER MATERIALS

Georgina A. Conway

MSc

School of Physical Science
University of Kent

Acknowledgements

I would like to thank Dr. Helena J. Shepherd for the opportunity to undertake this new and exciting research. I am extremely grateful for the continued support provided throughout and the limitless patience and understanding. Research aside, this could not have been completed without Helena's help, encouragement and believing in me when I did not believe in myself. I am enormously grateful and appreciative to have had such a great supervisor. I would like to thank everyone in the Shepherd group, specifically Jed, for their help and support in the lab. Thank you to my friends in SPS for keeping me sane on a regular basis and being so supportive. I would also like to thank my partner, Kristina for all of her love and support throughout my master's and university life. Lastly, I would like to thank my wonderful parents of which without none of this would have been possible. Truly, thank you.

Abstract

This thesis is a preliminary investigation into the synthesis of Fe(II) triazole spin crossover compounds (SCO) using novel techniques that are easily scalable for the production of large quantities. These techniques are the *direct-contact* synthesis of solid reagents mixed under ambient conditions and *thin-film* synthesis via in situ airbrushing. Three compounds [Fe(atrz)3]SO4 (**1**), [Fe(Htrz)2(trz)](BF4) (**2**), and [Fe(atrz)3](BF4)2 (**3**) were synthesized using these novel techniques and analyzed and characterized with regard to their respective traditional solution-state synthesis. Analysis shows that for **1**, the *direct-contact* and *thin-film* methods successfully synthesize the same compound as the traditional synthetic method yielding very similar SCO properties. Compound **2** is known to exist in a variety of forms, and it is likely that the *direct-contact* method yields a multi-phase sample of hydrated forms that potentially dehydrate upon heating. The *thin-film* method likely synthesizes the same compound as the solution-state with very similar SCO properties. The *direct-contact* method of compound **3** synthesises the β polymorph. More analysis is required to determine with accuracy the form of the thin-film method and its corresponding SCO properties. The overall results demonstrate that novel *direct-contact* and *thin-film* methods are viable techniques for synthesizing SCO materials on a large-scale.

Table of Contents

1. Introduction

Spin crossover (SCO) is a phenomena in which a metal ion can transition from the low-spin electronic state (LS) to the high-spin electronic state (HS) upon application of an external stimuli such as temperature, light, pressure, irradiation and pressure.[1] The most common way of "switching" these materials, and the main focus of this thesis, is temperature. Transition metals with an electronic configuration of d^4-d^7 in an octahedral coordination can experience this phenomenon. An octahedral field is required as a free metal ion's degenerate 3d orbitals are split into two sub-levels, as seen in *Figure 1*. A lower energy t_{2g} non-bonding orbital comprising of degenerated orbitals d_{xy}, d_{xz}, d_{yz} and a higher energy e_g antibonding orbital comprised of degenerate orbitals $d_{x^2-y^2}$ and d_{z^2} that are directed towards the ligand.

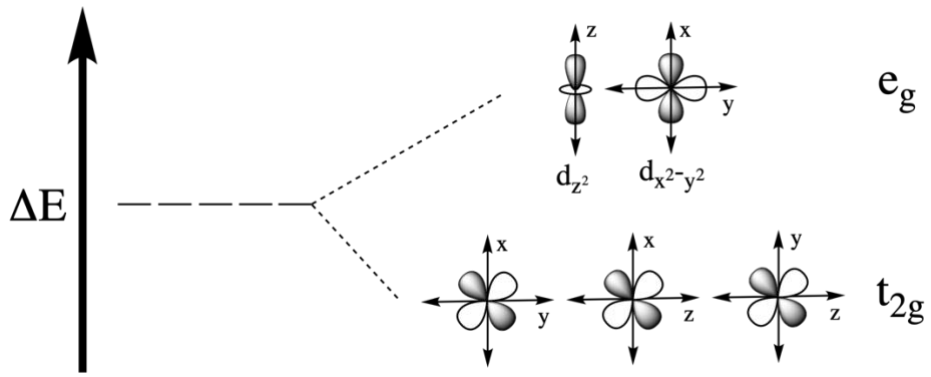

Figure 1: The splitting of the degenerate d-orbitals into lower energy t_{2g} and higher energy e_g sublevels with their respective orbitals.

The ligand field splitting energy is the energy difference between the t_{2g} and e_g orbitals. In the LS state the ligand field splitting energy is considerably greater than the electron pairing energy and thus the lower orbitals are populated first resulting in maximum spin multiplicity in the t_{2g} orbitals, shown in *Figure 2*. Alternatively, for an ion in the HS state, the ligand field energy is significantly less than the electron pairing energy and therefore the higher energy orbitals are populated resulting in minimum spin multiplicity. Upon switching from LS → HS, the electrons move from the non-bonding t_{2g} orbitals to the antibonding e_g orbitals inevitably resulting in significant changes to the structural, magnetic and optical properties of the material. From a thermodynamic standpoint, the LS state is a lower energy and more ordered state and is therefore favored enthalpically as opposed to the higher energy, more disordered entropically favored HS state. The SCO transition is a competition between electronic and vibrational enthalpic and entropic contributions.[1] The electronic contribution accounts for change in electronic degeneracy between the HS and the LS states. The vibrational contribution accounts for changes within the vibrational levels of the molecule upon transition and is mostly a result of the population of the antibonding e_g orbital and therefore the expansion of the coordination sphere.

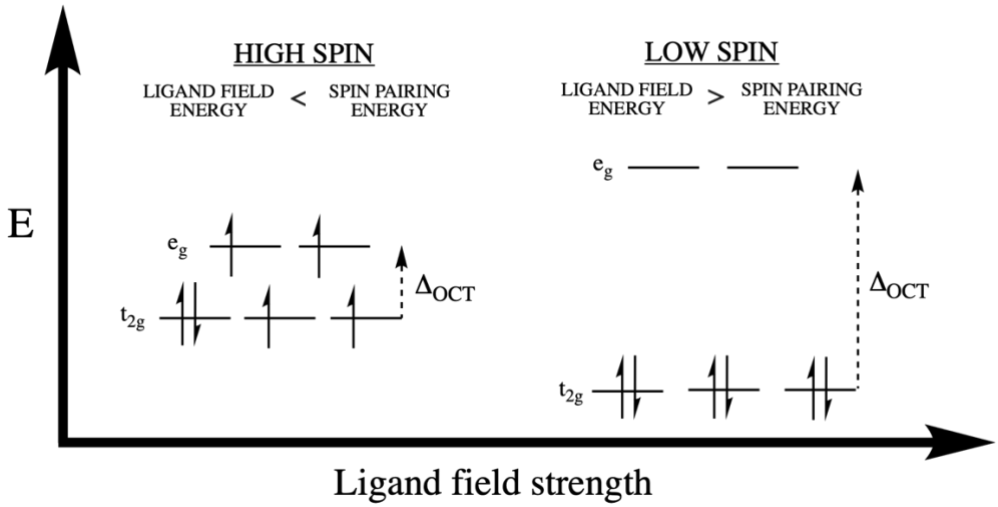

Figure 2: Diagram of LS and HS states and their relative orbital energies in relation to ligand field strength.

It is this vibrational entropy difference between the LS state and the HS state that is considered to be the main driving force of thermal spin crossover.[2] The temperature at which crossover occurs is thus the ratio of the overall enthalpic and entropic contributions. The SCO transition temperature, $T_{1/2}$ is defined as the temperature at which the LS and HS fractions are equal, shown in *Figure 3*.[3]

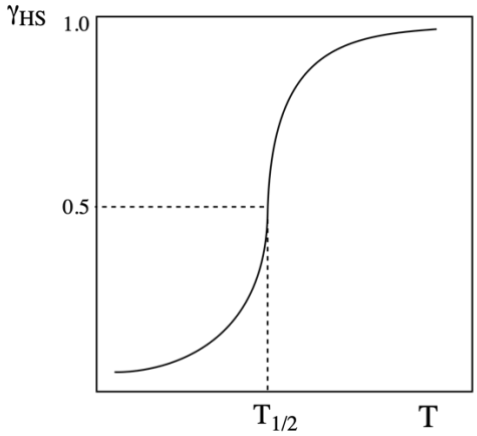

Figure 3: A typical SCO curve depicting the definition of $T_{1/2}$ as the temperature value when LS and HS fractions are equal.

SCO transition properties are highly sensitive to small changes in the ligand field energy and therefore the transition profile of an SCO compound can differ greatly depending on lattice properties.[4] The most significant determining factor of a transition is the overall combination of both the long and short range elastic interactions throughout a lattice known as cooperativity.[5] The degree of cooperativity can be defined as the extent to which consequences, most notably structural changes, of spin change are propagated to neighboring molecules through these elastic interactions and thus throughout the system.[4] The population of the antibonding e_g orbital in the HS state results in a weaker, longer metal-ligand bond, thus increasing the molecular volume and distorting the octahedra of the HS state, as seen in *Figure 4*. When a molecule is surrounded by neighboring molecules in an opposite electronic spin state with structural differences in volume

and shape, a tension is generated. This change in the metal-ligand bond distance acts as a 'defect' and is communicated throughout the system via electron-phonon coupling.[3] The higher the elastic strain field, the more tension builds up and propagates over the system and thus the higher the degree of cooperativity.

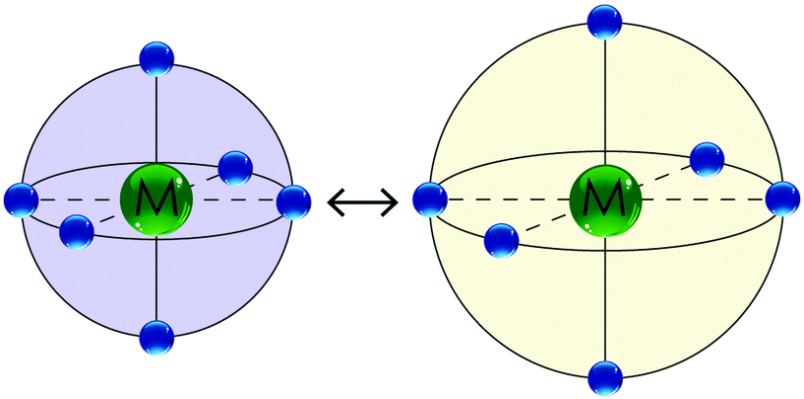

Figure 4: The LS electronic state (left) has a smaller molecular volume due to stronger and shorter bonds. The population of the antibonding orbital in the HS electronic state leads to weaker, longer bonds which increases the volume by approximately 10%. This schematic has been reproduced from reference.[6]

The complex nature of the intermolecular interactions and its fundamental dependence on the type of molecules and their properties results in a vast array of transitions. The general SCO profiles can be represented graphically on a plot of molar fraction in the HS state (γ_{HS}) vs temperature as seen in Figure *5*.[3] The steepness of the curve represents the nature of the transition, thus is indicative of the degree of cooperativity. The higher the degree of cooperativity, the more effective the propagation and thus the transition occurs over a narrower range of temperature, known as an abrupt transition. Less cooperativity within the lattice results in a gradual transition occurring over a wider temperature range. SCO compounds with a high degree of cooperativity can exhibit thermal hysteresis, and thus bistability *i.e.* the compound exists in two different stable electronic states within a certain temperature range.[6] The origins of hysteresis could be highly effective cooperativity that strongly propagates structural changes to neighboring metal ions through strong covalent bonds, hydrogen bonding, van der Waals forces, or there could be a phase change upon transition.[4,6]

These two electronic states have different optical, magnetic, vibrational and structural properties. Fe^{2+} is arguably the most studied metal ion in SCO compounds because of its d^6 electron configuration. This is of particular interest from a magnetic perspective as it involves a transition from the diamagnetic LS state to the paramagnetic HS state. This is the greatest magnetic response difference and thus makes Fe^{2+} SCO compounds highly attractive. A ligand family that is widely used with Fe^{2+} that forms a myriad of SCO compounds are the triazoles.[7]

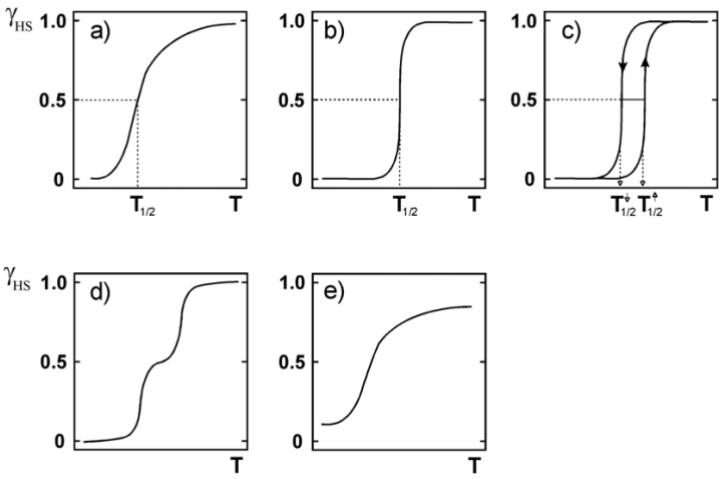

Figure 5: Graphical representation of the general profiles of SCO transition curves where γ_{HS} represents the molar high spin fraction as a function of temperature: **a)** gradual; **b)** abrupt; **c)** hysteresis; **d)** two-step; **e)** incomplete. These graphs are reproduced from reference.[4]

1.2. Triazoles

1.2.1. Synthesis & Structure

Triazoles are five-membered aromatic rings, shown in *Figure 6*, with three N atoms that provide a ligand field strength about the Fe^{2+} ion that gives rise to a wide range of SCO complexes with varying SCO properties that transition at or around ambient temperatures.[8] Triazole based SCO compounds with the general formula $[Fe(Rtrz)_3][A_2].xH_2O$ where Rtrz = 4-substituted-1,2,4-triazole and A = monovalent anion, are the most commonly studied.[7]

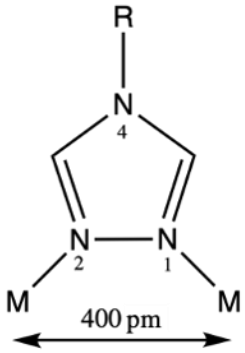

Figure 6: 4-substituted triazole attached to metal ligands in the 1,2-bridging mode with a distance of 400 pm between each ion.

The synthesis of these compounds is straightforward and highly efficient with favorable yields as the reagents readily react. The most common way of synthesizing these materials is to react an FeA_x hydrate with a triazole ligand in a 1:3 ratio under common conditions such as water or methanol. For the triazole family this typically yields a purple/pink complex that is SCO active that becomes white upon conversion to the HS state. A significant advantage to these SCO compounds is the customizability of both reagents. Not only can the triazole be modified at the 4 position, but the monovalent salt can also be substituted. This generates a family of triazole

compounds with the ability to be combined with many metal salts, creating countless possibilities of different compounds with varying SCO potential. This vastness of variety and chemical flexibility facilitates the potential tuneability of SCO properties, making them highly attractive compounds.[7]

Triazoles form one-dimensional (1D) coordination chains with the Fe^{2+} ion connecting to three N^1-N^2-triazole bridges, shown in *Figure 7*.[3,7] These N^1-N^2 linkages are very short and rigid and thus are ideal to propagate cooperativity throughout the network.[9] This results in the Fe^{2+} ions being only 400 pm apart and thus to reduce the electrostatic repulsion between these ions, triple bridges form.[7] Therefore each Fe^{2+} ion within the coordination chain is in an octahedral environment. The 1,2-bridging mode is optimal as this creates M-N-N angles of 125.26°. The significance of this angle is that it is very similar to the 126° exocyclic free donor electron pair angle of a 5 membered ring which is low energy and highly stabilized. This results in minimal to no ring strain and thus formation is highly favorable resulting in high yields.

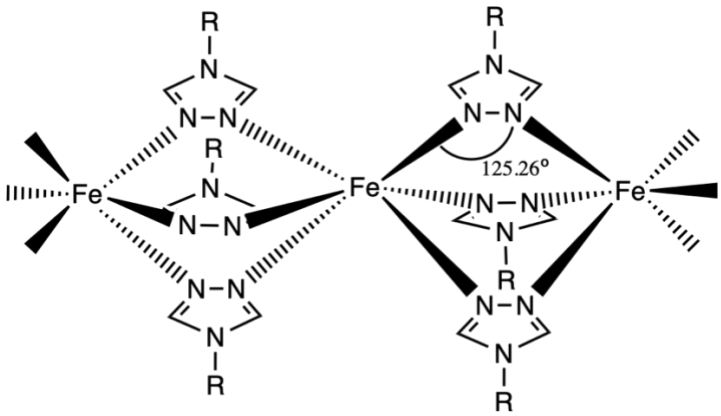

Figure 7: Propagation of 1D chains of Fe^{2+} ions triply bridged to R-1,2,4-triazole ligands displaying the optimal M-N-N angle.

The stabilization also drives the chains to propagate in long 1D chains with the terminus completed by solvent molecules. The counter-anions sit between these 1D chains and can form hydrogen bonds with the triazole ligands which can have a large impact on the SCO properties. Chains are connected via hydrogen bonds of adjacent groups and/or adjacent triazoles, as well as hydrogen bonding through counteranions resulting in strong interchain interactions. The strength of these interchain connections will have a profound effect on the cooperative nature of these complexes and thus the SCO properties of the material. The chain structure reportedly remains intact and does not coil and cause crystallographic phase transitions upon LS $\rightarrow$ HS transition.[9,10] As these chains propagate in 1D, it is imperative that the 4-substituent on the triazole is not bulky as this can disrupt the chain and prevent formation.[7] This can be overcome by having the bulky substitute on a long alkyl chain far enough away to not hinder chain propagation.

The polymeric chains are usually insoluble, and the favorable reaction means that precipitation is fast. This results in poor crystallinity and therefore these compounds are generally

isolated as microcrystalline powders. Consequentially, structural information is limited as single crystal analysis is not available. Structural information has been obtained by EXAF (Extended X-ray Absorption Fine Structure), WAXS (wide angle X-ray scattering), powder diffraction, and Raman spectroscopy.

1.2.2. SCO Properties in $[Fe(Rtrz)_3][A_2]$ Complexes

As discussed in **Section 1**, Fe^{2+} compounds also exhibit the maximum change in magnetic response converting from the diamagnetic LS state ($t_{2g}^6e_g^0$) to the paramagnetic HS state ($t_{2g}^4e_g^2$). This leads to structural consequences upon transition that is a direct result of the population of the antibonding e_g orbital in the HS state. EXAF studies show that upon SCO, the Fe-N bond length increases by approximately 0.18 Å due to bond weakening, thus distorting the FeN_6 octahedra resulting in thermal expansion across the entire sample.[11] The SCO transitions of $[Fe(Rtrz)_3][A_2]$ are generally accompanied by a thermochromic effect.[12] Thermochromism can be attributed to the $^1A_{1g} \rightarrow {}^1T_{1g}$ d-d transition at 520 nm in the visible region in the LS state and the $^5T_{2g} \rightarrow {}^5E_g$ d-d transition at 800 nm in the near infrared region in the HS state.[13] This results in a distinct pink/purple LS complex that transitions to a white HS complex upon SCO. The rate at which these SCO properties are propagated throughout the lattice depends on the cooperativity of the complex. As mentioned previously, the stiff, short triazole ligands coupled with the interactions between chains allow for effective propagation of across the lattice. The degree of cooperativity and thus rate of propagation is highly dependent on the R substituent, anion and the degree of hydration.[7] There are typically four SCO profiles that are observed by this family of compounds.

The combination of SCO features of these compounds *i.e.* thermochromism, magnetism, and structural properties, make them highly attractive for application purposes such as molecular switches, chemical sensors, displays, memory and data storage.

1.3. Nanoparticles, Thin Films & Applications

1.3.1. Nanoparticles

The development of functional nanomaterials has been a vital component in the rapid advancement of several technological fields. However, as technology continues to advance, the smaller and smaller these systems become.[14] This has led to a surge in research on the development of nanostructures and thin films.[15] There are two fundamental approaches in the development of nanoparticles. The 'top down' approach has been the main fabrication method thus far which involves the miniaturization of larger particles into progressively smaller and smaller particles.[16] This is achieved in a multitude of ways such as milling,[17] grinding[18] and sieving.[19] These techniques have generally been considered to be unideal for SCO compounds as the stress exerted by these procedures might have irreversible effects on the SCO properties.[20,21] This is attributed to introducing more defects into the crystal structure thus reducing the

coherent domain leading to a decrease in cooperativity. The mechanosynthesis of SCO complexes was first investigated by Askew *et al.*[22] The SCO complexes were synthesized via grinding the reagents in a mortar and pestle for 5 minutes. The resulting SCO complexes displayed comparable properties to that of their corresponding bulk materials. This rapid synthetic method could potentially be the gateway to obtaining novel compounds or attaining new polymorphs of existing SCO compounds.

As these systems are relentlessly shrinking at a rapid pace, the ultimate size is generally considered to be at a molecular or atomic level. This leads to the direct synthesis of molecular based systems via the controlled formation of particles, also known as the 'bottom up' approach. This approach can be divided into three principal methods — hard templating, soft templating and template-free synthesis.[23] Common hard templates used to synthesize nanoparticles include silica[24] and MOFs.[25] This technique is advantageous as the size and shape of particles can be directly controlled. However, these methods are generally complex and lead to low yields and the template potentially interferes with SCO properties. Soft template methods include reverse micelle,[26,27] vesicles,[28] and block copolymer micelles.[29] These procedures allow for control of nucleation and growth of nanoparticles however the presence of surfactant/matrix can dilute the SCO compound thus modifying the SCO properties. Template-free synthesis of SCO nanoparticles has therefore become increasingly attractive. Daro *et al.*[30] recently reported the synthesis of SCO nanoparticles via spray-drying that led to predominantly spherical nanoparticles as opposed to their typical rod-like morphologies. Other template-free synthetic methods have been reported by way of homogeneous mediums[31] and millifluidics.[32]

There have been restraints that have slowed the development of using SCO materials in nanotechnology.[33] As the SCO properties of a material are largely determined on the degree of cooperativity throughout the lattice, it is logical to assume that these properties will alter upon size reduction and a change in crystallinity. The size reduction effects on SCO properties was investigated by Felix *et al.*[34] which highlighted that the effects of SCO properties in nanoparticles are dependent on surface phenomena *i.e)* surface area to volume ratios and surface interactions. Whilst many studies of SCO thin films exhibited loss of hysteresis, this study showed that hysteresis can be reestablished when nanoparticles are < 5-10 nm.[33,34] This validated the potential for thin films to be fabricated with comparable properties to that of the bulk sample. The following sections introduce several current methods used in the fabrication of thin films.

1.3.2. Thin Films

For SCO materials to be suitable for technological applications they must be able to be deposited onto surfaces whilst retaining properties.[16] The development of stable, homogenous and reproducible thin films is thus critical for the evolution of functionality of SCO materials. Since a fundamental characteristic of these compounds is their optical properties, it is imperative that

the fabricated thin films are transparent.[35] Thin film growth has been studied using techniques such as Langmuir-Blodgett,[36] spin coating,[37] drop casting,[38] multi-layer sequential growth,[39] and sublimation.[40]

1.3.2.1. Langmuir-Blodgett

The Langmuir-Blodgett (LB) technique was the first molecular-level method used to synthesize thin films.[41] The process requires an amphiphilic compound dissolved in a volatile solvent dispersed at the air/water interphase. The molecule arranges itself with the non-polar aliphatic chains facing upright away from the water and the polar moiety submerged. Adjustable barriers on either side are used to alter the area of the interphase, thus condensing and ordering the amphiphilic molecules into a monolayer on the surface. To produce a film, a substrate is immersed through the interphase and into the water. Upon removal, the monolayer adheres to the substrate and additional layers are applied by subsequent dips.

The first manufacturing of an SCO thin film was via the LB technique and reported by Soyer *et al.*[39] They reported the successful synthesis of an $Fe(II)L_2(NCS)_2$ (where L is a substituted bipyridine) LB film. The subphase used was a formamide/water mixture as these molecules are known to decompose slightly when in contact with water due to instability. Analysis determined that spin conversion was still present via the same process as that of the solid state. However, analysis also shows incomplete conversion and suppression of SCO that is most likely a consequence of the highly structured molecules separated by long alkyl chains that potentially interfere with the propagation of SCO. This in turn will reduce cooperativity and thus alter the SCO properties of LB films in comparison to their respective powders. This study highlighted the sensitivity of the environment and organization on the completeness of SCO and the cooperativity.

Roubeau *et al.*[42] reportedly synthesized iron(II) triazole LB thin films with SCO transitions at ambient temperatures. More recently, Kitchen *et al.*[43] successfully synthesized a stable SCO LB film of an iron(II) triazole complex at the air/water interphase. This film exhibited a gradual transition close to room temperature at 290 K. These studies show promise for the potential formation of homogenous, stable SCO thin films with precise thicknesses. Nevertheless, the restriction of exclusively using amphiphilic molecules limits the scope for this method and thus this technique is not a comprehensive way to synthesize SCO thin films.

1.3.2.2. Spin Coating & Drop Casting

Spin coating is the most common and accessible method of synthesizing thin films of functional materials in a laboratory setting.[15] This technique is relatively straightforward and consists of depositing a drop of solution onto a rotating substrate, as seen in *Figure 8*. The difficulty with this method is the ability to achieve thin films with desired thickness and

morphology. Although this is a simple technique, there are numerous factors contributing to the quality of the thin film.[44] These factors include the concentration of the polymer in solution, rate of solvent evaporation, viscosity of fluid, volume of the fluid deposited, spinning time, spinning speed and spinning acceleration.

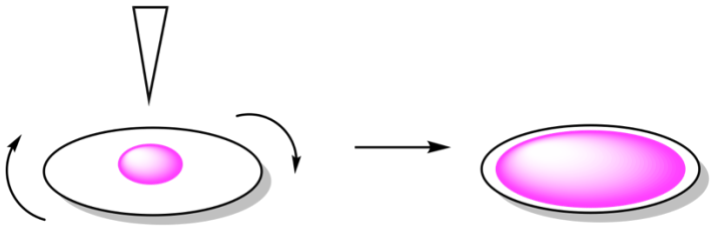

Figure 8: Schematic depicting the spin coating process of synthesizing thin films.

Matsuda *et al.*[45] successfully synthesized a homogenous thin film of [Fe (2,6-di(pyrazol-1-yl)pyridine)$_2$](BF4)$_2$ on a glass substrate with reproducible SCO phenomena using the spin coating method. In the solid state, this compound exhibits an abrupt transition centered at 259 K with a hysteresis of 3 K. The thin film displays comparable properties with a more gradual transition around 260 K. This is a particularly significant study as it demonstrated the potential to synthesize thin films in an easy, accessible manner with SCO properties analogous to their solid state. Tissot *et al.*[46] also reported the precipitation of SCO nanoparticles by spin coating a doped gel which led to the fabrication of transparent thin films. The properties of SCO of the thin film were retained although exhibited a more gradual transition curve.

Another example of SCO thin films being synthesized via spin coating was by Felix *et al.*[47] This study demonstrates the fabrication of a smooth, homogenous [Fe(4-heptyl-1,2,3-triazole)$_3$](tosylate)$_2$ thin film onto a glass substrate. What was also exciting about this study is the demonstration of a technique to detect SCO phenomena in nanometric thin films by utilizing surface plasmon polaritons. Essentially, the refractive index of an SCO active compound changes, primarily because of the change in volume that occurs upon transition. This change in refractive index can be used to monitor SCO occurrences in nanometric thin films potentially down to 5 nm.

Even more recently, Hochdörffer *et al.*[48] reported the synthesis of a [Fe(Htrz)$_2$(trz)](BF$_4$) thin film via the spin coating method on a silica substrate. The thin film demonstrated analogous SCO properties to that of the corresponding bulk sample. The ease and the accessibility of this technique makes it largely appealing; however, the lack of control limits the fabrication of thin films with precise specifications. This technique is also very restricted in the manufacturing of large-scale thin films and particularly thin films on surfaces that are not flat.

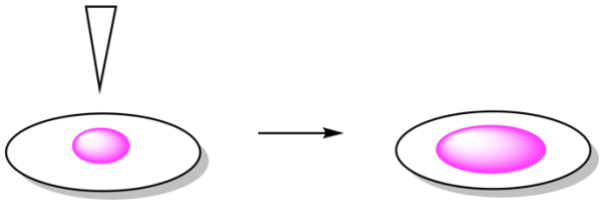

Figure 9: Schematic for the drop casting method of synthesizing thin films.

An even simpler method of manufacturing thin films is drop casting which involves depositing a solution onto a substrate, seen in *Figure 9*. [15] The volatile solvent then evaporates leaving the desired solute behind adhered to the substrate. Kuroiwa *et al.*[49] investigated the synthesis of lipophilic Fe^{2+} 1,2,4-triazole thin films by using a unique supramolecular approach. This produced films that exhibited lethargic SCO properties with no hysteresis. This was most likely a consequence of the long alkyl chains disrupting the propagation of SCO phenomena. However interestingly, the same complexes with alcohol groups present on the alkyl chains resulted in an abrupt transition with bistability. This is most likely a result of the increased interactions throughout the chains via hydrogen bonding of the OH groups and an increase in Van der Waals forces which in turn increases propagation and thus cooperativity throughout perpetuating the SCO phenomena. Although this technique of drop casting is very simple, it usually leads to thick, inhomogeneous films and thus this technique is most useful for preliminary tests and not necessarily thin films fit for technological application.

1.3.2.3. Multi-Layer Sequencing

The previously mentioned thin film methods all involve synthesis *ex situ* and then deposited onto a substrate. The multi-layer sequential method involves synthesizing the SCO compound *in situ* on the substrate. Nakomoto *et al.*[35] first introduced this technique in 2003 when they reported synthesizing the first $[Fe(R\text{-}trz)_3]$-Nafion film, (where R = H or NH_2) with an ambient SCO temperature. This method exploits the chemical structure of Nafion and the presence of SO_3^- that can act as suitable anions. In order to achieve this, Nafion was submerged in aqueous $FeSO_4$ resulting in the Fe^{2+} ions being absorbed. The Nafion with Fe^{2+} bound was then immersed in a solution of R-trz which led to the formation of $[Fe(R\text{-}trz)_3]$ attached to the Nafion backbone, courtesy of the SO_3^- anions. The final film was transparent and exhibited an SCO transition about 260 K. Prospective complications with Nafion is that the material is inherently inhomogeneous and so will most likely result in inhomogeneous thin films with an unpredictable morphology.[15,50]

Another study into the multi-layer sequencing synthesis of thin films was conducted by S. Cobo *et al.*[51] which reports the successful synthesis of [Fe- (pyrazine){$M(CN)_4$}], where M = Ni, Pd, or Pt, thin films through subsequent dipping of the M substrate into $Fe(BF_4)_2 \cdot 6H_2O$ and pyrazine solutions, shown in *Figure 10*. The thin films displayed hysteretic spin crossover that occurred around room temperature.

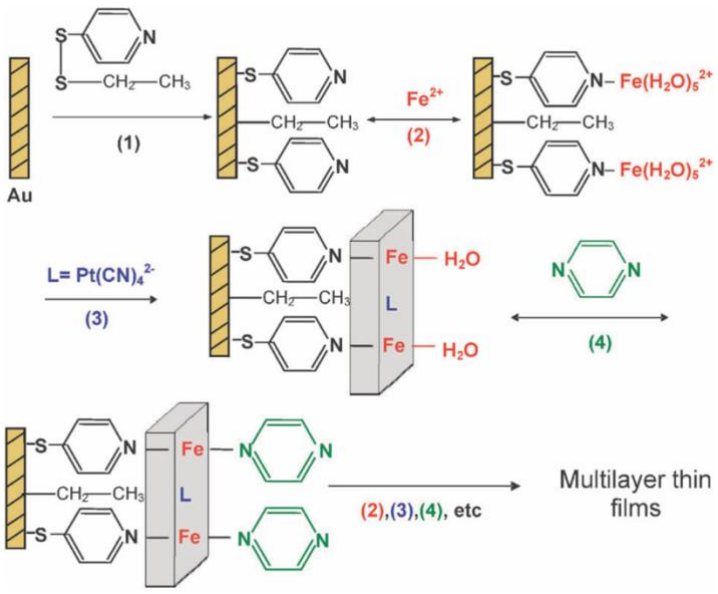

Figure 10: Schematic illustrating the multi-layer sequential approach conducted by Bartual-Murgui et al. This figure has been reproduced from the reference.[52]

The potential of synthesizing thin films this way was further studied by the same group by Bartual-Murgui *et al.*[52] This focused primarily on the optimization of layer by layer deposition of {Fe(pyrazine)[Pt(CN)4]} onto a gold plated silicon wafer. To functionalize the gold substrate, a thiol monolayer was attached as an 'anchor' and then dipped into a solution of $Fe^{2+}[Pt(CN)_4]^{2-}$ and then subsequently dipped into a pyrazine solution. This was repeated several times until desired thickness is reached. Atomic force spectroscopy shows smooth topology of the resultant thin films. Surface plasmon resonance was used to accurately determine the thickness of films. This study demonstrated the ability to fabricate thin films of any desired thickness to very precise measurements.

1.4. Applications

It is evident that there are many properties that spin crossover thin films possess that make them highly appealing for application purposes such as molecular switches, data storage and display devices.[16] The ability to exist in two different electronic spin states (LS/HS) makes these complexes eligible as potential molecular switches. Information can be associated with the LS and HS states and thus when an input is applied (external stimuli such as temperature or light etc.) the change in volume or magnetism can produce an output. This can be thought of as an 'ON/OFF' switch or 0/1 in binary code.[6] This means that it is possible for SCO complexes to be used as a logic operator and thus can be used in data processing or programming.[16] It is also important to note that these complexes generally do not exhibit any fatigue after consecutive switching. This means that they can 'execute a function' repeatedly without deteriorating performance which is advantageous for application potential.

The magnetic and bistability potential of SCO compounds makes them highly prospective for memory applications, such as data storage. Hysteretic compounds have two transition temperatures, the heating $T_{1/2}\uparrow$ and the cooling $T_{1/2}\downarrow$, that depends on the cooperativity of the compound, as previously discussed in **Section 1**. The spin state within these temperatures is determined by a 'memory effect' and is dependent upon the spin state when entering the temperature range.[6] For memory applications it is thus especially desirable to have a large hysteresis within ambient temperature as this will prevent natural changes, *i.e.* weather or temperature of the operating device, from having a profound effect on the application.

The first SCO display device was reported by Kahn *et al.*[13] and fabricated using iron-triazole complexes. The requirements for the SCO complex state that the transition temperature must be abrupt and occur below 5 K, exhibit a wide hysteresis with a $T_{1/2}\uparrow$ and $T_{1/2}\downarrow$ around the devices operating temperature, display a prominent color change upon switching between LS and HS, and be chemically stable over a long period of time without signs of deterioration or fatigue upon successive thermal cycles. The device consisted of an SCO complex in resin that was deposited as an ink onto a substrate consisting of alumina with resisting dots and electrodes organized into a pattern.[13,16] Prior to writing, the whole display is purple as the complex is in the LS electronic state. Upon writing, the dots became heated thus switching the area occupied by the dots into the HS electronic state and thus white when $T_{1/2}\uparrow$ is reached or surpassed. The pattern is retained as long as the temperature remains within the hysteresis. To clear the pattern, or erase the information, the temperature needs to decrease below $T_{1/2}\downarrow$ in order to transition back into the purple, LS state. This study demonstrated practically the potential of SCO complexes as display devices.

The observable thermochromic effect displayed in these compounds means that they could act as potential thermal sensors. Once a certain temperature (*i.e.,* $T_{1/2}$) has been reached, the SCO complex (sensor) would then display an optical change indicating a temperature has been exceeded. This could prove particularly useful for large reactor vessels that are sensitive to temperature fluctuations. The coating of a vessel with an SCO thermal sensor could thus optically indicate that a temperature has been reached instantaneously. The requirements for an SCO complex suitable for this application would be a very abrupt, irreversible transition. Other sensory applications of SCO materials have been investigated. Ohba *et al.*[53] reported the synthesis of a microporous framework, SCO–PCP $\{Fe(pz)[Pt(CN)_4]\}$ and showed that when guest molecules populate the cavities of the framework a spin transition is induced. This transition is reversible and is controlled by the adsorption and desorption of the guest molecules, in this case CS_2 and benzene. The principle of utilizing SCO complexes as chemical sensors was further developed by Bartual-Murgui *et al.*[54] This study demonstrated the synthesis of micro-patterned gratings of an SCO/metal-organic framework (MOF) complex with sensing capabilities. When guest molecules (typically volatile organic compounds), are absorbed by the framework it induces a change in spin

state, and thus a change in the refractive index value which allows the transitions to be monitored. Another interesting property of these frameworks is their selectivity. The chemical structure of the MOF is vital as the functionalization determines not only the strength of host-guest interactions but also what guests are able to bind. The dimensions of the cavities also determine the size of the molecules that are able to penetrate and thus bind and be detected. Typically, inert molecules do not induce a spin change and are thus not 'detected'. These SCO compounds and their selective ability demonstrate encouraging potential for the application of SCO materials as chemical sensors.

2. Experimental Techniques

The SCO phenomenon and the electronical and vibrational changes associated with it cause structural, magnetic, and optical modifications to the compound. In order to gain a better understanding of SCO and how it can be controlled, it is important to be able to probe these consequences. The following sections discuss techniques used to characterize and analyze the effects of SCO.

2.1. Magnetic Measurements

As the transition from LS → HS in Fe^{2+} SCO compounds result in a dramatic change in magnetic response (diamagnetic → paramagnetic), the magnetic susceptibility can be measured to detect and quantify an SCO transition. The magnetic response can be detected by a magnetometer, such as a superconducting quantum device (SQUID). The SQUID utilizes the Josephson effect whereby an insulator sits between a ring of two superconductors and flux quantization within this ring results in a highly sensitive and accurate device that can be used to measure the long magnetic moment.[55] This is arguably the most common and most accurate method of detecting thermal SCO.[4] The magnetic susceptibility can be calculated from the long magnetic moment and can be plot as a function of temperature to generate a spin crossover transition curve, from which $T_{1/2}$ can be deduced. The 'smoothness' of a transition can also be determined, which is defined as the difference in the temperatures where 20% and 80% of the complex is in the HS state.[22] The SCO curves are highly informative and can provide insight into the SCO character of a compound. As mentioned in **Section 1**, the SCO transition curves convey how abrupt or gradual a transition is or whether it exhibits hysteresis, thus offering an understanding on the degree of cooperativity within the compound.

In order to obtain these SCO transition curves, the magnetic susceptibility (or more accurately the long magnetic moment) is measured during heating and cooling cycles over a specific temperature range (of which the transition temperature resides). The first heating cycle is likely to display different magnetic susceptibility measurements to subsequent cycles as residual solvent molecules can cause irreversible changes to the complex and thus alter the magnetic

response. This is also known as the 'running in' effect and thus samples are typically heated first to evaporate any residual solvent that could affect the magnetic measurements. As reproducibility is an important feature of SCO compounds, the first heating and cooling cycles are generally disregarded.[6]

2.2. Vibrational Measurements

The population of the antibonding orbital upon transition into the HS state results in a weaker, longer metal-ligand bond and distorted octahedra. This results in different vibrational bond frequencies within the compound between the LS and HS states. These subtle changes are thus a good indication of SCO and the spin transitions are commonly detected by Raman spectroscopy. Raman is an analytical technique that can directly investigate the vibrational or rotational state of a molecule by the inelastic scattering of light, or Raman scattering.[56] To obtain a Raman spectrum, a sample of an SCO compound was positioned on a temperature-controlled stage that was set in relation to the compound and the electronic state being analyzed. The Raman spectra of a complex can act as a 'fingerprint' for both electronic states due to discrepancies in bond intensities and a shift in frequencies for LS and HS states that are characteristic to each complex. For smaller, simpler molecules it is possible to assign specific peaks to specific bonds, similar to Infra-red Spectroscopy. However, for the nature of this work it is deemed trivial to determine such information, and as such Raman spectra will be considered as the chemical 'fingerprint' of a compound. A 'fingerprint' of a complex in the LS and HS states is very useful when investigating three different synthetic techniques as this allows for direct comparison to determine congruency between techniques.

2.3. Powder X-Ray Diffraction

Powder x-ray diffraction (PXRD) is a technique used to determine the structural characterization of microcrystalline powders through the interpretation of diffraction peaks, intensities, positions and shapes.[57] A monochromatic X-ray beam hits the sample of powder containing small, randomly ordered crystallites. Diffraction occurs when these X-rays constructively interfere after being scattered from the atoms present in the crystallites.[57,58] This constructive interference corresponds to peaks on PXRD spectra, and their shape and intensity can provide insight into the structure and crystallinity of a material. This technique is similar to the Raman, in the respect that it acts as a 'fingerprint' for each complex and in-depth analysis of peaks is unimportant for this work. Raman and PXRD data will be used in parallel to ascertain structural similarities and differences between spin states and compounds.

2.4. Optical Measurements

The thermochromism that accompanies the switching in triazole SCO complexes is particularly prominent. The ability to quantify and thus characterize color change for SCO materials provides insight and allows for direct comparisons between samples. This can be achieved by measuring the reflected light, or reflectivity, of a sample over a range of temperatures. A schematic diagram shown in Figure *11* shows the apparatus used to measure the reflectivity. The equipment is encased in a black box to prevent the penetration of light as this would have drastic effects on the results. To further ensure the omittance of light, a blackout sheet was fit across the black box. When $T_{1/2}$ was above room temperature, the variable temperature stage was preset to heat to a temperature higher than the $T_{1/2}$ of the SCO material being analyzed and then cool back to room temperature. When $T_{1/2}$ is below room temperature, the stage was preset so that it cooled to a temperature lower than the $T_{1/2}$ value and warmed back to the initial temperature. When measuring below room temperature, liquid nitrogen is used to purge the chamber to prevent condensation. To start collecting data, the variable temperature and the camera were initiated simultaneously, and the box was sealed with the black sheet fit on top as quickly as possible. The camera recorded an image of the sample every 20 seconds over the heating and cooling cycles.

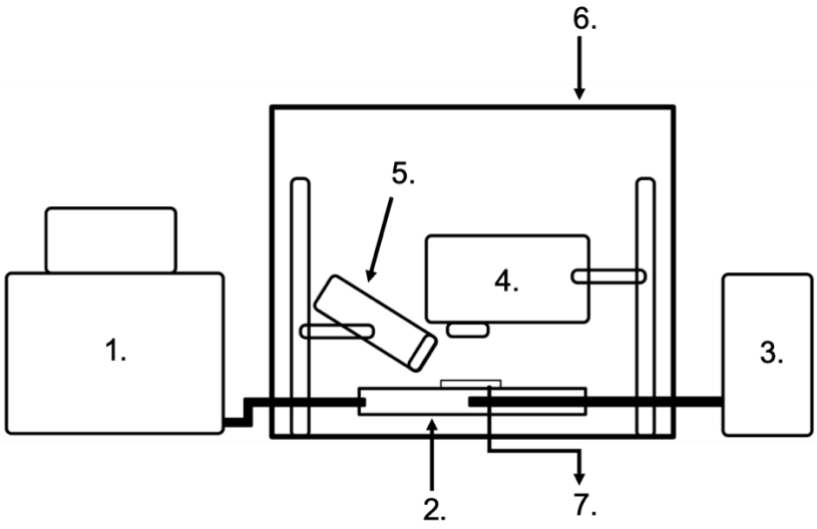

Figure 11: Schematic of apparatus used to measure reflectivity. 1) Computer; 2) Variable temperature stage; 3) Nitrogen dewar; 4) Camera; 5) Light; 6) Black box; 7) Sample holder. The black box is then covered with a blackout sheet.

To obtain the reflectivity measurements of the sample, the images were collated into a video using ImageJ software. The maximum sample area was selected, minimizing the background as much as possible, and each pixel was converted to greyscale. The mean grey value, thus the reflectivity, was calculated for each frame. The mean grey value is the sum of the grey values of the pixels within the area selected divided by the number of pixels present. These values were then plot against the temperature of the stage at the time that the image was taken. Upon color transition, the camera automatically adjusted the white balance causing discrepancies in the

results. To correct for this, the same analysis was performed on multiple regions that were not expected to change color. These values were then averaged and subtracted from the sample at each point to remove the effects of the adjustment. The resultant graph depicts the SCO profile of that material from which $T_{1/2}$ can be calculated. This can then be compared to other samples and analytical techniques such as SQUID and variable temperature Raman.

3. Aims

The core objective of this thesis is to develop a new synthetic technique for the production of large-scale thin films of spin crossover materials. The predominant feature of large-scale SCO thin films applications such as large area sensors, is color change. Therefore, part of this thesis focuses on the development of reflectivity; a method that allows the quantification of color change visually. From previous work conducted within the mechano-synthetic research of the group, it was determined that the two starting materials reacted when they came into direct contact with each other in ambient conditions. This thesis offers a preliminary investigation of the formation of SCO compounds synthesized via contact reaction of metal salts and triazole in the solid state. Three complexes synthesized via three different synthetic methods— *solution-state* (**sol**), *direct-contact* (**direct**) and *thin-film* (**thin**)— are discussed with one main study and two supplementary studies. The first and main complex investigated was $[Fe(atrz)_3]SO_4$ (complex **1**). Smaller studies on $[Fe(Htrz)_3](BF_4)_2$ (complex **2**), and $[Fe(atrz)_3]BF_4$ (complex **3**) were conducted to demonstrate potential for other SCO compounds.

4. Experimental

4.1. General Synthetic Procedures

Three separate synthetic procedures, *solution-state*, *direct-contact*, and *thin film* have been carried out to synthesize three different SCO complexes. All reagents were purchased directly from either FisherScientific or Sigma Aldrich and were used without any further purification.

4.2. Solution-state Synthesis

A concentrated aqueous solution of the appropriate iron salt was added dropwise to a concentrated aqueous solution of the ligand in a 1:3 molar ratio. The precipitate was filtered off and washed with deionized water and left in air. For complexes with $T_{1/2}$ above room temperature this resulted in a fine pink powder, typical of iron triazole complexes of this type in the LS state. Complexes with a $T_{1/2}$ below room temperature resulted in a white powder indicative of a HS product.

4.3. Direct-contact Synthesis

Crystals of iron salt were added to crystals of triazole in a 1:3 ratio and mixed in a SpeedMixer Dual Asymmetric Centrifuge 150.1 FVZ-K with an RPM of 3500 and a mix time of 10 s. For studies on the SCO properties, the reaction vessel was left to react for one hour and then analyzed. For formation studies, the sample was immediately placed into the LinkAm THMS 600 for prompt analysis.

4.3.1. Single Crystal Synthesis

A single crystal of an iron salt hydrate was forced into contact with a single crystal of triazole and left to react for 55 minutes. This was monitored using an optical microscope.

4.4. Thin-film Synthesis

The thin films were synthesized using a single action PME Airbrush and Compressor with an air output of 10 LPM and a max pressure of 25 PSI. The airbrush had a nozzle with a diameter of 0.3 mm. The iron salt hydrate was dissolved in a minimum amount of water. Triazole was dissolved in water with a concentration three times that of the iron salt solution. As the triazoles used are more soluble, the iron salt dictates the amount of solvent. Six drops of the iron salt solution were added to the cup of the airbrush and sprayed onto the Whatman 1001-125 qualitative filter paper substrate from a height of approximately 7 cm. This height was determined to be as close as possible with minimal disruption from the continuous airflow from the airbrush. The cup was then thoroughly cleaned with excess solvent and six drops of the triazole solution was sprayed onto the substrate. This constitutes as one layer. This was repeated two more times, allowing each layer to dry for an hour before the next layer was sprayed. The resultant thin film was left to air dry overnight with the SCO complex becoming visually more prominent throughout the drying process.

5. Characterization

5.1. Superconducting Quantum Interference Device (SQUID)

Magnetic susceptibility measurements were carried out using a Quantum Design MPMS SQUID (Superconducting Quantum Interference Device) magnetometer. Temperature dependent measurements were made using a 1000 Oe magnetic field in sweeping mode across the stated temperature ranges at a rate of 2 K min^{-1}. The magnetic data presented throughout are $\chi_M T$ vs T plots where χ_M represents the magnetic molar susceptibility and T represents temperature. The precision of the instrument coupled with the reproducibility of magnetic susceptibility for a complex allows for direct comparison between the three synthetic techniques.

5.2. Raman Spectroscopy

The bond stretching frequencies were measured using Raman spectroscopy at variable temperatures over a range of 200-2200 cm^{-1}. Spectra were recorded using a Horiba LabRam spectrometer equipped with a 600 grating, x 50 LWD NIR objective, and a 632.81 nm laser. The temperature stage used was a Linkam THMS 600 with a heating/cooling rate of 10 K min^{-1}.

5.3. Powder X-ray Diffraction

The data was collected at room temperature on powder samples using a Rigaku MiniFlex 600 desktop X-ray Diffractometer using Cu K_α radiation, λ = 1.54051 Å.

5.4. Reflectivity

The setup comprises of a Linkam THMS 600 with a variable temperature stage, a Brinno TLC 200 PRO camera, a light, and a portable liquid nitrogen dewar enclosed in a black box with a black sheet on top. The variable temperature heated and cooled at 2 K min^{-1} (same rate as SQUID). An image was acquired every 20 s. All reflectivity measurements were obtained by ImageJ software.

6. $[Fe(atrz)_3]SO_4$

$[Fe(atrz)_3](SO_4)$ is a member of the triazole family of compounds that has previously been reported in 2003 by L.G Lavrenova *et al.*[59] synthesized via solution based methods using $FeSO_4.7H_2O$ and 4-amino-4H-1,2,4-triazole (atrz). The effects of mechanosynthesis on the SCO properties of this complex has also been investigated by J. Askew *et al.*[22] This study revealed that the complex can be synthesized via mechanosynthetic methods with little change to the SCO properties and also provided further insight into the properties of this complex. $[Fe(atrz)_3](SO_4)$ displays the distinct color change associated with the triazole family going from pink when LS at ambient temperatures to white when HS above 350 K, seen in *Figure 12*.

Figure 12: [Fe(atrz)3](SO4) in the pink LS state and the white HS state.

$[Fe(atrz)_3](SO_4)$ forms 1-dimensional chains with each Fe atom connecting to six atrz ligands with the chains connecting via hydrogen bonds of the atrz, *Figure 13*. As these complexes

form so quickly upon reaction with very small coherent domains, it is very difficult to acquire single crystals and thus little structural information has been reported. This complex exhibits abrupt transitions with $T_{1/2}\uparrow$ = 350 K and $T_{1/2}\downarrow$ = 327 K and a hysteresis width of 14 K.[22]

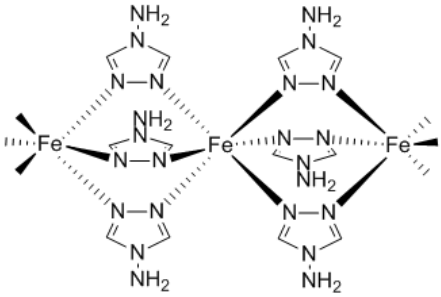

Figure 13: Structural diagram of $[Fe(atrz)3]SO_4$ depicting 1D chain propagation.

Previous studies used $FeSO_4.7H_2O$ for solution-state synthesis, however for this investigation $(NH_4)_2Fe(SO_4).6H_2O$, or Mohr's salt, has been used. $FeSO_4.7H_2O$ oxidizes rapidly which can provide difficulties in analysis. Mohr's salt was used as the presence of the acidic ammonium ions delays the oxidation process. However, this leads to an increase in by-products as $(NH_4)_2SO_4$ is readily formed. The following sections investigate and compare the properties of $[Fe(atrz)_3](SO_4)$ synthesized via *solution-state*, *direct-contact*, and *thin-film* methods.

6.1. Solution-state synthesis

6.1.1. Experimental

$(NH_4)_2Fe(SO_4)_2.6H_2O$ (1.276 mmol, 0.5 g) was dissolved in 2 ml of water and added dropwise to a solution of 4-aminotriazole (3.865 mmol, 0.325 g) dissolved in 2 ml of water. After 5 minutes of mixing, a purple precipitate formed which was collected via filtration and washed with water. This was left to airdry overnight yielding a fine pink powder of $[Fe(atrz)_3]SO_4$ (0.31 g, 62%) (**1-sol**).

6.1.2. Results and Discussion

The solution-state synthetic method is imperative to understanding the effects of the other synthetic methods explored. Thus, it is critical to determine the characteristics and properties of the solution-state powders in depth to allow for comparison. All results from other methods will be compared directly to results acquired from the solution-state protocol.

The Raman spectra of the LS and HS states, taken at 298 K and 373 K respectively, were acquired and can be seen in *Figure 14*. The spectra exhibit distinct vibrational changes between the LS and the HS state, most notably an increase in peak intensity when switching to the HS state. Peaks at 702 cm^{-1} and 972 cm^{-1} show a considerable increase in intensity after switching from LS → HS, whilst the peak at 246 cm^{-1} disappears, potentially shifting outside of the range analyzed. Peaks at 1374 cm^{-1}, 1479 cm^{-1} and 1151 cm^{-1} show a substantial decrease of intensity.

The peak at 437 cm^{-1} in the LS state has evolved into a double peak in the HS state. Significant differences are observed below 500 cm^{-1} where the Fe-N stretching is expected to be observed, which is anticipated to change drastically upon switching.

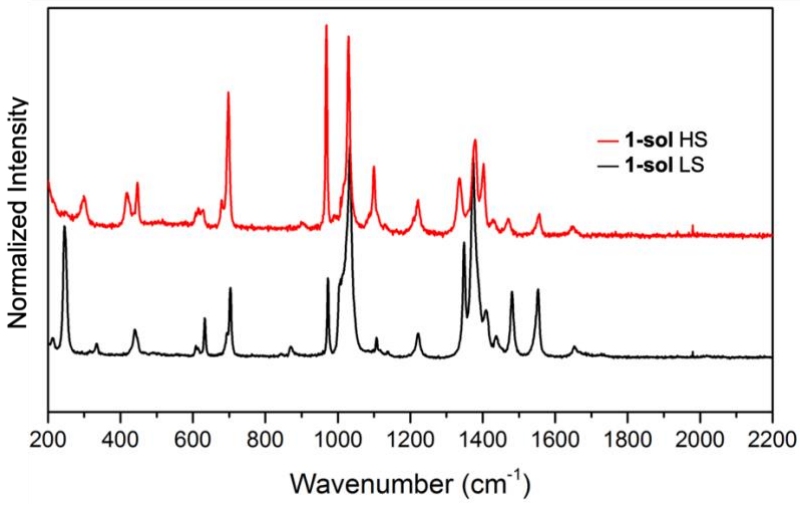

Figure 14: Normalized Raman spectroscopy plot of — LS (298 K) and — HS (373 K) electronic states of **1-sol**.

In addition to acquiring spectra at two distinct temperature values, variable temperature (VT) spectra were acquired, shown in *Figure 15*. A spectrum was acquired every 5 K over a temperature range of 298-363 K until the transition temperature range, 348-353 K, where it was taken every 1 K. The peaks at 966 cm^{-1} and 1026 cm^{-1} are demonstrably sensitive to spin state and show adequate intensity at all temperatures and thus were used to follow the SCO process. Recording spectra over small increments in temperature allows for the transition to be followed in more detail.

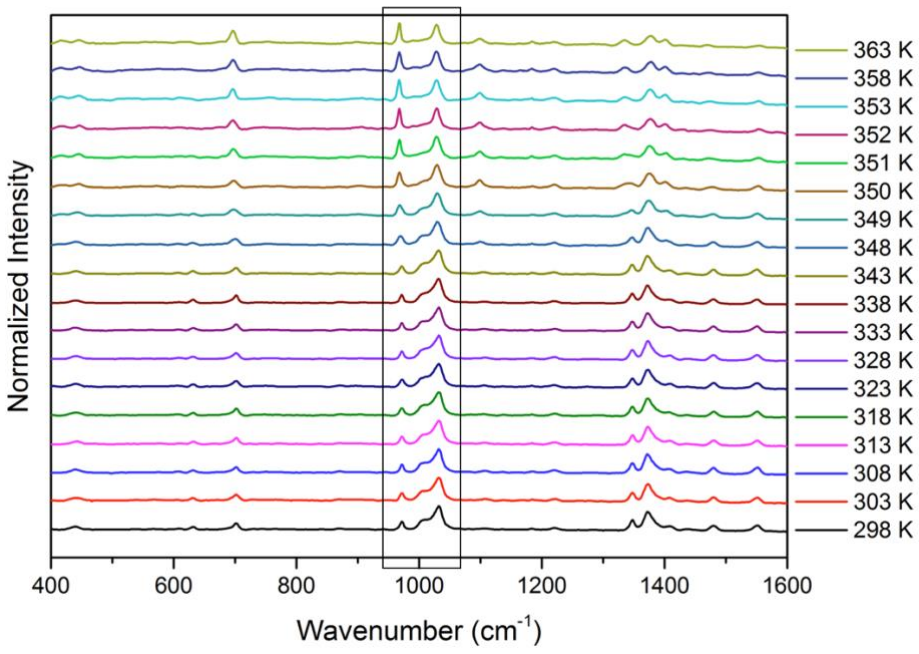

Figure 15: Normalized variable temperature Raman spectra of **1**-sol taken every 5 K over a range of 298-363 K. From 348-353 K, spectra were acquired every 1 K.

As a way of investigating and quantifying this peak transformation further, peaks at 966 cm^{-1} and 1026 cm^{-1} were integrated and a ratio of the two at each temperature calculated. This integral peak ratio was then plot as a function of temperature, revealing the spin-crossover curve for this complex, shown in *Figure 16*. From this, an approximate $T_{1/2}$ and the 'smoothness' of the curve can be calculated and compared with other values obtained from other techniques. There is a lack of accuracy in the $T_{1/2}$ and smoothness values calculated from VT Raman. As the sample is heated from the bottom and analysis conducted from the top, there may be a temperature gradient across the sample causing discrepancies between the temperature of the sample and the temperature reading thus resulting in a shift of $T_{1/2}$ values. The $T_{1/2}$ of the heating cycle ($T_{1/2}\uparrow$) was calculated as 349 K with a smoothness of 4 K which is 11 K higher than the $T_{1/2}\uparrow$ of literature values.[22] Considering the likely temperature lag, it is to be expected that the transition temperature would be higher than that of more accurate measurements, such as magnetic.

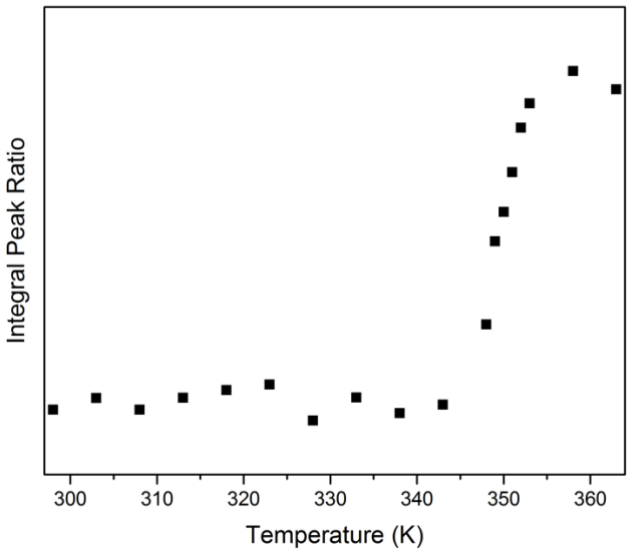

Figure 16: Integral peak ratio from variable Raman spectra of **1-sol** as a plot as a function of temperature. From this it is possible to determine $T_{1/2}$.

Magnetic measurements of the solution-state compound are shown in *Figure 17*. This shows the second and third heating and cooling cycle and reveals a high degree of reproducibility. The solution-state complex has a reasonably abrupt transition with $T_{1/2}\uparrow$ = 341 K and $T_{1/2}\downarrow$ = 332 K giving a ΔT, or hysteresis, value of 9 K. The smoothness of the transition on heating and cooling differ with values of 10 K and 8 K, respectively. The previously reported literature values of this compound for the solution state are $T_{1/2}\uparrow$ = 338 K and $T_{1/2}\downarrow$ = 325 K with a smoothness of 12 K.[22] The ideal $\chi_M T$ values for triazole complexes is between 0 for LS and 3.5 $cm^3 mol^{-1} K$ for HS. The observed values of both $\chi_M T$ and $T_{1/2}$ are very close to those stated in literature and thus can be used as a basis to compare values for the other two synthetic and analytical methods.

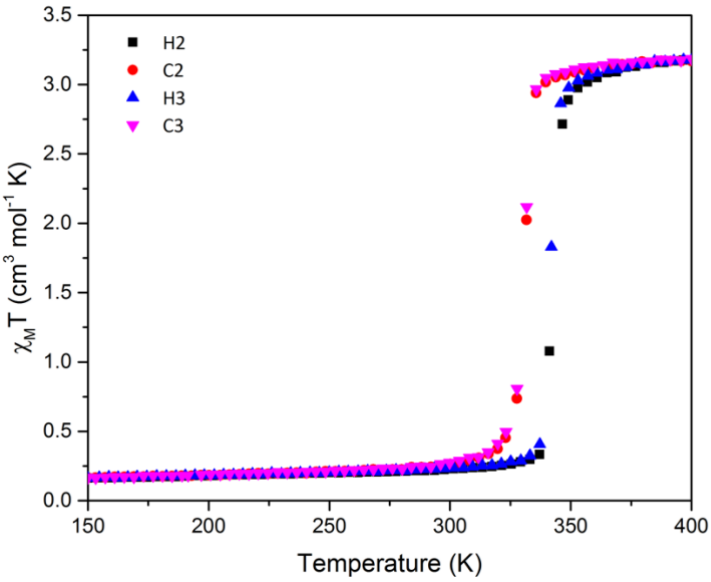

Figure 17: Plot of $\chi_M T$ vs. temperature showing the second and third heating and cooling cycles for **1-sol**.

A less conventional analytical method and one that had to be optimized and refined is reflectivity. The normalized mean grey scale can be plot as a function of temperature and thus $T_{1/2}$ values and smoothness can be calculated and compared to those acquired from the magnetic and vibrational measurements. **1-sol** was heated from 298 K to 403 K and cooled back down at 2 K min^{-1} with images captured every 20 s.

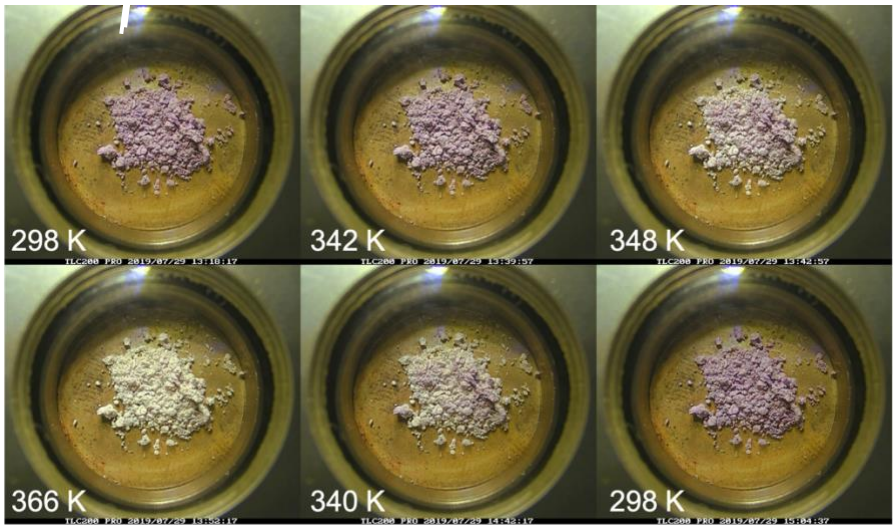

Figure 18: Visual SCO transition of **1-sol** from LS (298 K) to HS (403 K) during reflectivity analysis.

The montage in *Figure 18* shows images taken over the course of reflectivity analysis and show the visual transition from LS → HS. The images taken over the analysis period were used to generate the graph in *Figure 19*, which shows the normalized corrected reflectivity values plot as a function of temperature. This resulted in calculated values of $T_{1/2}\uparrow$ = 345 K and $T_{1/2}\downarrow$ = 338 K with a ΔT of 7 K and a smoothness of 5 K.

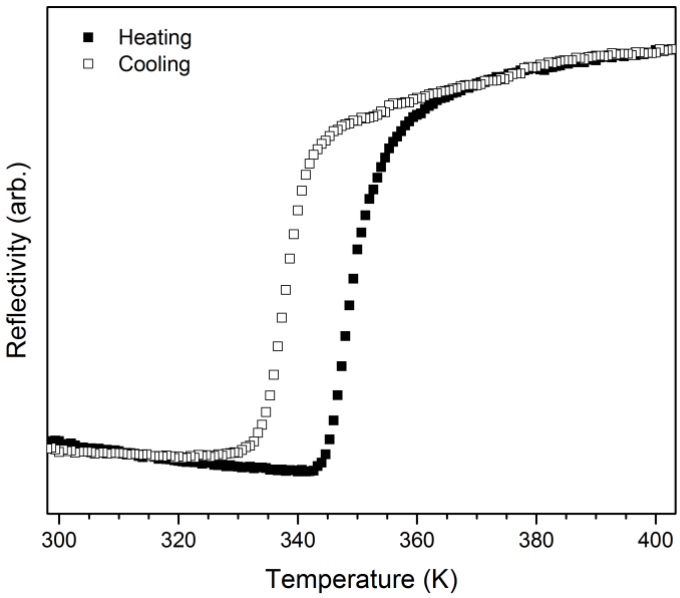

Figure 19: Corrected reflectivity values as a function of temperature for the ■ heating and □ cooling cycle of **1-sol**.

The SCO curve of the reflectivity data is slightly shifted to the right of the data acquired from the magnetic measurements, shown in *Figure 20*. Compared to the magnetic measurements, $T_{1/2}\uparrow$ was 7 K higher and $T_{1/2}\downarrow$ 6 K higher with ΔT being 2 K narrower. The increase in both $T_{1/2}$ measurements of reflectivity is most likely due to the temperature gradient across the sample. This occurs as the sample is heated from the bottom and the sample is analyzed from the top, causing a slight lag in temperature, thus shifting the results. Visually this can be confirmed, as the final area of the sample to transition is furthest from the heating element which can be seen in *Figure 18*.

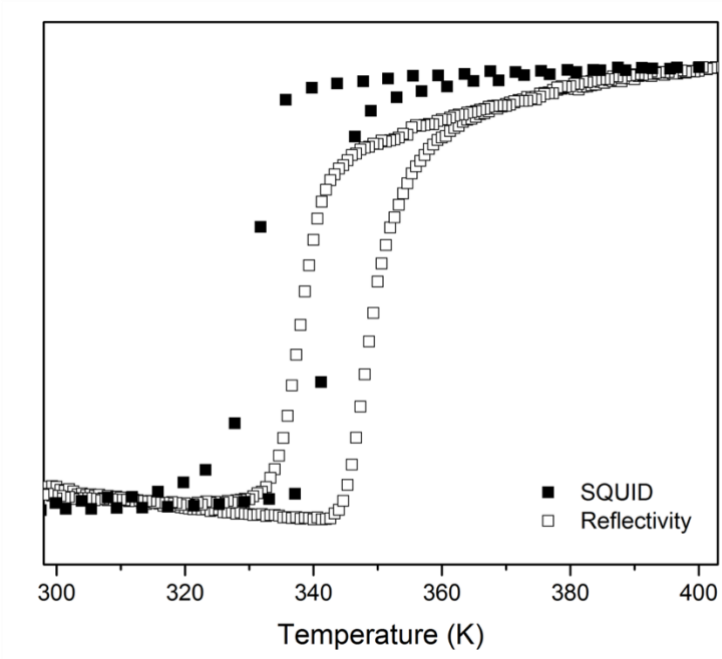

Figure 20: □ Optical reflectivity and ■ SQUID magnetic measurement comparison of **1-sol**.

6.1.3. Conclusion

The solution-state compound synthesized demonstrates similar structural and magnetic properties revealed by Raman and SQUID analysis to the compound reported in literature.[22] Therefore this compound is deemed sufficient to use as a basis of comparison for the direct-contact and thin-film synthetic results.

6.2. Direct-contact synthesis

6.2.1. Experimental

6.2.1.1. Direct-contact crystals

A single crystal of both $(NH_4)_2Fe(SO_4)_2.6H_2O$ and 4-aminotriazole were forced into contact under a microscope and left to react for 50 minutes. It was not possible to determine precise stochiometric ratios for the reaction due to the use of single crystals. A purple solid was formed.

6.2.1.2. Direct-contact synthesis

$(NH_4)_2Fe(SO_4)_2.6H_2O$ (3.825 mmol, 1.5 g) was added to 4-aminotriazole (11.475 mmol, 0.9649 g) and quickly placed in the SpeedMixer for 10 s. A very light pink complex, $[Fe(atrz)_3](SO_4)$ (**1-direct**), had formed progressing to a darker purple over the course of one hour with residual reagent still remaining.

6.2.2. Results and Discussion

From previous work conducted within the mechano-synthetic research of the group, it was determined that these two starting materials reacted when they came into direct contact with each other in ambient conditions. This was investigated further by pushing a single crystal of each reagent together and recording the reaction under a microscope. The montage shown in *Figure 21a* displays images captured throughout that exhibit the formation of $[Fe(atrz)_3]SO_4$.

(a) (b)

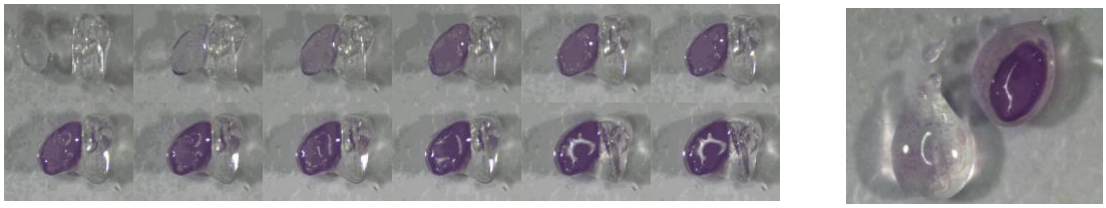

Figure 21: (a) Images showing the reaction of single crystals of $(NH_4)_2Fe(SO_4)_2.6H_2O$ (left crystal) and 4-aminotriazole (right crystal), yielding the purple SCO complex $[Fe(atrz)_3]SO_4$ over a 45 minute period with an image taken every 3-4 minutes. (b) The solid removed from the point of reaction with residual sample left behind, still enclosed in a bubble of liquid.

From this it appears as though the atrz is dissolving, either from the hydrate of the iron salt or potential humidity factors aiding dissolution – possibly a combination of both. The SCO complex is forming within the iron salt crystal suggesting that the atrz crystal is diffusing into the iron salt crystal. A large amount of liquid was formed which is most likely the atrz dissolving. A

powder of $[Fe(atrz)_3]SO_4$ was formed and was able to be removed as a solid from the liquid bubble surrounding it, as shown in *Figure 21b*.

Once it was confirmed that the crystals reacted, it was repeated on a temperature controlled Linkam stage set at 298 K and heated to 373 K to ensure the sample was SCO active. This single crystal reaction successfully yielded an active SCO complex as seen in *Figure 22*.

Figure 22: Single crystal reaction heated from 298 K to 373 K to determine crossover capability. The first image (top left) was taken at 298 K and the last image was taken at 373 K. As this was preliminary testing to see if it switched, individual temperatures were not acquired.

To investigate this on a larger scale, iron salt and atrz crystals were mixed together as described in **Section 4.3.** Immediately after mixing, a sample of the product was analyzed using reflectivity to quantify the increase in color as the complex formed over time. As previously investigated, the reaction initiates once directly in contact, with the SpeedMixer maximizing distribution of crystals thus ensuring further reaction. Between the mixing process and the time taken to set up the reflectivity equipment, the reaction had already started to progress. Therefore, the first image shows a pink color as the complex had begun to form, becoming increasingly darker as the reaction continues, as shown in *Figure 23*.

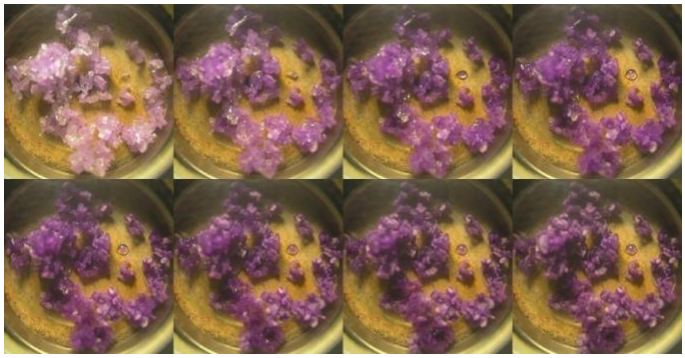

Figure 23: This reflectivity montage depicts the formation of $[Fe(atrz)_3]SO_4$ $[Fe(atrz)_3]SO_4$ over time immediately after mixing. The top left image can be assumed to be at zero seconds with the bottom right image at 3000 s.

The reaction was monitored for 55 minutes and the reflectivity was measured and plot as a function of time, shown in *Figure 24*. The graph shows a fast reaction rate until around 250 s where it begins to react at a steadier rate and plateauing around 3000 s. Visually it appears as though the direct-contact method synthesizes $[Fe(atrz)_3]SO_4$, however it is important to

determine the characteristics and properties compared to that of the traditional solution-state as synthesized in **Section 6.1.**

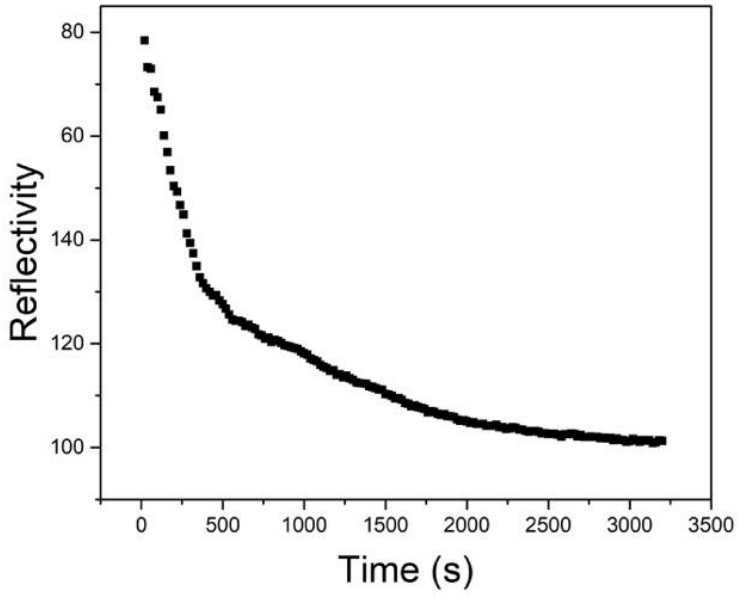

Figure 24: Reflectivity of formation of **1-direct**.

Raman data was collected of each electronic spin state to determine peak changes between the LS and HS, as seen in *Figure 25*. Each spin state was then compared with the corresponding spin state in **1-sol**, shown in *Figure 26* and *Figure 27*, to determine similarities between peak positions and their respective intensities and frequencies.

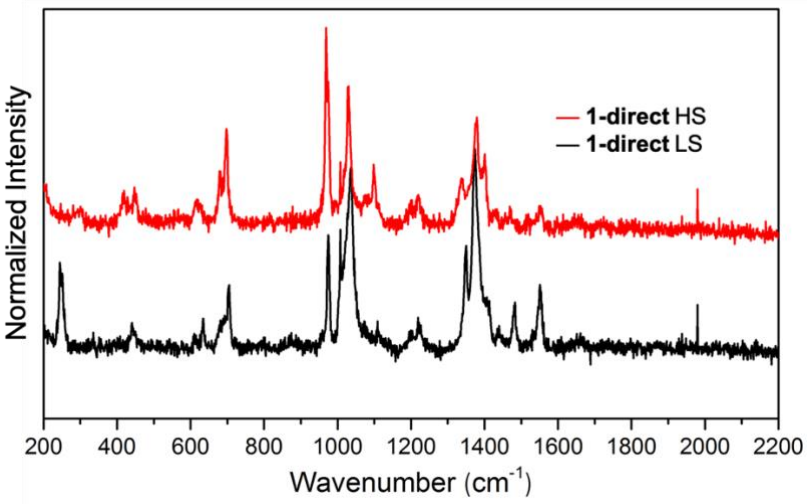

Figure 25: Raman spectra of **1-direct** — LS (298 K) and — HS (373 K) states.

Analysis of the data shows that **1-sol** and **1-direct** have similar patterns in both spin states with comparable differences upon transition. Smaller peaks are not as defined as a result of the increased signal to noise ratio of the **1-direct** compound, although are still visibly present. The HS spectrum of **1-direct** exhibits the expected changes that are characteristic to the $[Fe(atrz)_3]SO_4$ complex. Notable similarities between **1-sol** and **1-direct** include the peak at 439 cm^{-1} in the LS

state of transforming into a double peak. Increase of intensities at peaks 702 cm^{-1}, 975 cm^{-1}, and 1098 cm^{-1} and the decrease in intensities of peaks at 1372 cm^{-1}, 1482 cm^{-1} and 1550 cm^{-1}. The peak at 250 cm^{-1} also disappears or shifts beyond the range, as is the case with the **1-sol** compound. The similarity between both the LS and HS spectra of the solution-state and direct-contact synthetic methods indicates that the same complex has been synthesized.

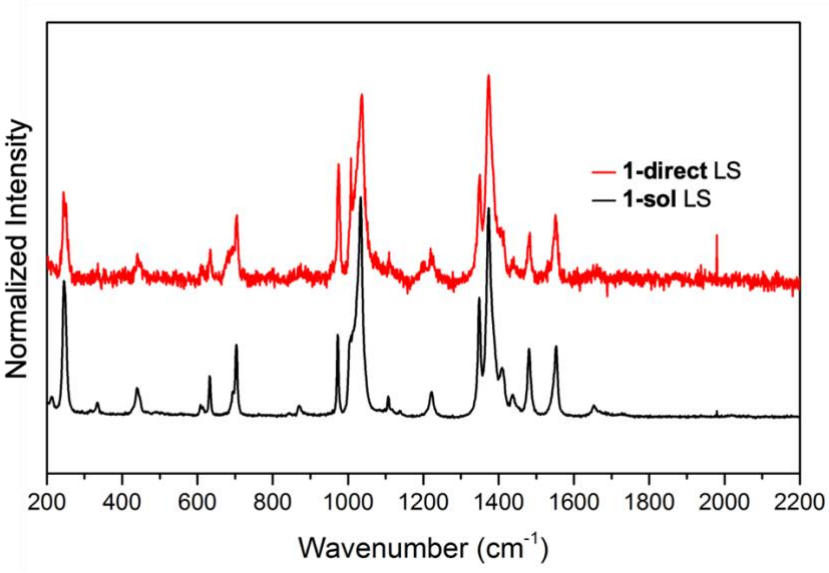

Figure 26: Raman spectra of the — LS **1-sol** and the — LS **1-direct** (298 K).

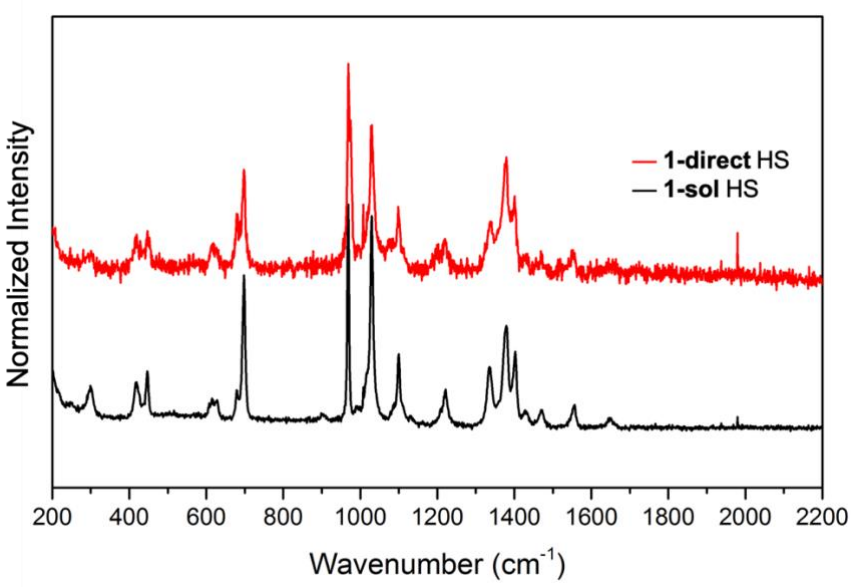

Figure 27: Raman spectra of the — HS **1-sol** and the — HS **1-direct** (373 K).

To further determine whether **1-sol** and **1-direct** structures are analogous, powder x-ray diffraction analysis was undertaken. The powder diffraction patterns of **1-direct** and **1-sol**, shown in *Figure 28*, show comparable degrees of crystallinity. Some peaks of **1-direct** are slightly wider than the peaks of **1-sol** which could be due to many factors such as decreased particle size, topology/morphology of crystallites and potential preferred orientation.[57] **1-direct** has several additional peaks present at 16.9°, an intense peak at 20.4°, 22.8°, 28.4°, 33.6° and 41.4°.

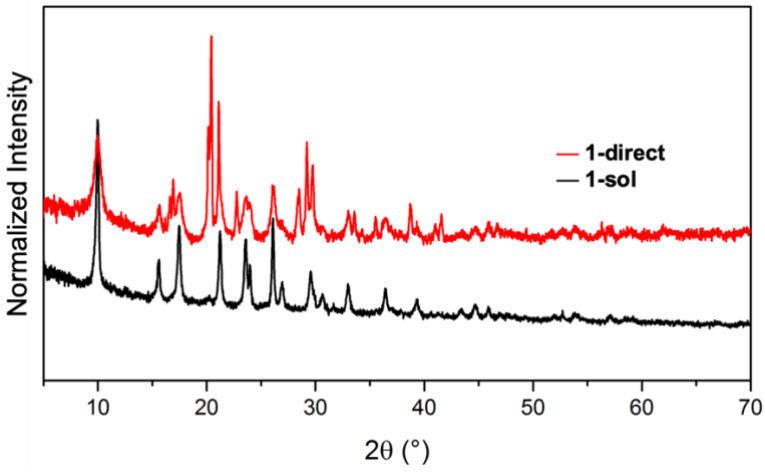

Figure 28: Powder x-ray diffraction patterns of — **1-sol** and — **1-direct**.

This data also illustrates the short-range order of these materials with peaks generally being between 10-40°. The diffraction patterns of the reagents were also obtained to determine whether these additional peaks were a consequence of residual unreacted reagents, shown in *Figure 29*. Analysis of this indicates that the additional peaks do not correspond to either of the reagents, thus can most likely be attributed to the formation of the by-product ammonium sulfate.

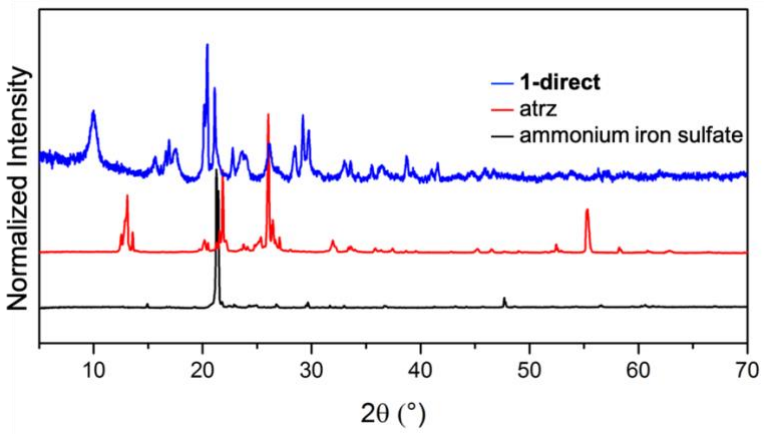

Figure 29: Powder x-ray diffraction patterns of **1-direct**, atrz and ammonium iron sulfate.

The magnetic measurements for **1-direct** exhibit a $T_{1/2}\uparrow$ = 341 K and $T_{1/2}\downarrow$ = 315 K with ΔT = 26 K, with a heating and cooling smoothness of 12 and 8 K, respectively. Magnetic measurements of **1-direct** can be compared directly to that of **1-sol**. The $T_{1/2}\uparrow$ values are identical for both methods; however, the transition range is 2.4 K wider meaning a slightly more gradual transition upon heating. The $T_{1/2}\downarrow$ value for **1-direct** is 16 K lower with an identical smoothness of 8 K. The lower $T_{1/2}\downarrow$ value and thus the increase in hysteresis indicates an increase in cooperativity within the **1-direct** compound. $\chi_M T$ values are relatively close to the ideal value between 0.6 and 2.25 $cm^3\ mol^{-1}\ K$. The HS value is slightly lower than the ideal value of 3.5 $cm^3\ mol^{-1}\ K$ and is most likely a consequence of the diamagnetic contribution of the unreacted reagents and the probable

formation of the ammonium sulfate by-product. As these compounds are typically sensitive to solvent molecules, washing was not carried out post-synthesis. Therefore, impurities are likely present that will have an affect the absolute values of $\chi_M T$.

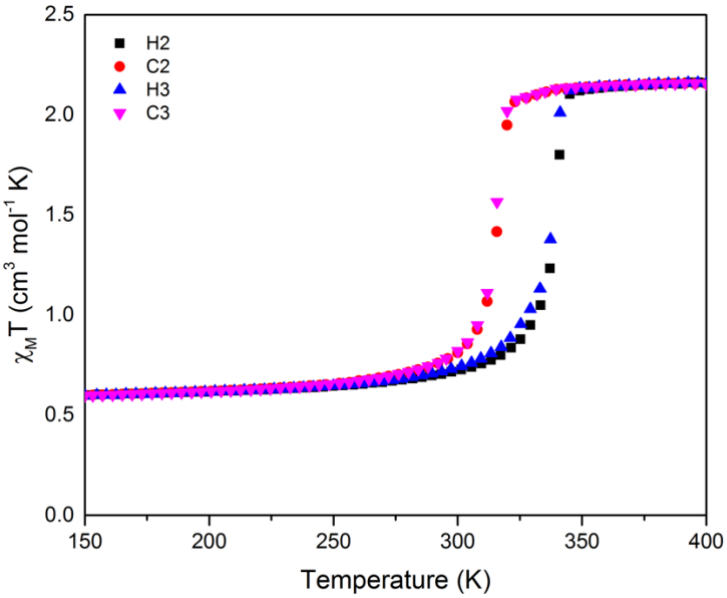

Figure 30: Magnetic measurements of the second and third heating and cooling cycles of **1-direct**.

The reflectivity data was recorded over a temperature range of 298-403 K demonstrated by the montage in *Figure 31*. Analysis of reflectivity, shown in *Figure 32*, yields values of $T_{1/2}\uparrow$ = 362 K and $T_{1/2}\downarrow$ = 316 K with a hysteresis width of 46 K and a smoothness of 8 K. Compared to the **1-direct** magnetic measurements, $T_{1/2}\uparrow$ increased by 21 K followed by an increase in $T_{1/2}\downarrow$ by 17 K. The $T_{1/2}$ values appear to have been shifted by approximately 20 K. This shift in $T_{1/2}$ values and the increase in hysteresis compared to the magnetic measurement is most likely a consequence of the potential temperature gradient across the sample. The direct comparison of optical and magnetic measurements can be seen in *Figure 33*.

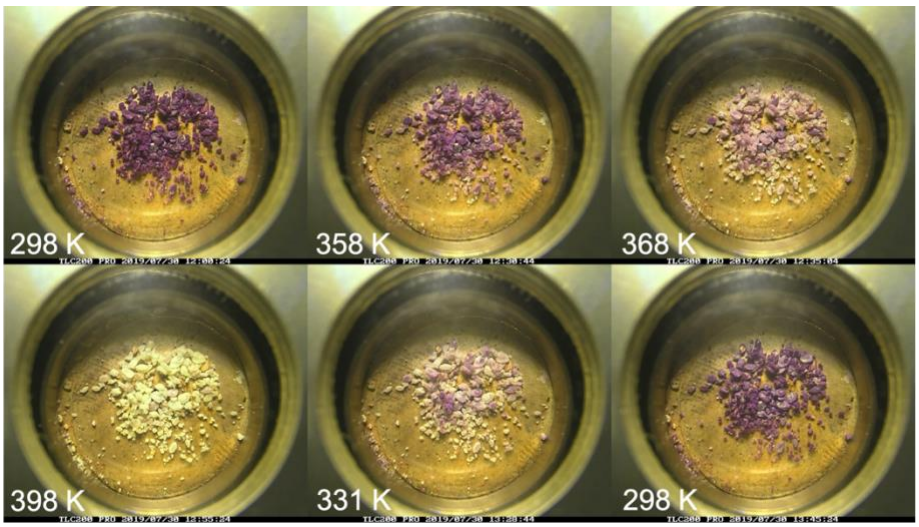

Figure 31: Transition of **1-direct** LS → HS over 298-403 K.

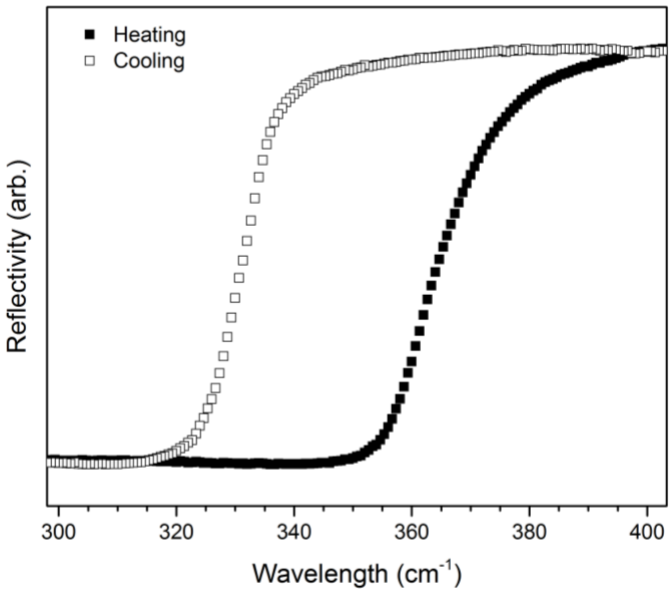

Figure 32: Reflectivity of **1-direct** for the ■ heating and □ cooling cycle.

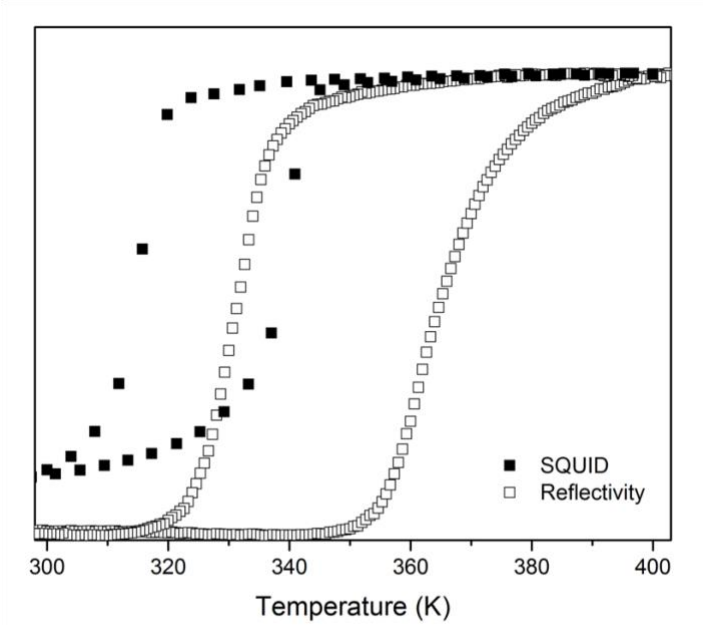

Figure 33: □ Optical reflectivity and ■ SQUID magnetic measurements comparison of **1-direct**.

The surface morphology of **1-sol** and **1-direct**, obtained via a Scanning Electron Microscope, are vastly different as seen in Figure *34*. **1-sol** displays a typical powder morphology whilst **1-direct** displays elongated rod like particles with large, embedded particles. This is likely the result of a highly concentrated reaction where the particles keep growing until growth can no longer occur, causing long tentacle-like rods. This difference in morphologies requires further investigation with a Transmission Electron Microscope (TEM) that would allow a closer look at a higher resolution. It is also likely that humidity plays a role in the formation of these rods and thus further quantification is required in future work.

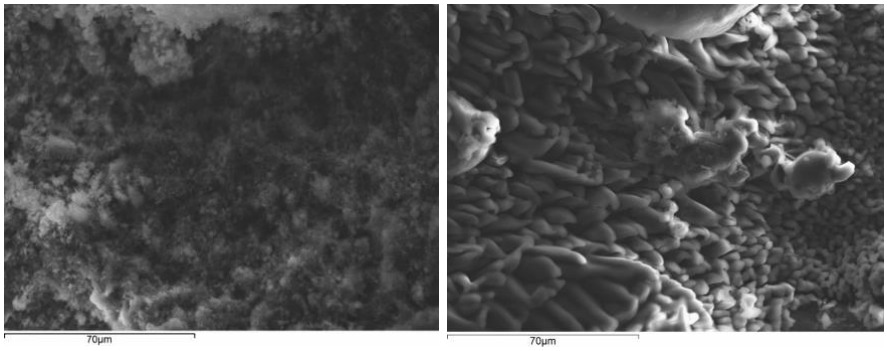

Figure 34: (Left) A Scanning Electron Microscope image of **1-sol** depicting a powder morphology. (Right) An SEM image of **1-direct** showing the formation of long tentacle-like rods most likely a cause of high concentration.

6.2.3 Conclusion

In conclusion, Raman and PXRD data confirm the same compounds with similar structures are synthesized via direct-contact and solution-state methods. SQUID data shows slight differences in magnetic properties between the two compounds. $T_{1/2}\uparrow$ values are identical with **1-direct** undergoing a slightly more gradual transition than **1-sol** and $T_{1/2}\downarrow$ is lower with an identical smoothness. Reflectivity measurements indicate an increase in cooperativity within the **1-direct** compound indicated by the increase in hysteresis. The **1-direct** compound demonstrates a 17 K and 20 K increase in $T_{1/2}$ values which is most likely inherent to the analytical technique and not intrinsic to the compound itself, as seen by the magnetic measurements. SEM analysis shows different morphologies between the two synthetic protocols with **1-direct** comprising of larger, elongated rod-like particles and **1-sol** exhibiting a more continuous powder morphology.

6.3. Thin Film Synthesis

6.3.1. Experimental

The protocol was followed as stated in **Section 4.4.** with $(NH_4)_2Fe(SO_4)_2.6H_2O$ (1.276 mmol, 0.5 g) and 4-aminotriazole (3.865 mmol, 0.325 g) dissolved separately in 1.2 ml of water – yielding a pink thin film of $[Fe(atrz)_3](SO_4)$ (**1-thin**).

6.3.2. Results and Discussion

The thin-film compound (**1-thin**) synthesized using the above procedure is analyzed and compared to the solution-state compound (**1-sol**) synthesized as stated in Section 4.1. As the compound is adhered to a filter paper substrate, a spectrum of the plain substrate was acquired to differentiate between substrate and compound. The Raman spectra in *Figure 35* shows a similar pattern for both **1-thin** and **1-sol**, indicating that $[Fe(atrz)_3]SO_4$ was synthesized. Peaks for **1-thin** are somewhat broader than that of **1-sol** and are likely due to the amorphous and inhomogeneous nature across the sample from the presence of the substrate. The broadness

present from 200-1600 cm^{-1} is a consequence of the fluorescence from the substrate and can be seen in both the substrate and **1-thin** spectra.

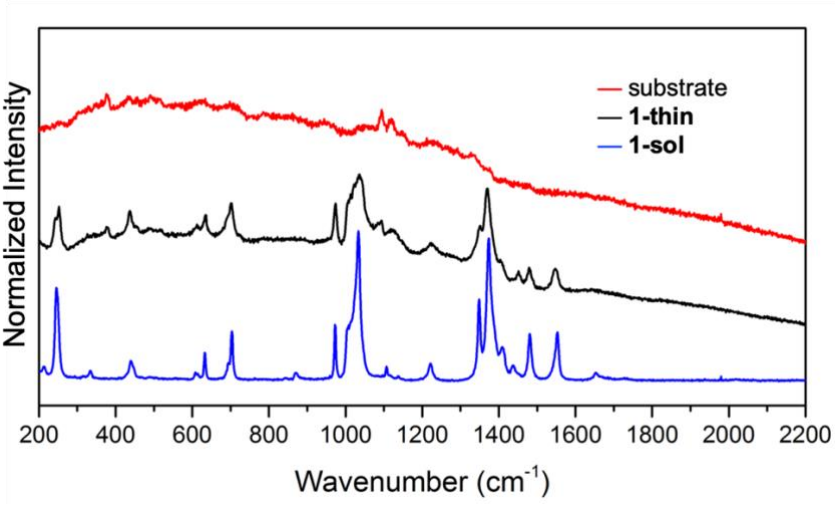

Figure 35: Normalized Raman of — **1-thin**, — substrate, and — **1-sol** (298 K).

PXRD data, in *Figure 36*, shows that **1-thin** has a similar pattern to **1-sol** with the broad peaks from 12-20˚ and 20-25˚ as a result of the substrate. The peaks of **1-thin** are less intense and slightly broader with a larger signal to noise ratio than that of **1-sol** likely due to the amorphous and inhomogeneous nature of the thin film.

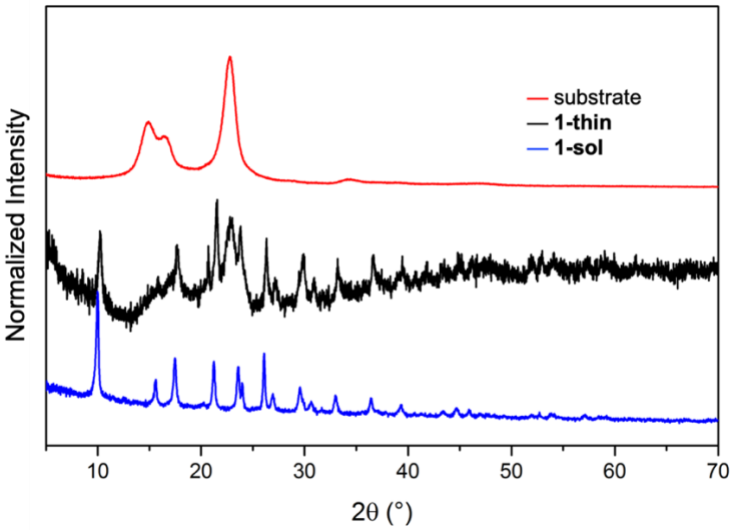

Figure 36: Normalized powder x-ray diffraction of — substrate, — **1-thin**, and — **1-sol**.

The magnetic measurements for **1-thin** reveal $T_{1/2}\uparrow$ = 333 K and $T_{1/2}\downarrow$ = 324 K with ΔT = 9 K and smoothness values of 8 K and 12 K respectively. $T_{1/2}\uparrow$ is 8 K lower than **1-sol** with a similar smoothness value with only a slight difference of 1 K. $T_{1/2}\downarrow$ is also 8 K lower with an increase in smoothness of 4 K indicative of a more gradual transition. The hysteresis values are identical potentially indicating that the substrate does not interfere with the propagation and cooperativity of the compound.

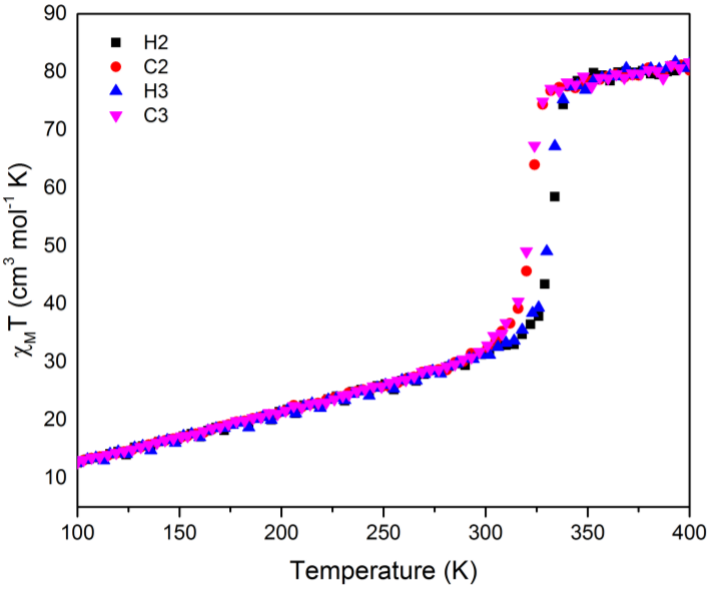

Figure 37: Magnetic measurements of 1-thin without first heating and cooling cycles.

The $\chi_M T$ values are much higher than the ideal values for triazole SCO compounds as a result of the diamagnetic contribution from the large amount of substrate present. These values are also intrinsically inaccurate as they rely on knowing the mass of sample on the substrate which is difficult to determine with any degree of accuracy. The steady increase of $\chi_M T$ from 1 to 3.5 cm^3 mol^{-1} K over a temperature range of 100-325 K is also a side effect of the diamagnetic contribution from the substrate. However, from a very small amount of compound on a very large amount of diamagnetic substrate, the magnetic measurements are still remarkably close to the values of **1-sol**.

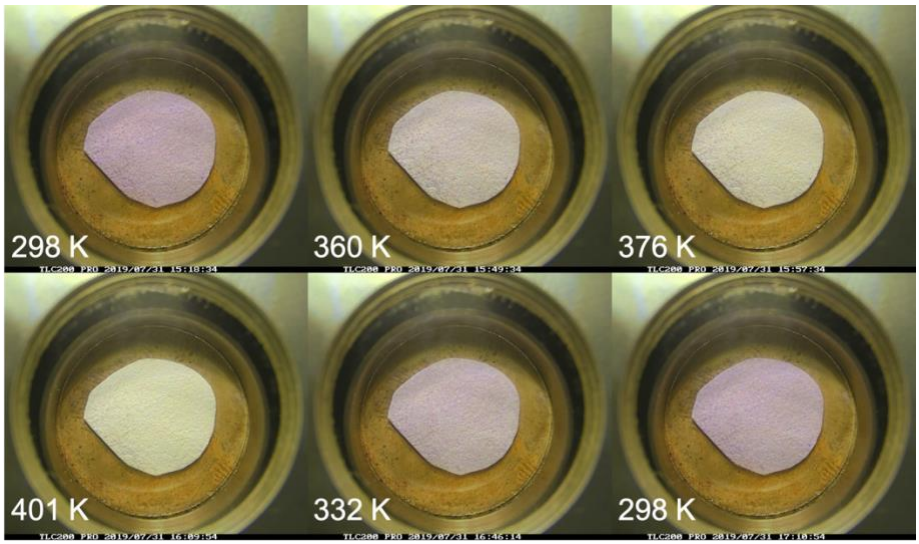

Figure 38: Reflectivity montage of **1-thin** during the heating (298 K → 403 K) and cooling (403 K → 298 K) cycles.

To obtain reflectivity measurements, **1-thin** was heated from 298 K → 403 K and then cooled back to 298 K. The reflectivity of **1-thin**, shown in Figure *39*, displays the typical shape of

curve expected for this material with $T_{1/2}\uparrow$ = 347 K and $T_{1/2}\downarrow$ = 335 K. This is a 14 K and an 11 K difference, respectively, to the magnetic measurements obtained. This larger difference of $T_{1/2}$ values are likely due to the temperature lag from the heating and cooling of the sample. The heat must also transfer from the stage through the insulating substrate to reach the sample on the surface, causing an even larger lag. ΔT of the reflectivity is 12 K which is an increase of 3 K compared to the values obtained from magnetic measurements. The heating and cooling smoothness value is 3 K, a 5 K and 7 K difference from the respective magnetic measurements. Compared to the **1-sol** magnetic measurements, the **1-thin** reflectivity $T_{1/2}\uparrow$ is 6 K higher and $T_{1/2}\downarrow$ is 3 K higher with an increase in hysteresis width of 4 K. The smoothness values of the heating and cooling cycle demonstrate a 7 K and 5 K decrease, respectively. The reflectivity and magnetic measurements comparison are shown in *Figure 40*.

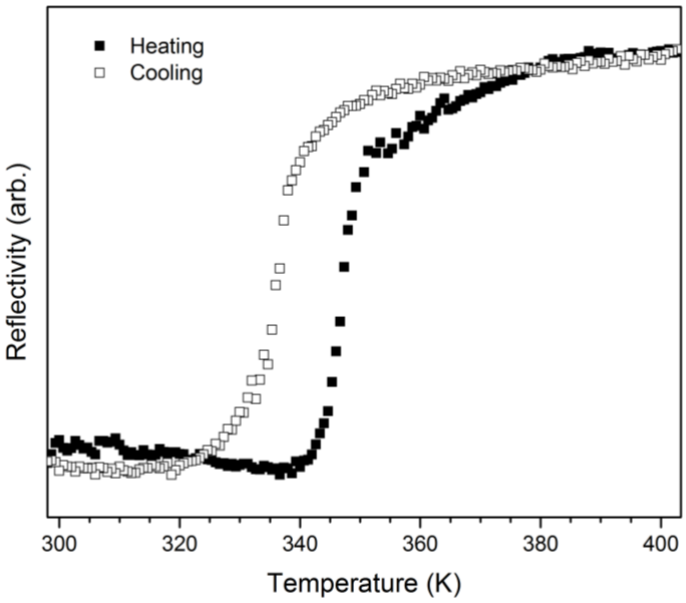

Figure 39: Plot of corrected reflectivity vs. temperature of **1-thin** during ■ heating and □ cooling.

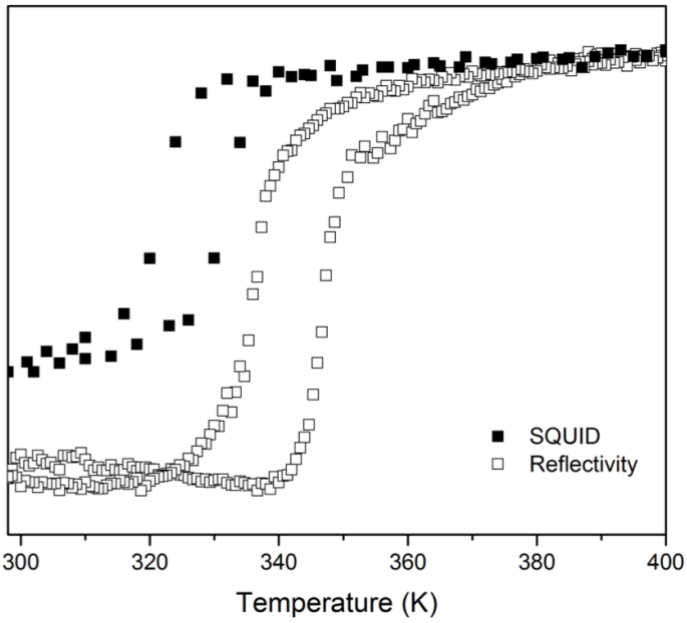

Figure 40: Comparison of □ optical and ■ magnetic measurements of **1-thin**.

The SEM image shown in *Figure 41a* illustrates the intricate, interwoven network of fibers within the paper substrate. This does not depict the characteristically desirable homogenous topology suitable for thin film applications, however this thesis is a preliminary investigation and can be thought of as a 'proof of concept.' *Figure 41b* shows the network of fibers coated in the $[Fe(atrz)_3]SO_4$ complex to form **1-thin**. The morphology of **1-thin** resembles the SEM images of **1-sol** more than **1-direct** and appears to consist of a series of particulates instead of a continuous, homogenous film.

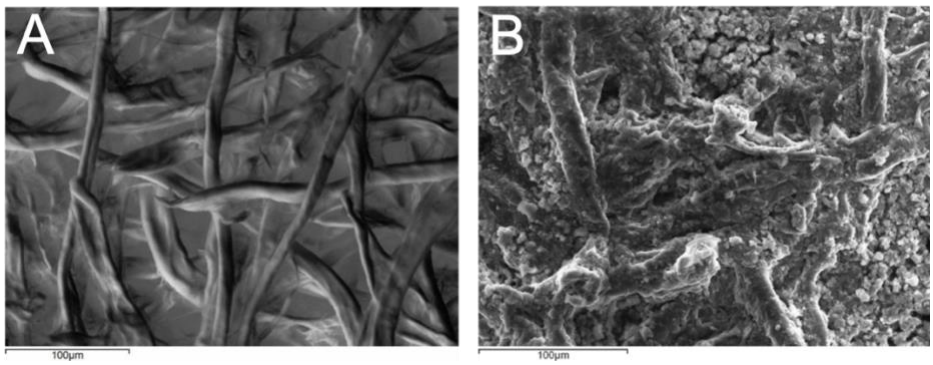

Figure 41: Scanning Electron Microscope images of a) plain substrate and b) **1-thin**.

6.3.3 Conclusion

The Raman (*Figure 42*) and PXRD (*Figure 43*) plots show the vibrational spectra and diffraction patterns of complex **1** formed via *solution-state*, *direct-contact* and *thin-film* synthesis. The Raman spectra are strikingly similar for all three methods with comparable characteristic peak changes upon transition. This, coupled with similar PXRD patterns, draws the conclusion that $[Fe(atrz)_3]SO_4$ was successfully synthesized via each method.

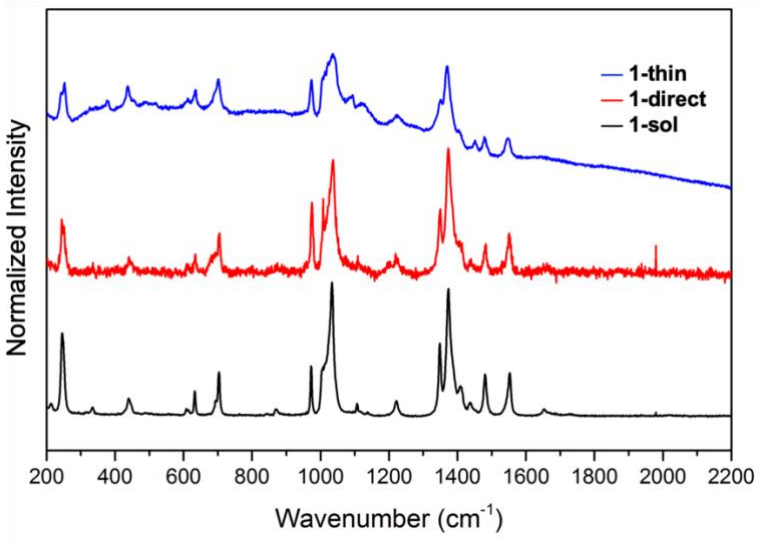

Figure 42: Raman spectra of — **1-thin**, — **1-direct**, — **1-sol** (298 K).

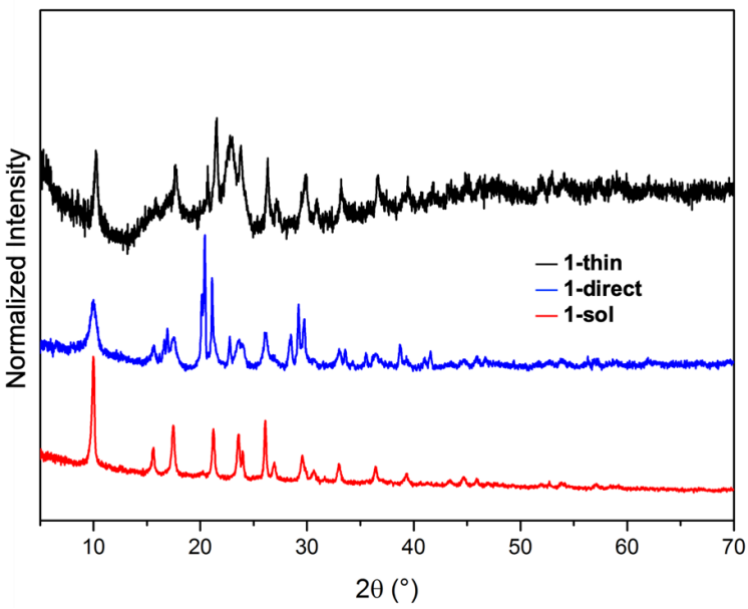

Figure 43: PXRD of — **1-thin**, — **1-direct**, and — **1-sol**.

The magnetic measurements, shown in *Figure 44*, of **1-direct** and **1-thin** differ slightly to that of **1-sol**. For **1-direct** this is most likely because of the unavoidable likely presence of impurities and the ammonium sulfate by-product. The presence of diamagnetic filter paper in the **1-thin** sample inevitably effects the magnetic susceptibility measurements. However, with these factors taken into consideration, the magnetic measurements remain considerably close.

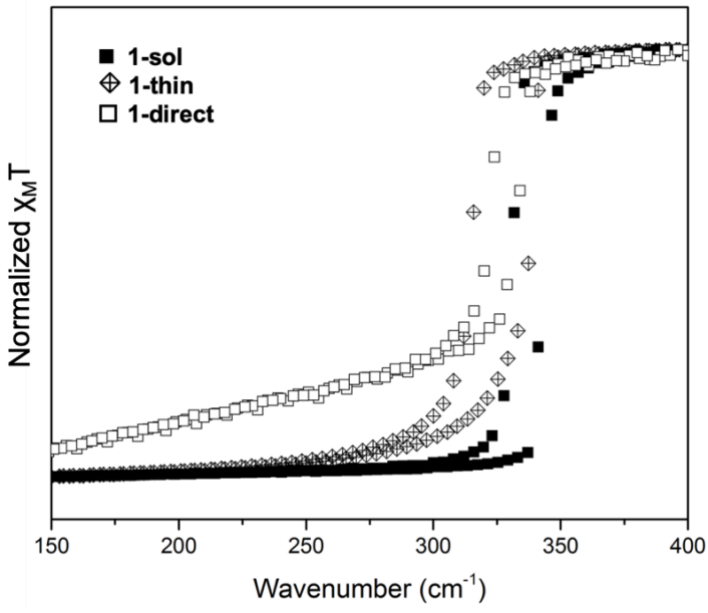

Figure 44: SQUID magnetic measurements of ■ **1-sol**, × **1-direct**, and □ **1-thin**.

Figure 44 shows the reflectivity of each synthetic method. **1-sol** and **1-thin** are similar in temperatures and hysteresis width with **1-direct** showing a much wider hysteresis and transition temperatures. This does not reflect in the magnetic measurements and is likely to be a consequence of the morphology of the complex when synthesized by direct contact. Visually, the grains appear larger and this could contribute to an even greater temperature lag due to less

effective heat transfer during reflectivity analysis. This, coupled with the presence of impurities and possible by-products, will therefore affect the overall mean grey scale and thus the width of the hysteresis.

Figure 45: Reflectivity of ■ **1-sol**, **1-direct** and □ **1-thin**.

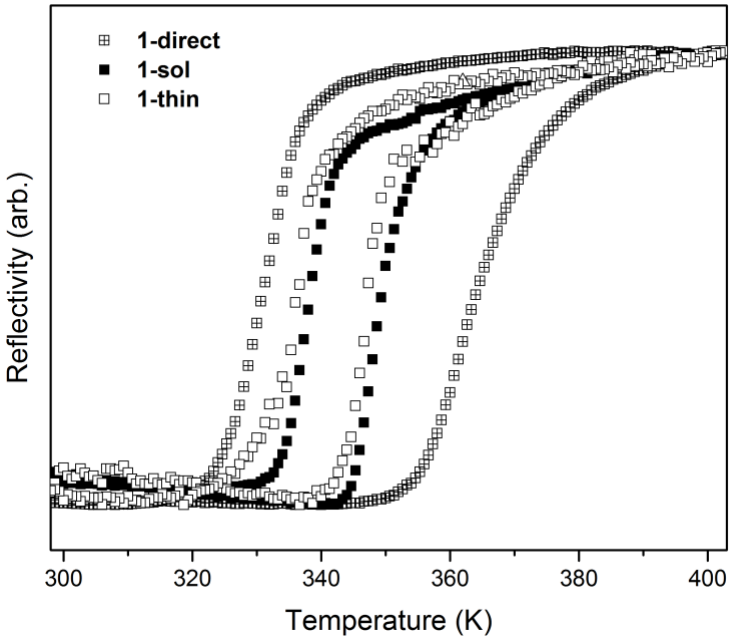

In conclusion, all three synthetic routes form $[Fe(atrz)_3]SO_4$ with comparable SCO properties.

7. $[Fe(Htrz)_2(trz)](BF_4)$

The $[Fe(Htrz)_2(trz)]BF_4$ complex is more widely studied than $[Fe(atrz)_3]SO_4$ and was first reported in 1977. Later, *Lavrenova* et al. reportedly synthesized a polymorph of this complex with the formula $[Fe(Htrz)_3](BF_4)_2$. This prompted a further study into these two complexes and their corresponding properties by *J. Kröber* et al.[60] This study found that the deprotonated $[Fe(Htrz)_2(trz)]BF_4$ yields two complexes — the hydrated α phase, $Fe(Htrz)_3](BF_4)_2.H_2O$, and the dehydrated β, $[Fe(Htrz)_2(trz)]BF_4$. These complexes exhibit different properties but similar thermochromism from pink (LS) to white (HS). The more stable α phase SCO profile reveals a very abrupt transition with $T_{1/2}\uparrow$ = 385 K and $T_{1/2}\downarrow$ = 345 K with a hysteresis width that can reach up to 50 K and smoothness of 4.2 K. The β phase has a $T_{1/2}\uparrow$ = 350 K and $T_{1/2}\downarrow$ = 325 K with a much narrower hysteresis that can be reduced up to 50% of that of the α phase. The chemical analysis of both complexes indicated that these compounds were identical and did not reveal the presence of water. The significant differences between the SCO properties, however, suggested that perhaps a very small amount of water too small for chemical analysis is likely present within the structure. This was possibly modifying the crystal structure via hydrogen bonding creating a strong cooperative network that is evident through the large hysteresis.

As mentioned previously, it is very difficult to obtain single crystals of these complexes and thus structural properties are not widely reported. The structures of the α and β phases were further studied by the same group.[10] EXAF analysis confirmed that these compounds form linear chains of octahedral Fe atoms triply bridged to the triazole ligands in the 1,2 N positions with a deprotonated triazolato group disordered across each bridging network. Later in 2013, *Grosjean* et al.[61] synthesized the complex with the largest domain size reported which provided great insight into the structural properties. The crystal structure is an asymmetrical unit with Htrz, trz^- and BF_4 lying on a mirror plane with an Fe inversion center. The triazole ligands create voids along the chain whereby BF_4 anions reside. This study revealed that there is no presence of water within the structure and that the strong cooperativity observed can be attributed to the direct interactions between Htrz and trz^- ions and the indirect chain-BF_4-chain interactions.

Two polymorphs of the protonated modification $[Fe(Htrz)_3](BF_4)_2$ were also reported — the hydrated α phase, $[Fe(Htrz)_3](BF_4)_2.H_2O$ and the dehydrated β phase, $[Fe(Htrz)_3](BF_4)_2$.[10,60] The chemical analysis of the hydrated phase of $[Fe(Htrz)_3](BF_4)_2.H_2O$ confirms the presence of water. The magnetic measurements reveal $T_{1/2}\uparrow$ = 345 K and $T_{1/2}\downarrow$ = 323 K with a smoothness of 13 K and 9 K, respectively.[60] The dehydrated β phase has a transition below room temperature $T_{1/2}\uparrow$ = 282 K and $T_{1/2}\downarrow$ = 276 K with a narrow hysteresis of 6 K. The smoothness of the heating and cooling cycles were 7 K and 4 K, respectively, indicative of a more abrupt transition. At temperatures above 440 K, the hydrated phase converts into the dehydrated phase and thus on cooling the Fe atoms remain in the HS state until $T_{1/2}\downarrow$ = 276 K. The complex returns to the hydrated phase spontaneously after the absorption of moisture from the atmosphere. EXAF analysis depicts that $[Fe(Htrz)_3](BF_4)_2$ has an identical structure to $[Fe(Htrz)_2(trz)]BF_4$ with octahedral Fe triply bridged to triazole ligands in the 1,2 N positions in a 1D chain.[10]

The following sections investigate the properties of $[Fe(Htrz)_2(trz)]BF_4$ synthesized via *solution-state, direct-contact,* and *thin-film* methods.

7.1. Solution-state Synthesis

7.1.1. Experimental

$Fe(BF_4)_2.6H_2O$ (1.481 mmol, 0.5 g) was dissolved in 3 ml of water and added to a solution of 1*H*-1,2,4-triazole (Htrz) (4.444 mmol, 0.3069 g) dissolved in 2 ml of water. A pink precipitate (**2-direct**) formed and was filtered and washed with water and left to air dry.

7.1.2. Results and Discussion

The Raman spectra of the LS and HS states of **2-sol** can be seen in *Figure 46* and were acquired at 298 K and 403 K, respectively. Various spectral differences can be seen between the two states that are indicative of structural changes and thus SCO. Peaks at 1056 cm^{-1} and 1530

cm^{-1} decreased in intensity from LS → HS. Alternatively, peaks at 767 cm^{-1}, 1163 cm^{-1} and 1428 cm^{-1} increased. Between 978 cm^{-1} and 1447 cm^{-1} the peaks shift slightly to lower wavenumbers upon HS transition with the exception of 1530 cm^{-1} which increases to 1536 cm^{-1}. The drastic changes that occur at 286 cm^{-1} and below can be attributed to the Fe-N stretching vibration, of which reduces significantly upon transition. The peaks at 1056 cm^{-1} and 1312 cm^{-1} originate from the Htrz ligand and peaks at 1088 cm^{-1} and 1282 cm^{-1} can be attributed to the triazole (trz) ligand.[62] The relative intensity of the trz peak to the Htrz peak is roughly a 1:2 ratio concurring with the 1:2 stochiometric ratio in $[Fe(Htrz_2)(trz)]BF_4$). The vibrational spectra of the LS and HS structures were compared to the Raman spectra acquired in the literature showing similar and corresponding peaks for both electronic states.[62]

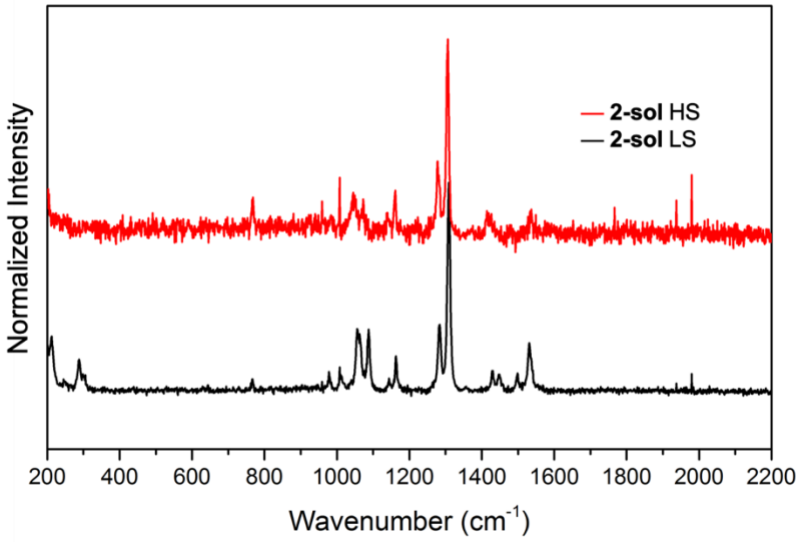

Figure 46: Plot of normalized intensity vs. wavenumber for **2-sol** in the — LS (298 K) and — HS (403 K) states.

The diffraction patterns for the LS structure of **2-sol,** shown in *Figure 47*, are very similar to the diffraction patterns in the literature and are representative of the short-range structure.[62] This, coupled with the vibrational spectra indicates that $[Fe(Htrz)_2(trz)](BF_4)$ was successfully synthesized and thus the direct-contact and thin film methods could be compared to the solution-state method.

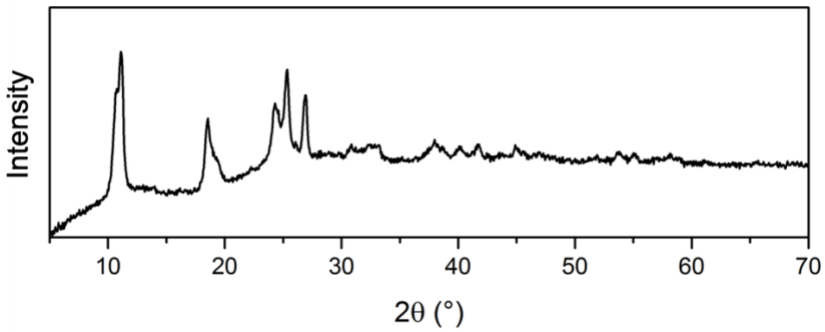

Figure 47: Powder diffraction pattern of **2-sol** in the LS state.

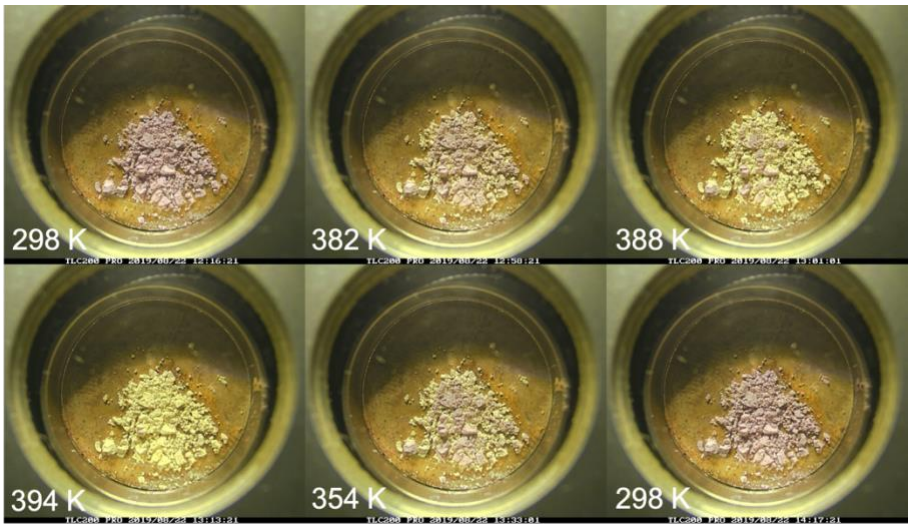

Figure 48: Reflectivity montage of the heating (298 K → 403 K) and cooling (403 K → 298 K) cycles of **2-sol**.

The reflectivity montage seen in Figure *48* reveals the pink → white/yellow SCO transition when heated from 298 K → 403 K. The reflectivity measurements of **2-sol** are shown in *Figure 49* depicting $T_{1/2}\uparrow$ = 384 K, $T_{1/2}\downarrow$ = 354 and ΔT = 30 K with a smoothness of 3 K and 5 K respectively indicating abrupt transitions. Magnetic measurements previously reported reveal abrupt transitions occurring around $T_{1/2}\uparrow$ = 385 K and $T_{1/2}\downarrow$ = 345 K with hysteresis reaching 50 K.[60] This is a $\Delta T_{1/2}\uparrow$ = 1 K and a $\Delta T_{1/2}\downarrow$ = 9 K and a hysteresis difference of 20 K. Hysteresis width is susceptible to change as evidence shows that $T_{1/2}\uparrow$ is subject to incremental increases upon successive cycles, whilst unaffecting $T_{1/2}\downarrow$.[60] The temperature lag across the sample that is intrinsic of the analytical method itself must also be taken into consideration.

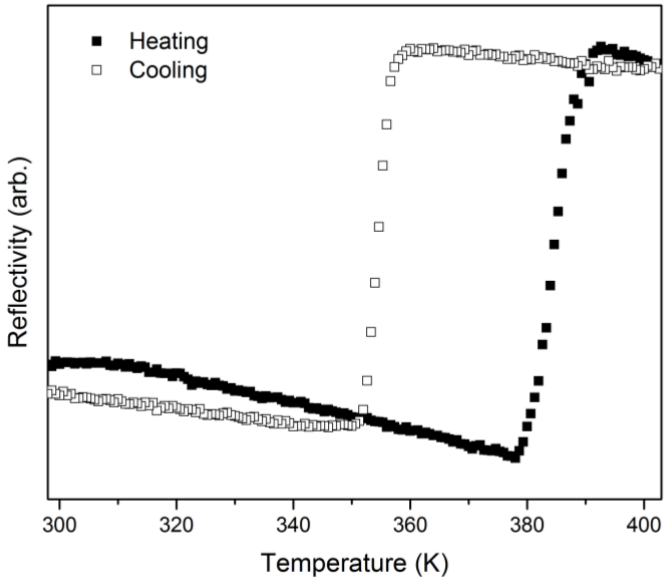

Figure 49: Plot of reflectivity vs. temperature of **2-sol** for the ■ heating and □ cooling cycle.

7.1.3. Conclusion

Structural analysis of Raman and PXRD data confirms that $[Fe(Htrz)_2(trz)](BF_4)$ was successfully synthesized. Reflectivity measurements compared to literature values show a similar $\Delta T_{1/2}\uparrow$ and a slight difference in $\Delta T_{1/2}\downarrow$ with a decrease in the reported hysteresis values of *ca.* 50%. As reflectivity measurements inherently are not as accurate as magnetic measurements, **2-sol** is considered to be suitable as the basis of comparison of the **2-direct** and **2-thin** compounds.

7.2. Direct-contact Synthesis

7.2.1. Experimental

$Fe(BF_4)_2.6H_2O$ (3.825 mmol, 1.5 g) was added to 1*H*-1,2,4-trizaole (11.475 mmol, 0.9649 g) and quickly placed in the SpeedMixer for 10 s. A very light pink complex had formed (**2-direct**), progressing to a darker purple over the course of one hour with residual reagent still remaining.

7.2.2. Results and Discussion

The Raman spectra of the LS and HS spin states of **2-direct**, shown in *Figure 50*, are compared to determine characteristic changes in peaks as a result of structural changes. The LS and HS spectra of **2-direct** were compared to the corresponding spectra of **2-sol** and are shown in *Figure 51* and *Figure 52*, respectively. The **1-direct** LS and HS spectra have corresponding peaks with **2-sol**, respectively. However, in each spin states the peak at 1284 cm^{-1}, attributed to the trz ligand, present in **2-sol** is only very weakly present in **2-direct**. The lack of intensity of the trz peak and the increased intensity of the Htrz peak at 1312 cm^{-1} is indicative that potentially a mixture of $[Fe(Htrz)_3](BF_4)_2$ and $[Fe(Htrz)_2(trz)](BF_4)$ have most likely been synthesized. Upon SCO, numerous peak modifications can be observed. The peak in the LS state at 290 cm^{-1} disappears in the HS

state. Similar to **2-sol**, peaks at 767 cm^{-1}, 1159 cm^{-1}, and 1442 cm^{-1} increase in intensity with the peak at 1538 cm^{-1} decreasing. The double peak at 1062 cm^{-1} and 1079 cm^{-1} displays an overlay and thus present as a single broad peak.

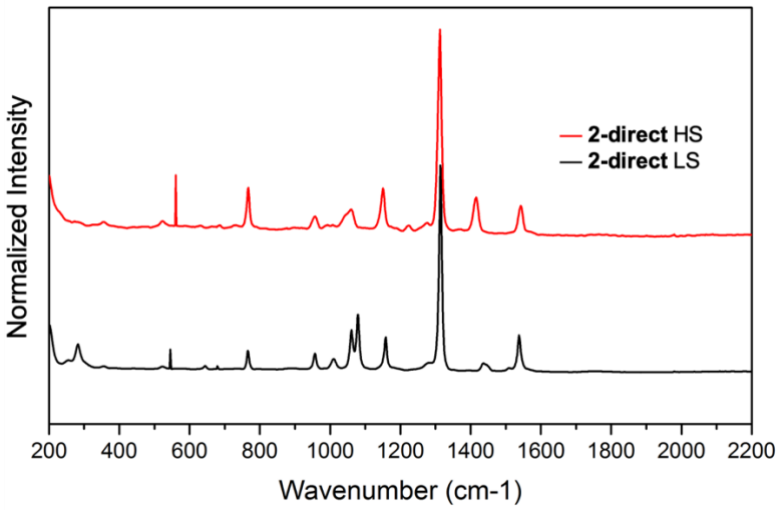

Figure 50: Vibrational spectra of **2-direct** in the — LS (298 K) and — HS state (403 K).

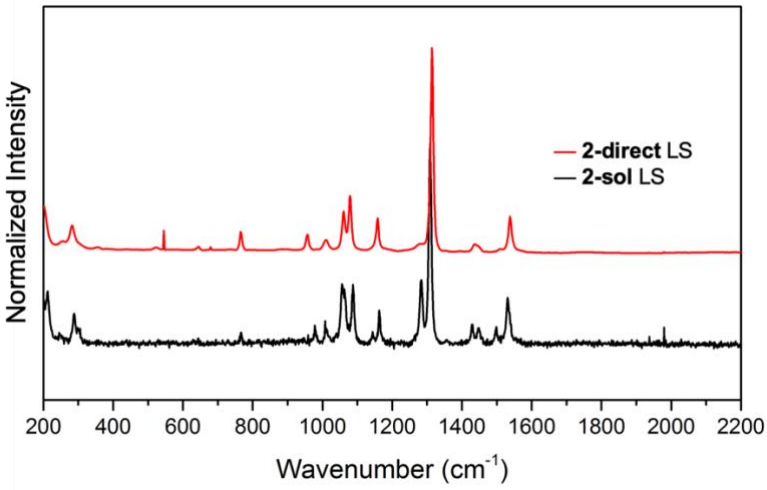

Figure 51: Comparison of vibrational spectra of — **2-sol** and — **2-direct** in the LS state (298 K).

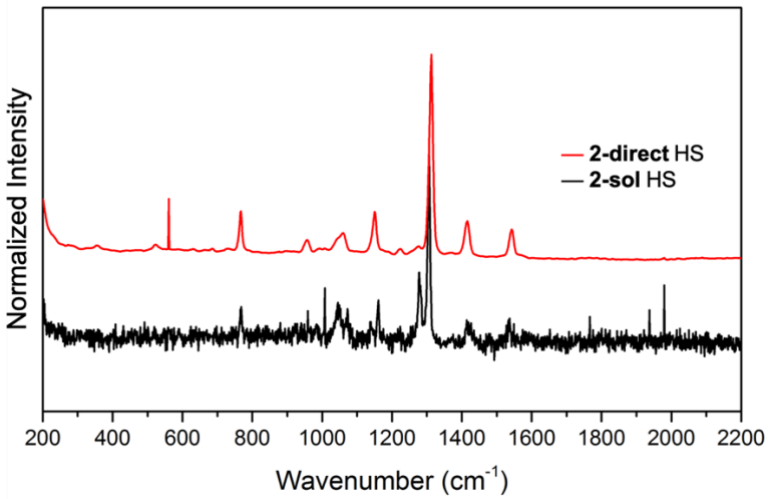

Figure 52: Comparison of vibrational spectra of— **2-sol** and — **2-direct** in the HS state (403 K).

The diffraction patterns of **2-direct** were compared to that of **2-sol** and its constituent reagents, shown in *Figure 53*. The pattern for **2-direct** exhibits very weak intensities with broad peaks consequential of poor crystallinity. The broad peak from 10-70° is most likely due to fluorescence of the sample. The diffraction pattern of **2-direct** has numerous additional peaks present compared to the pattern of **2-sol**, however does weakly exhibit peaks that resemble the pattern of **2-sol**, suggesting that $[Fe(Htrz)_2(trz)](BF_4)$ is present.

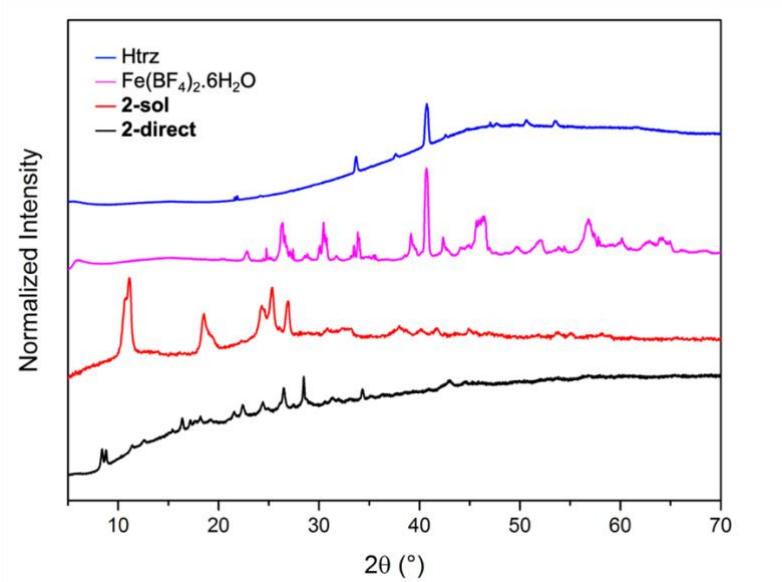

Figure 53: Powder x-ray diffraction patterns of **2-direct** compared to **2-sol** and reagents $Fe(BF_4)_2.6H_2O$ and Htrz.

The additional peaks displayed by **2-direct** do not correspond to the diffraction patterns of the reagents, which is indicative of a multi-phase sample. As this compound is known to exist as two different forms — both with two phases, it is hard to determine which forms/phases are present. PXRD data does not appear to be in the literature to allow for a thorough comparison. Both the PXRD and Raman data support the probable formation of a multi-phase compound via this synthetic method.

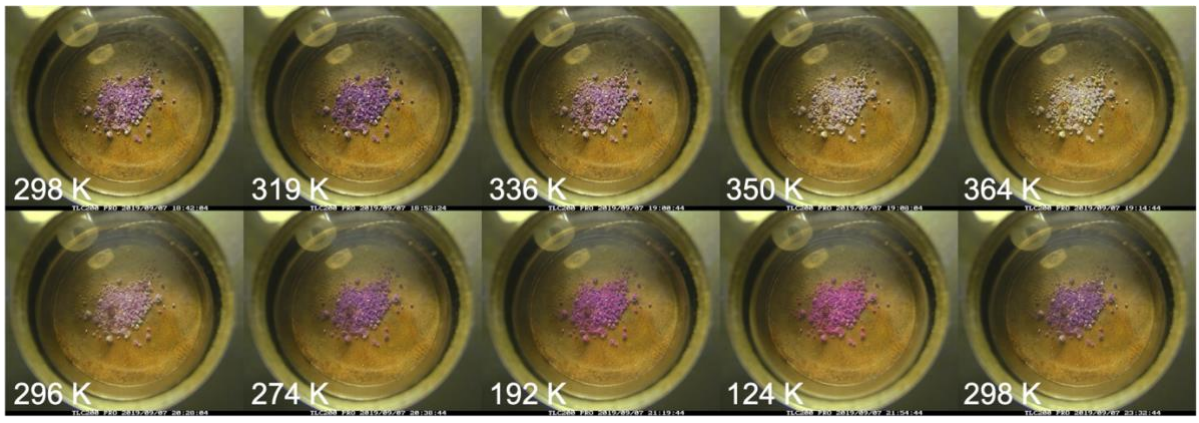

Figure 54: Reflectivity montage of the heating (298 K → 403 K) cooling (403 K → 123 K) and heating (123 K → 298 K) cycles of **2-direct**. From 298 K to 319 K the sample got darker most likely due to further reaction. Upon cooling to 123 K, the sample becomes pinker and then returns to a purple color upon heating back to 298 K which is potential evidence of a multiphase sample.

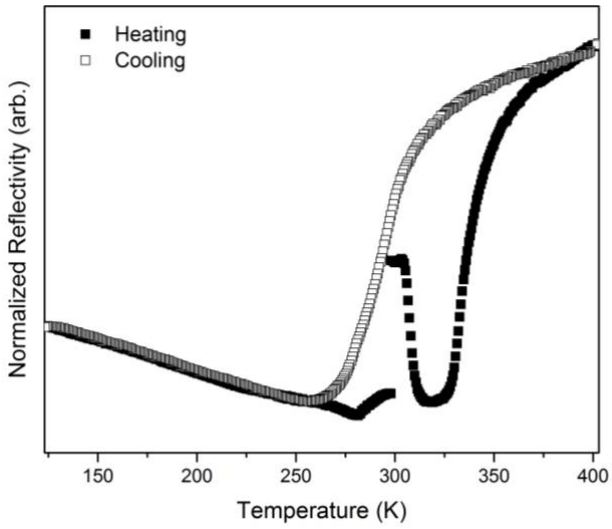

Figure 55: Reflectivity measurements of **2-direct** ■ heating and □ cooling cycles. The sample was heated from 298 K to 403 K, cooled to 123 K and then heated back to 298 K. The sharp decrease from 298 K to 315 K is indicative of further reaction of the sample as a consequence of heat.

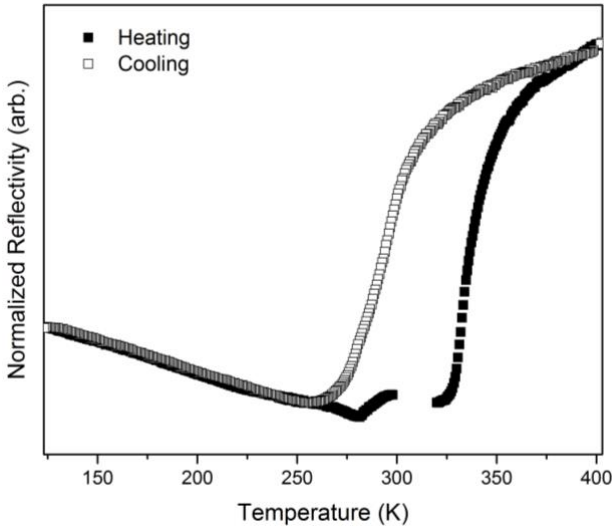

Figure 56: Adapted reflectivity measurement plot of **2-direct** ■ heating and □ cooling cycles, without the sharp decrease from 298 K to 315 K. From this data set, all SCO measurements were calculated.

The reflectivity measurements of **2-direct** can be seen in *Figure 55*. The sample was heated from 298 K to 403 K, then cooled to 123 K and heated back up to 298 K. In the first heating cycle, from 298-315 K there is a sudden increase in color, depicted by the sharp decrease in the reflectivity plot. This is indicative of the sample most likely reacting further due to the introduction of heat and can be seen visually in Figure *54*. For the purpose of SCO measurements, data from 298-315 K was omitted, represented by *Figure 56*. From this, $T_{1/2}$ and their corresponding smoothness were calculated. **2-direct** exhibits an abrupt spin transition with $T_{1/2}\uparrow$ = 332 K and a smoothness of 5 K. The cooling cycle reveals an extremely gradual transition from HS to LS, where $T_{1/2}\downarrow$ = 294 K with a smoothness of 55 K. Notably, this spin transition is below room temperature. The comparison between **2-direct** and **2-sol** and other literary values can be seen in *Table 1*. Out of the four literary compounds in *Table* 1, **2-direct** $T_{1/2}\uparrow$ (332 K) is closer to the $T_{1/2}\uparrow$ value of the hydrated form $[Fe(Htrz)_3](BF_4)_2.H_2O$ (345 K), with a $\Delta T_{1/2}\uparrow$ value of 13 K. The

2-direct $T_{1/2}\downarrow$(294 K) is however closer to the value of dehydrated $[Fe(Htrz)_3](BF_4)_2$ $T_{1/2}\downarrow$ (276 K), with a $\Delta T_{1/2}\downarrow$ value of 18 K. The **2-direct** hysteresis value is calculated to be 38 K; however, this is most likely a consequence of an exceptionally gradual transition upon cooling and thus not indicative of the degree of cooperativity. From this analysis and the visual montage, it is likely that **2-direct** is a multi-phase sample that converts from the hydrated polymorph to the dehydrated polymorph upon heating. Thus, is evident that **2-direct** reflectivity measurements are dissimilar to the reflectivity measurements of **2-sol**.

Table 1: SCO properties for **2-direct** compared to **2-sol** and other literary values.[10,60] * Denotes values reproduced from literature.

Sample	$T_{1/2}\uparrow$ (K)	$T_{1/2}\downarrow$ (K)	$\Delta T_{1/2}$ (K)
2-direct	332	294	38
2-sol	384	354	30
α–[Fe(Htrz)$_2$(trz)](BF$_4$)*	385	350	50
β–[Fe(Htrz)$_2$(trz)](BF$_4$)*	350	325	25
[Fe(Htrz)$_3$](BF$_4$)$_2$.H$_2$O*	345	323	22
[Fe(Htrz)$_3$](BF$_4$)$_2$*	282	276	6

7.2.3. Conclusion

The lack of intensity in the trz peak of the Raman spectroscopy and the presence of additional peaks in the PXRD data indicate the likelihood that **2-direct** is a multi-phase sample. The PXRD pattern of **2-direct** suggests the presence of $[Fe(Htrz)_2(trz)](BF_4)$. The evidence of **2-direct** being a multi-phase sample is further inferred by the reflectivity data. The $T_{1/2}\uparrow$ value is closest to the $T_{1/2}\uparrow$ value of hydrated $[Fe(Htrz)_3](BF_4)_2.H_2O$ whilst the $T_{1/2}\downarrow$ value is closer to the dehydrated $[Fe(Htrz)_3](BF_4)_2$ $T_{1/2}\downarrow$ value. This is potentially a result of the evaporation of water at the higher temperature, thus converting it to the dehydrated phase. As such, it is evident that this is not likely to be the same compound as **2-sol**, and that **2-direct** gives rise to a multi-phase sample. In order to ascertain further information about the phases likely to be present, further analysis will need to be performed. SQUID magnetic measurements would be particularly useful as this would explicitly pinpoint changes in spin state and give $T_{1/2}$ values with a much higher accuracy. VT Raman could also show potential changes in states through various peak transformations at specific temperatures across a range. As water is such a determining factor of SCO, it would be beneficial to acquire Thermogravimetric analysis (TGA) and Differential Scanning Calorimetry (DSC) to establish potential mass loss which could provide insight between the hydrated and dehydrated forms and also indicate any phase changes. This will also likely provide a better understanding of the sharp decrease in reflectivity upon initial heating from 298-315 K.

7.3. Thin-film Synthesis

7.3.1. Experimental

The protocol was followed as stated in **Section 4.4.** with $Fe(BF_4)_2.6H_2O$ (1.481 mmol, 0.5 g) and 1*H*-1,2,4-trizaole (4.444 mmol, 0.3069 g) dissolved separately in 1.2 ml of water – yielding a pink/purple thin film.

7.3.2. Results and Discussion

The Raman spectra was acquired of **2-thin** in both electronic spin states, as seen in *Figure 57*. Both the LS and HS states were then compared to that of **2-sol** and the blank filter paper substrate, seen in *Figure 58* and *Figure 59*. Although the peaks of **2-thin** are significantly less intense than that of **2-sol** due to the compound being adhered to a substrate, peak presence can still be determined and show a comparable pattern to **2-sol**. **2-thin** has peaks at 206 cm^{-1}, 765 cm^{-1}, 958 cm^{-1}, 1007 cm^{-1}, 1059 cm^{-1}, 1163 cm^{-1}, 1281 cm^{-1}, 1310 cm^{-1}, and 1439 cm^{-1} analogous to **2-sol**. Peaks at 381 cm^{-1}, 1097 cm^{-1} and 1120 cm^{-1} are consistent with the peaks present in the substrate spectrum. The slight peak at 1281 cm^{-1} suggests that trz is present and therefore $[Fe(Htrz)_2(trz)](BF_4)$ is likely formed. LS and HS spectra of **2-thin** shows an increase in intensity for peaks at 765 cm^{-1}, 1159 cm^{-1} and 1416 cm^{-1}. Peaks at 1060 cm^{-1}, 1417 cm^{-1} and 1548 cm^{-1} decrease in intensity from LS → HS.

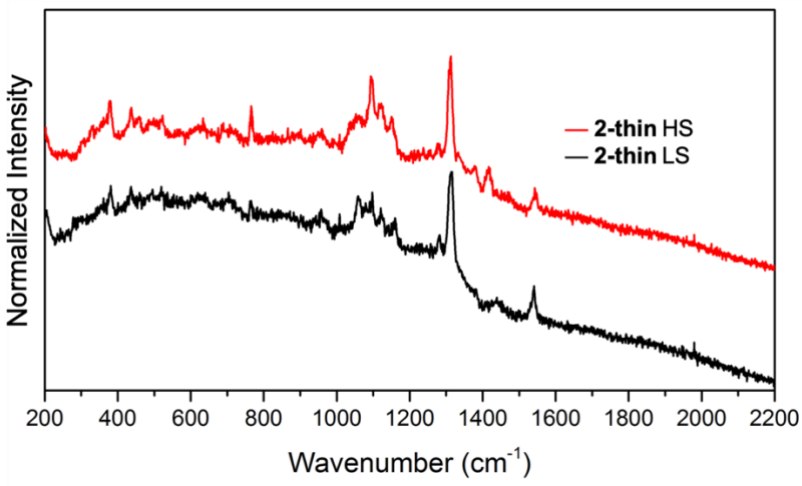

Figure 57: Raman spectroscopy of **2-thin** in the — LS (298 K) and — HS state (403 K).

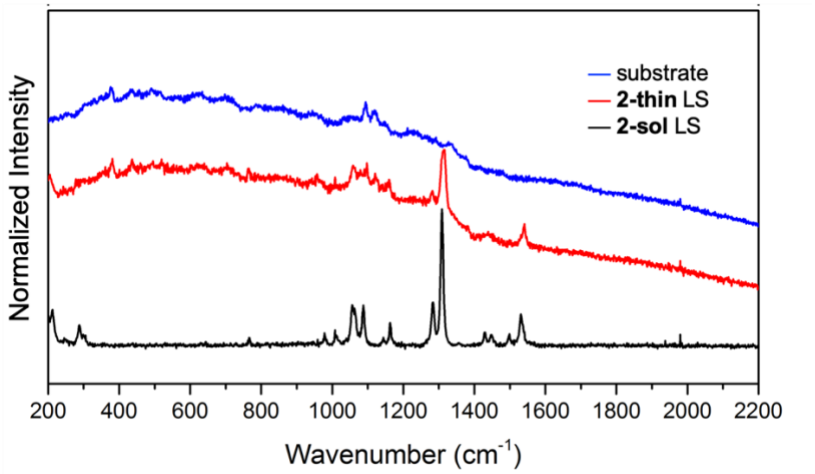

Figure 58: Raman spectroscopy of — 2-**sol**, — **2-thin** and the — substrate in the LS state (298 K).

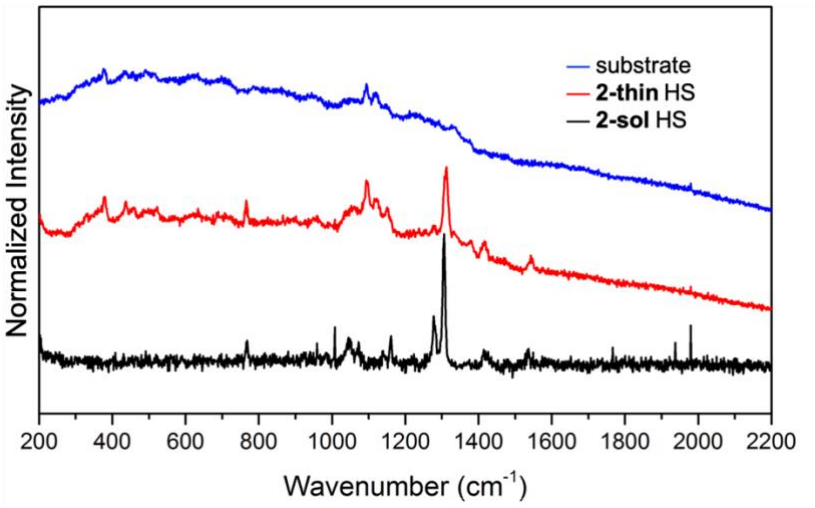

Figure 59: Raman spectroscopy of — **2-sol**, — **2-thin**, and — substrate in the HS state (403 K).

As expected, the PXRD pattern shown in *Figure 60*, of **2-thin** shows weaker intensities than **2-sol** and **2-direct** as a consequence of the high presence of substrate and a small amount of compound. The large amorphous peaks at 15.2˚, 16.3˚ and 22.8˚ of the **2-thin** pattern corresponds to the substrate. Peaks at 10.8˚, 18.5˚, 24˚, 25.1˚, and 26.7˚ are akin to the peaks present in the PXRD data of **2-sol**. There is an unknown peak at 8.1˚ that does not reflect either reagents or **2-sol** but is present in the diffraction pattern of **2-direct**, shown in *Figure 53*. Therefore, it is likely possible that **2-thin** also has more than one phase present.

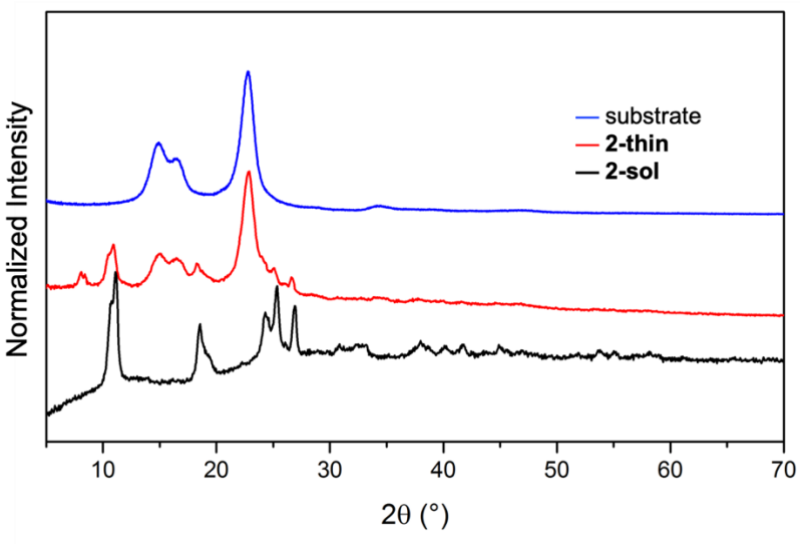

Figure 60: PXRD of — **2-thin**, — **2-sol** and — substrate.

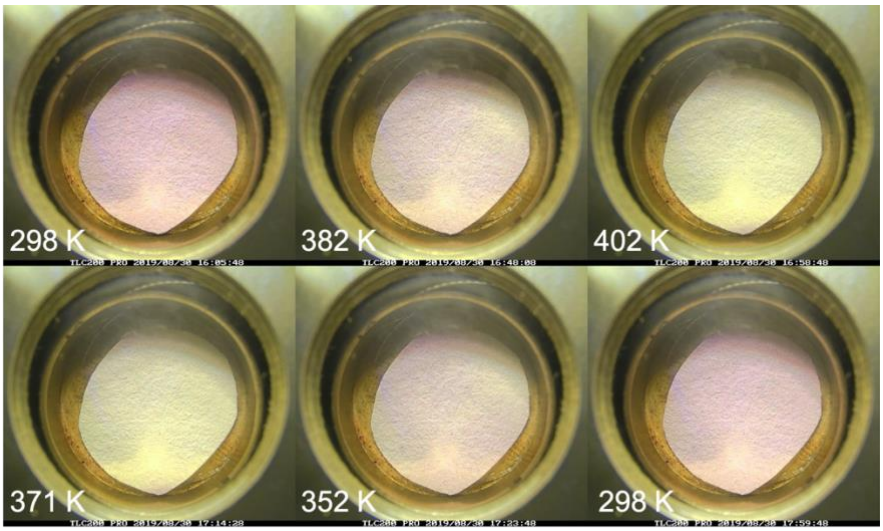

Figure 61: Visual montage of reflectivity measurements of the heating (298 K → 403 K) and cooling cycles (403 K → 298 K) of **2-thin**.

The visual montage of the reflectivity measurements of **2-thin** can be seen in *Figure 61*, which shows the transition of a pink LS → white HS thin film. The film was heated from 298 K → 403 K and cooled back to 298 K. Analysis of this reflectivity data, shown in *Figure 62*, indicates $T_{1/2}\uparrow$ = 387 K and $T_{1/2}\downarrow$ = 353 K with ΔT = 34 K and a smoothness of 1 K and 6 K, respectively. The results of **2-thin** show great similarity to those of **2-sol** with a $\Delta T_{1/2}\uparrow$ = 3 K, $\Delta T_{1/2}\downarrow$ = 1 K and a difference in hysteresis width of 4 K. There is no visible sporadic color change of **2-thin** between 390-400 K, and thus the fluctuation in points is most likely caused by condensation on the glass.

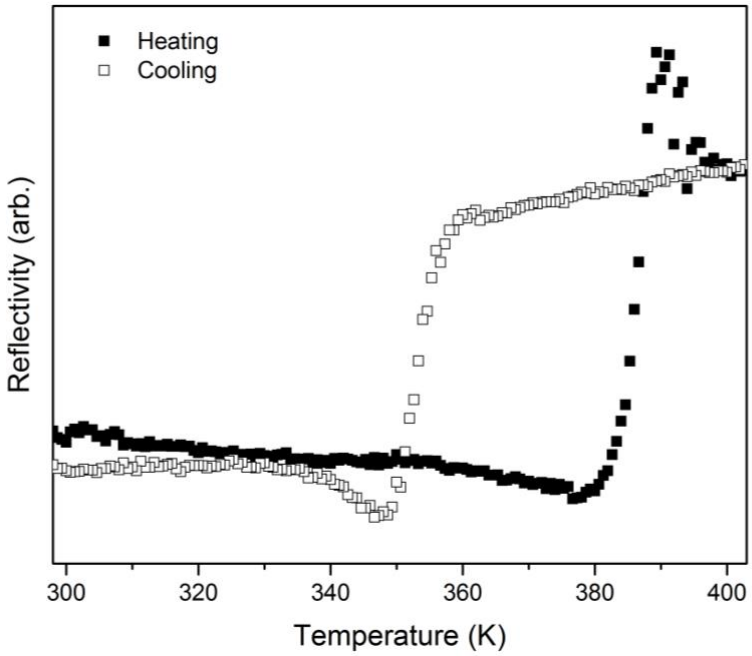

Figure 62: Reflectivity graph of ■ heating and □ cooling cycle of **2-thin**.

7.3.3. Conclusion

The Raman spectroscopy of **2-thin** indicates the presence of the trz^- ligand and thus the likely presence of $[Fe(Htrz)_2(trz)](BF_4)$. PXRD data also mimics the likelihood of the formation of $[Fe(Htrz)_2(trz)](BF_4)$ as the patterns of **2-thin** and **2-sol** are comparable. However, the presence of the additional peak at 8.1˚ is indicative of a potential multi-phase sample, as seen in **2-direct**. The reflectivity data is very similar to that of **2-sol** with only slight variations. Although Raman and reflectivity data suggest that **2-sol** and **2-thin** are likely the same compound, the PXRD data suggests possibly otherwise. To further determine the nature of **2-thin**, VT Raman and TGA/DSC could be conducted. In conclusion, **2-thin** displays similar SCO properties to that of **2-sol** and further analysis is needed to determine the structural information.

7.4. $[Fe(Htrz)_2(trz)](BF_4)$ Conclusion

The Raman in *Figure 63* shows the vibrational spectra for complex **2** formed via *solution-state*, *direct-contact*, and *thin-film* synthesis. The spectra for **2-sol** and **2-thin** are comparably similar, and thus likely form the same compound. The **2-direct** Raman also exhibits similar characteristics; however, the main discrepancy is the near absence of the trz^- peak at 1284 cm^{-1}. This alludes to the prospect that **2-direct** potentially has a different form to that of **2-sol** and **2-thin**. The PXRD patterns of all three synthetic methods are shown in *Figure 64*. With the PXRD of **2-sol** being very similar to the diffraction pattern of $[Fe(Htrz)_2(trz)](BF_4)$ found in the literature, it is most likely that the *solution-state* method forms this compound. The **2-direct** PXRD pattern displays weakly intense peaks that correspond to **2-sol**. However, there are a number of additional peaks that do not correspond to **2-sol** or the reagents which is indicative of another

phase being formed. Thus, it is reasonable to conclude that **2-direct** is most likely a multi-phase compound.

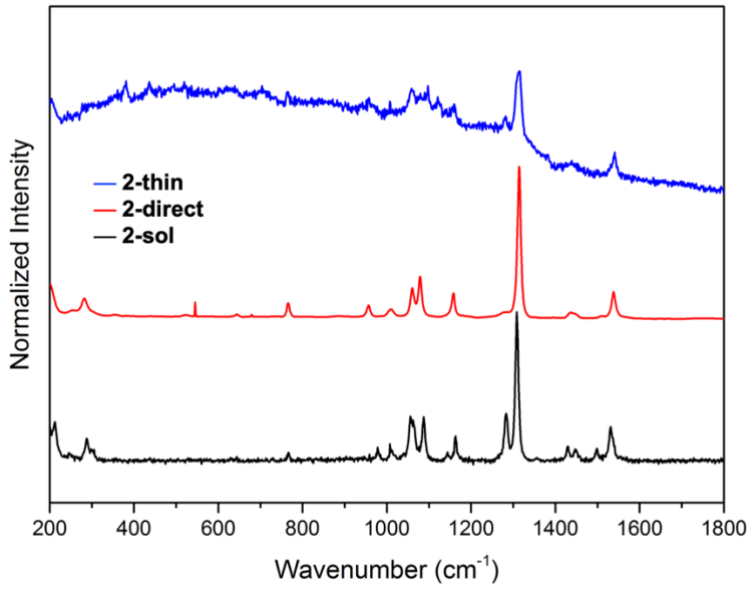

Figure 63: Raman spectroscopy of — **2-sol**, — **2-direct** and — **2-thin** in the LS state (298 K).

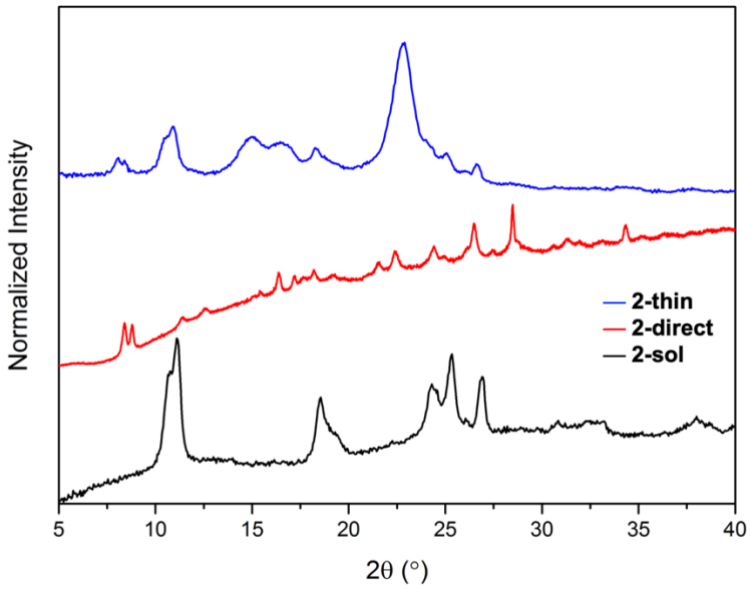

Figure 64: PXRD of — **2-sol**, — **2-direct** and — **2-thin**.

The reflectivity of all three synthetic methods is displayed in *Figure 65*. From the graph it is evident that **2-sol** and **2-thin** have extremely similar $T_{1/2}$ values to each other and to the $[Fe(Htrz)_2(trz)](BF_4)$ literature value, as seen in *Table 2*. **2-direct** exhibits a very different SCO profile. The heating cycle $T_{1/2}\uparrow$ most closely resembles the compound $[Fe(Htrz)_3](BF_4)_2.H_2O$ whilst the cooling cycle $T_{1/2}\downarrow$ most closely resembles the dehydrated form, $[Fe(Htrz)_3](BF_4)_2$ which is below room temperature. This is most likely a cause of eliminating the water from the complex.

In order to further ascertain more information about each compound, particularly **2-direct**, more analytical work needs to be conducted. Analytical techniques such as SQUID, TGA/DSC, and further in-depth VT Raman studies could provide further insight.

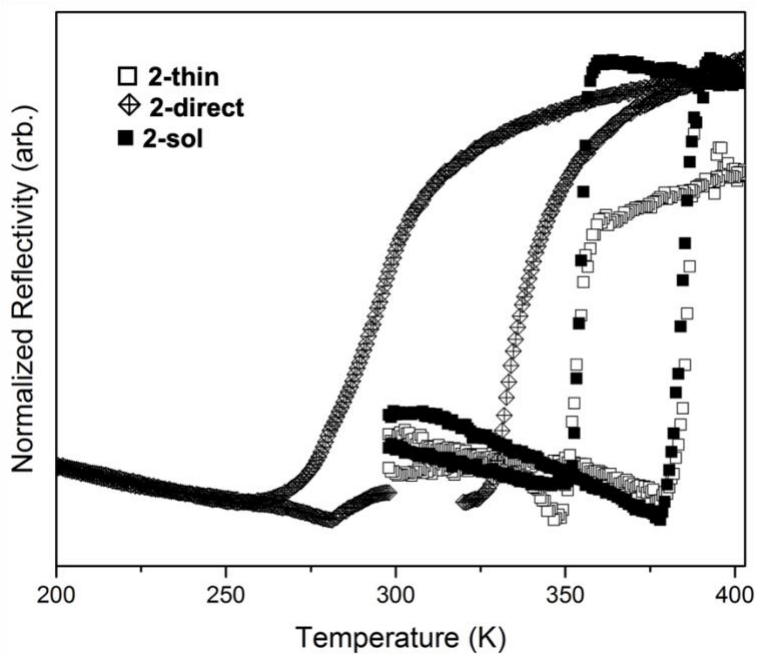

Figure 65: Reflectivity of ■ **1-sol**, × **1-direct** and □ **1-thin**.

Table 2: SCO properties for **2-sol, 2-direct** and **2-thin** compared to literary values.[10,60] * Denotes values reproduced from literature.

Sample	$T_{1/2}\uparrow$ (K)	$T_{1/2}\downarrow$ (K)	$\Delta T_{1/2}$ (K)
2-sol	384	354	30
2-direct	332	294	38
2-thin	387	353	34
α–[Fe(Htrz)$_2$(trz)](BF$_4$)*	385	350	50
β–[Fe(Htrz)$_2$(trz)](BF$_4$)*	350	325	25
[Fe(Htrz)$_3$](BF$_4$)$_2$.H$_2$O*	345	323	22
[Fe(Htrz)$_3$](BF$_4$)$_2$*	282	276	6

In conclusion, it is most likely that the *solution-state* and the *thin-film* methods synthesize [Fe(Htrz)$_3$](BF$_4$)$_2$.H$_2$O, whilst the *direct-contact* method synthesizes [Fe(Htrz)$_3$](BF$_4$)$_2$.H$_2$O. Further analysis such as TGA/DSC and magnetic measurements is required to gain more of an understanding.

8. [Fe(atrz)$_3$](BF$_4$)$_2$

The final compound of this investigation is [Fe(atrz)$_3$](BF4)$_2$. This compound was first reported by *Kahn* et al[13] in 1992 with SCO occurring very gradually below room temperature. The transition temperature was reported as $T_{1/2}\uparrow$ = 260 K and $T_{1/2}\downarrow$ = 248 K. In 1995, *Lavrenova* et al[63] reported conflicting SCO properties with $T_{1/2}\uparrow$ = 335 K $T_{1/2}\downarrow$ = 307 K. This is particularly interesting as the SCO was purportedly above room temperature. *Roubeau*[7] later confirmed the properties stated by Kahn with $T_{1/2}\uparrow$ = 260 K and $T_{1/2}\downarrow$ = 250 K. *Grosjean* reportedly identified a new β phase

of this complex with $T_{1/2}\uparrow$ = 245 K and $T_{1/2}\downarrow$ = 239 K.[64] This phase has a lower transition temperature and is less crystalline than the α phase reported by *Kahn* and *Roubeau*.

8.1. Solution-state Synthesis

8.1.1. Experimental

$Fe(BF_4)_2.6H_2O$ (1.481 mmol, 0.5 g) was dissolved in 3 ml of water and added to a solution of 4-aminotriazole (4.4443 mmol, 0.3736 g) dissolved in 2 ml of water. A white precipitate (**3-sol**) was formed and was filtered and washed with water and left to air dry.

8.1.2. Results and Discussion

The Raman spectra of the LS and HS states of **3-sol** can be seen in *Figure 66* and were acquired at 223 K and 298 K, respectively. As the spin transition is below room temperature, the compound resides in the HS state at room temperature. Numerous peak transformations are observed upon switching from LS → HS. The peak at 252 cm^{-1} (LS) shifts to a lower wavenumber and outside the range of analysis in the HS state. The intensity of peaks at 357 cm^{-1}, 523 cm^{-1}, 693 cm^{-1}, 765 cm^{-1} and 1098 cm^{-1} increase in the HS state whilst peaks at 1464 cm^{-1} and 1554 cm^{-1} show a decrease in intensity. The width of the peak at 1347 cm^{-1} also shows a slight increase from LS → HS. These changes in peak intensity, width and wavenumber are evidence of an SCO transition within the complex.

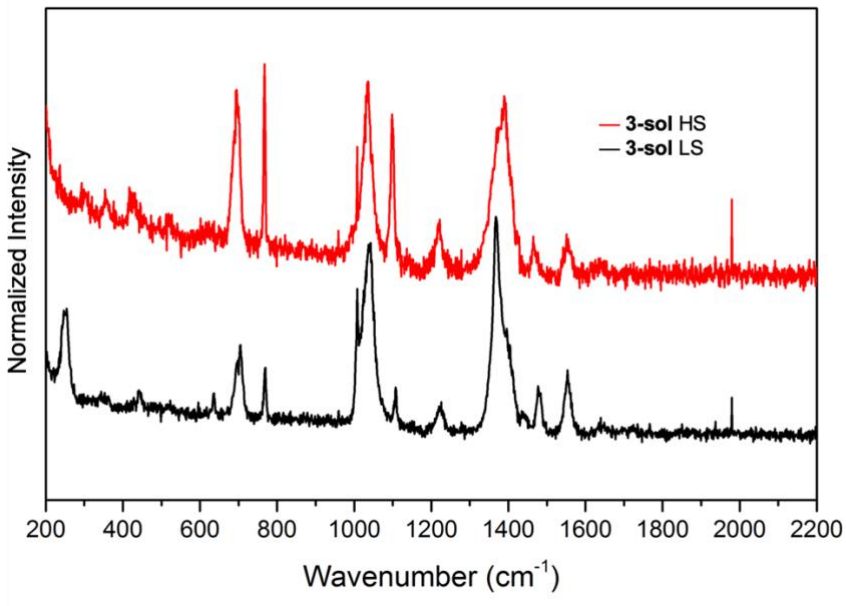

Figure 66: Raman spectroscopy of **3-sol** in — LS (223 K) and — HS (298 K) states.

In order to ascertain if **3-sol** was in fact $[Fe(atrz)_3](BF4)_2$, the PXRD pattern was obtained, seen in *Figure 67*, and compared to a diffraction pattern in the literature, shown in *Figure 68*.[64] The PXRD of **3-sol** exhibits strong fluorescence which is evident from the large broad peak across

the spectra. Nonetheless, the Braggs peaks are prominent and show analogous similarities with the literature 1-sol sample from *Figure 68* with no additional peaks. Thus, **3-sol** is likely to be the α phase of $[Fe(atrz)_3](BF4)_2$.

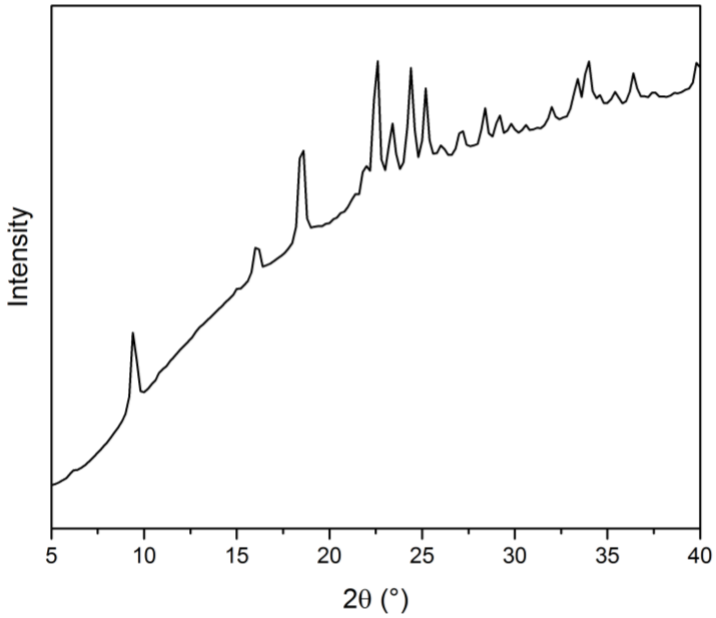

Figure 67: PXRD of **3-sol**.

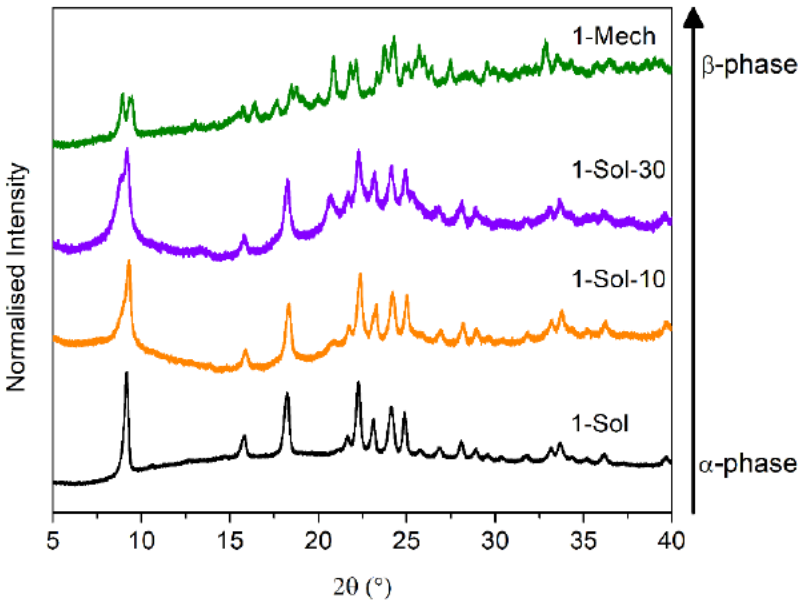

Figure 68: Normalized PXRD of $[Fe(atrz)_3](BF_4)_2$. Reproduced from reference.[64]

The reflectivity of **3-sol**, shown in Figure *69*, depicts the cooling and heating cycle from 298 K $\rightarrow$ 203 K $\rightarrow$ 298 K. The reflectivity values reveal $T_{1/2}\uparrow$ = 211 K and $T_{1/2}\downarrow$ = 261 K and a hysteresis value of 50 K. This data is exceptionally atypical as it suggests that the cooling cycle has a higher transition temperature than the heating cycle. This has never been reported within the SCO community. Perhaps it is possible that the compound experienced a thermal phase transition on cooling, however this has not been reported for $[Fe(atrz)_3](BF4)_2$, and thus it is improbable. It is

more likely that there was a systematic error within the Linkam temperature stage and that the temperature readings are incorrect and unreliable. Nonetheless, the reflectivity montage in Figure *70* displays a slight color change from white → pink. The montage is also indicative that the temperatures were misaligned as it is expected for $[Fe(atrz)_3](BF4)_2$ to go a darker pink color than observed here. This faint change could therefore be revealing an incomplete transition where the temperature did not cool as much as it was supposed to.

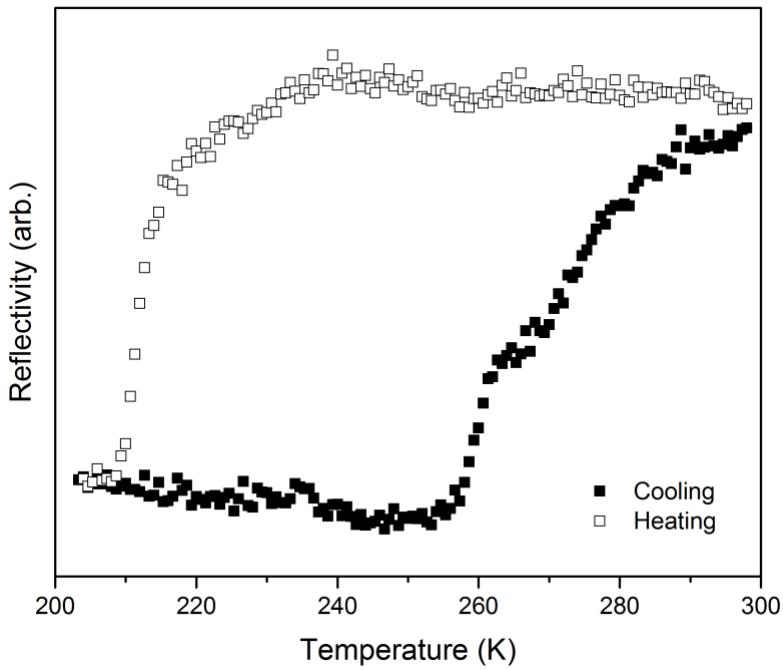

Figure 69: Reflectivity of ■ cooling (298 K → 203 K) and □ heating cycles (203 K → 298 K) of **3-sol**. However, these values are anomalous and most likely the result of a systematic error.

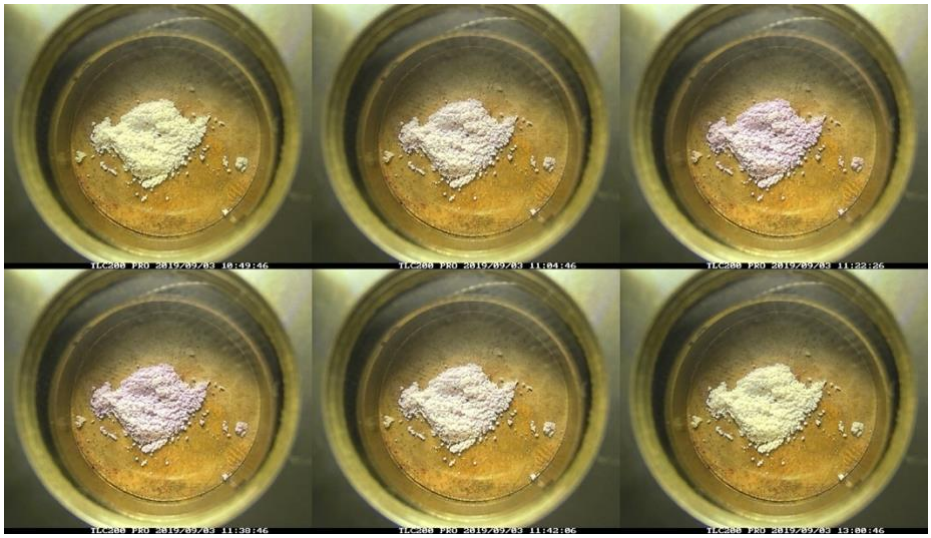

Figure 70: Reflectivity of the cooling (298 K → 203 K) and heating (203 K → 298 K) cycles of **3-sol**. The temperature is not included as these values are incorrect. However, these images are evidence that an SCO material that transitions from white → pink was synthesized.

8.1.3. Conclusion

The Raman data depicts the SCO occurrence of **3-sol** by the peak transformations that are evident from disparities in peak intensities and frequencies. These discrepancies between spin states are indicative that an SCO transition has occurred. The powder diffraction pattern of **3-sol** is analogous to the diffraction pattern of the α phase of $[Fe(atrz)_3](BF4)_2$ from the literature.[64] The reflectivity measurements have been regarded as inaccurate and unreliable which is consequential of a probable systematic experimental error. However, the reflectivity montage does show an optical change from white $\rightarrow$ pink. Regardless of the reflectivity $T_{1/2}$ values, it is evident that a spin active compound was synthesized, and from the diffraction data it is highly likely that **3-sol** is the α phase of $[Fe(atrz)_3](BF4)_2$.

8.2. Direct-contact Synthesis

8.2.1. Experimental

$Fe(BF_4)_2.6H_2O$ (4.444 mmol, 1.5 g) was added to 4-aminotriazole (13.331 mmol, 1.121 g) and quickly added to the SpeedMixer and mixed for 10 s. A white complex (**3-direct**) was formed with residual reagent and was left to react for an hour.

8.2.2. Results and Discussion

The Raman spectra of **3-direct**, shown in *Figure 71*, was acquired in the LS and HS states at 223 K and 298 K, respectively. The spin states were compared to determine characteristic peak transformations. Notably, the peaks at 200 cm^{-1}, 424 cm^{-1}, 694 cm^{-1}, 769 cm^{-1}, and 1100 cm^{-1} increase in intensity from LS $\rightarrow$ HS. There is also a decrease in intensity exhibited by the peak at 287 cm^{-1}. The double peak in the LS state at 1366 cm^{-1} and 1400 cm^{-1} transforms into a single peak with a shoulder which could be due to an overlap of peaks. Therefore, the peak at 1366 cm^{-1} could also be considered to decrease in intensity. The splitting of the peak in the LS state of the peak at 430 cm^{-1} also becomes a single peak in the HS state.

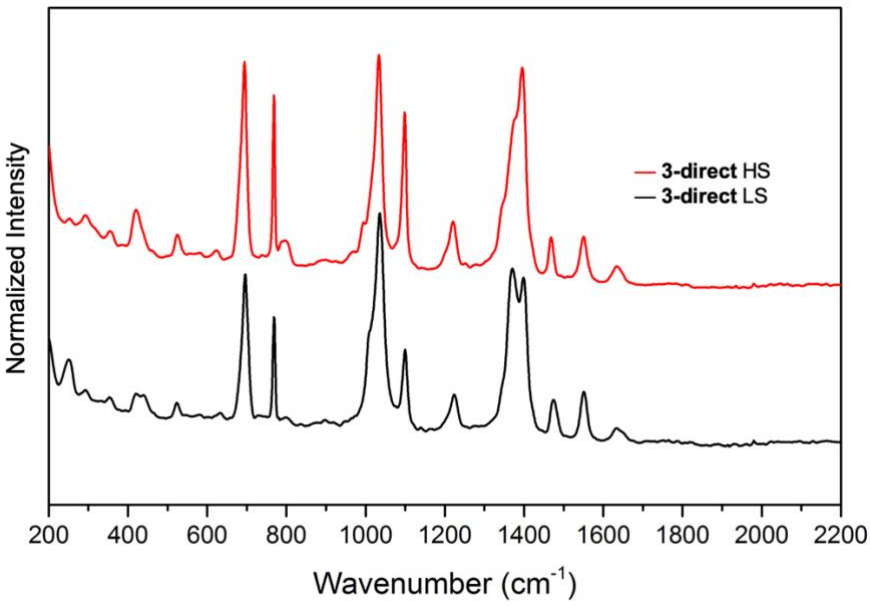

Figure 71: Raman of **3-direct** — LS (123 K) and — HS states (298 K).

The Raman spectra of the LS and HS states of **3-direct** were compared to the corresponding **3-sol** spectra to determine congruency between the 'fingerprints.' The LS comparison, shown in *Figure 72*, shows that **3-direct** has a similar peak pattern with corresponding peaks to the spectra of **3-sol**. There are a couple of differences exhibited in peak intensities *i.e.* the peaks at 254 cm^{-1} and 1553 cm^{-1} are more intense in **3-sol**. Conversely, the peaks at 694 cm^{-1}, 769 cm^{-1}, and 1100 cm^{-1} are more intense in **3-direct**. The **3-sol** compound also does not exhibit the double peak at 1366 cm^{-1} and 1400 cm^{-1}. The HS comparison, shown in *Figure 73*, displays very similar 'fingerprints' regarding peak position and peak intensities.

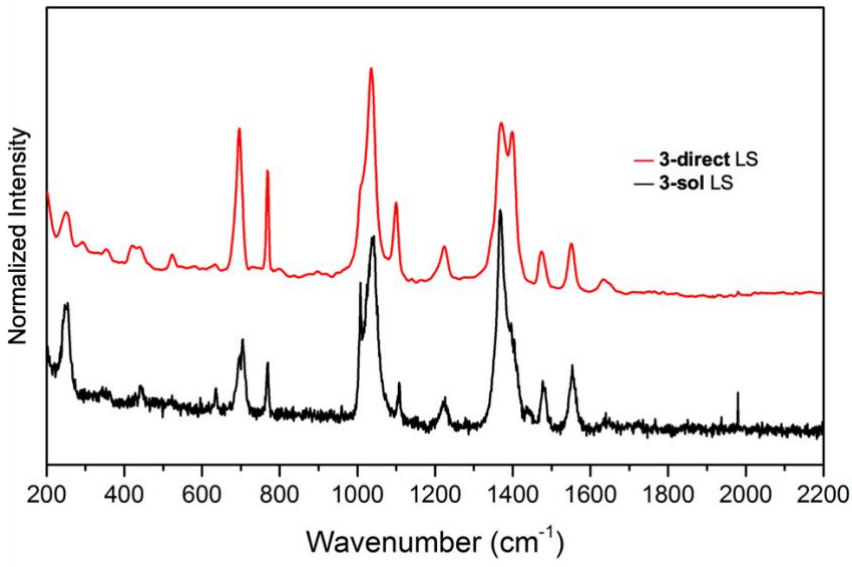

Figure 72: LS state comparison of — **3-sol** and — **3-direct** at (123 K).

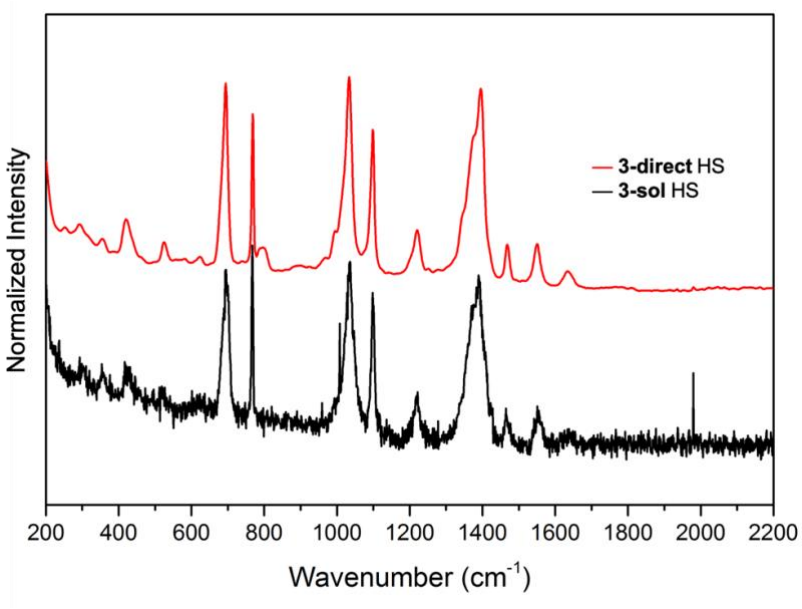

Figure 73: HS state of — **3-direct** and — **3-sol** (298 K).

To further ascertain the compound formed by **3-direct**, PXRD data was acquired and compared to the diffraction patterns of **3-sol** as seen in *Figure 74*, and the patterns from the literature in *Figure 68*. The diffraction pattern of **3-direct** has very broad, weakly intense peaks that are indicative of a more amorphous, less crystalline compound. The ill-defined peaks make it hard to determine the congruency between **3-direct** and **3-sol**. However, the pattern of **3-direct** does not appear to be comparable to **3-sol**. When compared to the diffraction patterns from the literature in *Figure 68*, **3-direct** is most similar to the 1-Mech phase, which is indicative of the β-phase.[64] The presence of the split peak at 9.4˚ is consistent with the β-phase.

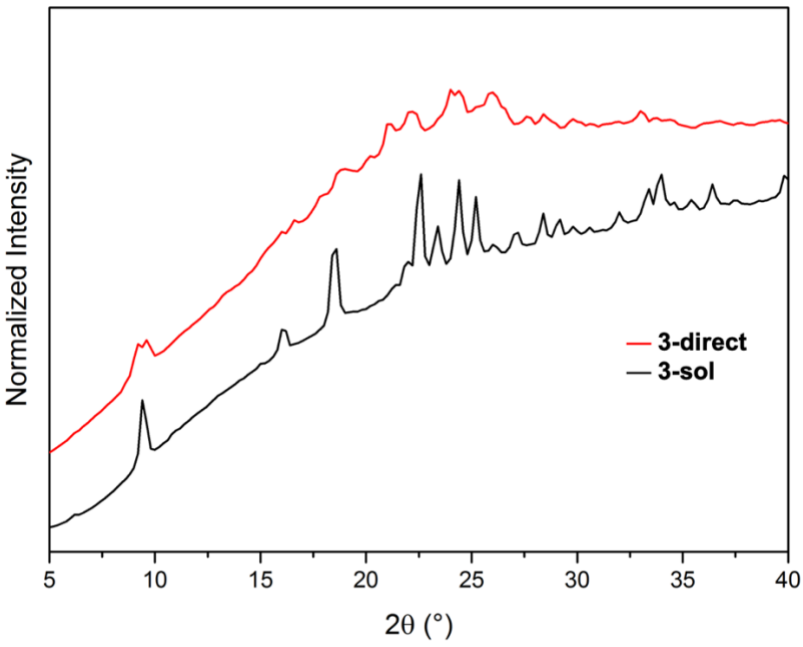

Figure 74: Powder x-ray diffraction pattern of — **3-direct** and — **3-sol**.

The reflectivity data can be seen in *Figure 75*, and reveals a two-step transition in both the cooling (298 K → 123 K) and heating cycles (123 K → 298 K). The cooling cycle $T_{1/2}$ values are

$T_{1/2}\downarrow$ = 212 K and $T_{1/2}\downarrow$ = 237 K, and the heating cycles, $T_{1/2}\uparrow$ = 179 K and $T_{1/2}\uparrow$ = 192 K. Two-step transitions have been reported for $[Fe(atrz)_3](BF4)_2$[64], however like the reflectivity of **3-sol**, this data suggests that the cooling cycle $T_{1/2}\downarrow$ has a higher transition temperature than $T_{1/2}\uparrow$. Again, a thermal phase change could be possible; however, it is more likely that this is a consequence of a systematic experimental error, and the temperatures recorded are not the actual temperature of the sample. Therefore, the reflectivity data and the $T_{1/2}$ values are unreliable and inaccurate. However, the montage in Figure *76* shows an SCO active compound that transitions from white → pink upon cooling below room temperature.

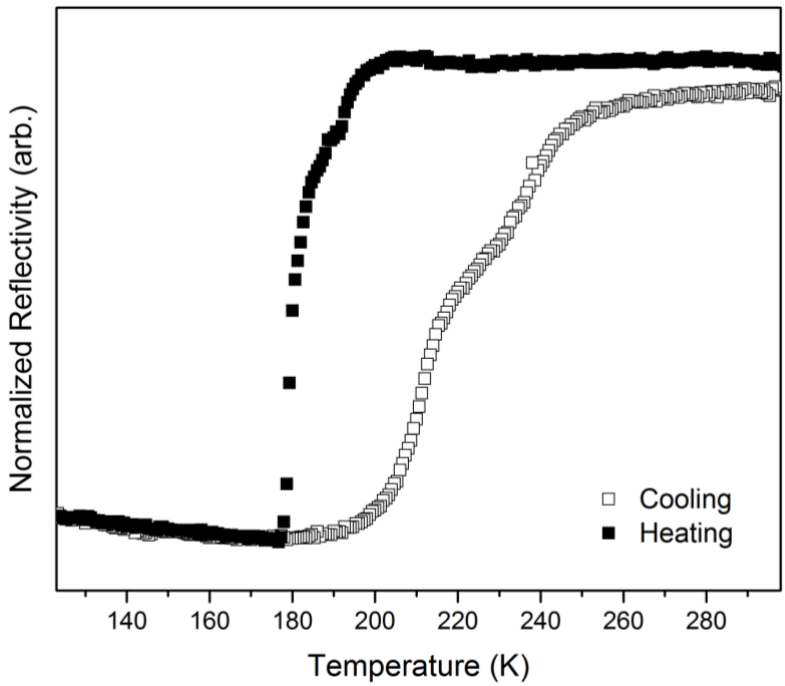

Figure 75: Normalized reflectivity as a function of temperature plot showing the □ cooling (298 K → 123 K) and ■ heating (123 K → 298 K) cycles. However, these values are anomalous and most likely the result of a systematic error.

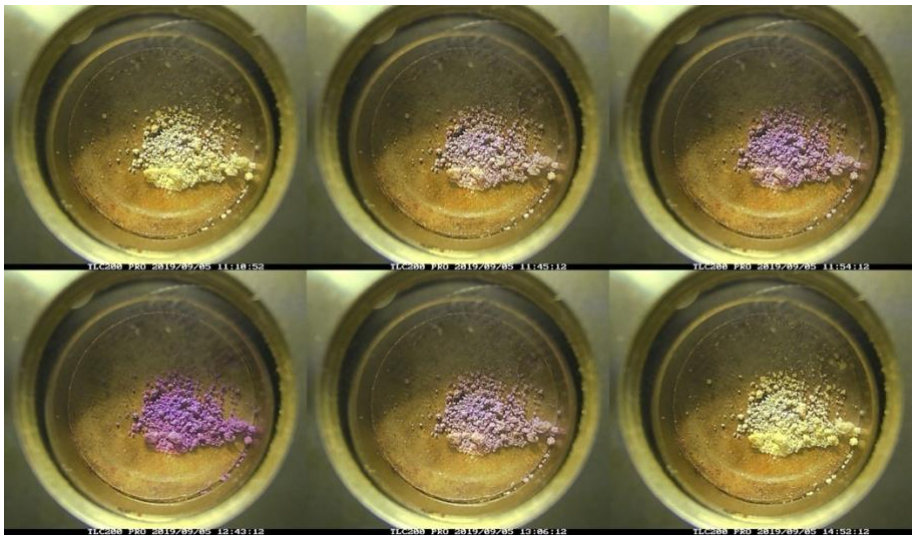

Figure 76: Reflectivity montage of the cooling and heating cycles of **3-direct**. Due to systematic error, temperature readings are not included. However, this clearly shows that an SCO active material that transitions from white/yellow → pink was synthesized.

8.2.3. Conclusion

The Raman spectra of **3-direct** shows a very similar pattern to **3-sol**. However, the PXRD data do not assimilate and thus they are unlikely to be the same complex. The comparison of **3-direct** to the PXRD in the literature from Figure *68* indicates that **3-direct** corresponds to the β phase of $[Fe(atrz)_3](BF_4)_2$, most notable for the split peak present at 9.4°. The reflectivity data depicts the formation of a spin active complex evident from the color change in the montage, however these results do not quantify the SCO profile as they are most likely a result of a systematic error.

8.3. Thin-film Synthesis

8.3.1. Experimental

$Fe(BF_4)_2.6H_2O$ (1.481 mmol, 0.5 g) was dissolved in 3 ml of water and added to a solution of 4-aminotriazole (4.4443 mmol, 0.3736 g). The process was repeated as stated in **Section 4.4**. A white precipitate (**3-thin**) formed on the substrate

8.3.2. Results and Discussion

The Raman spectra of **3-thin** in the LS or HS states were acquired and compared to the respective spectra of **3-sol** and can be seen in Figure *77* and Figure *78*. The broad peak spanning across the spectra of **3-thin** can be attributed to the fluorescence of the substrate. Although the peaks are substantially less intense, likely due to a smaller amount of product and the presence of a substrate, the peaks of **3-thin** show comparable similarities to **3-sol**. Peaks at 254 cm^{-1}, 382 cm^{-1}, 436 cm^{-1}, 458 cm^{-1}, 524 cm^{-1}, 700 cm^{-1}, 769 cm^{-1}, 1008 cm^{-1}, 1025 cm^{-1}, 1095 cm^{-1}, 1354 cm^{-1}, 1475 cm^{-1}, 1480 cm^{-1}, and 1564 cm^{-1} all correspond to peaks also present in **3-sol**. A peak in **3-thin** at 1123 cm^{-1} does not appear in **3-sol** but could potentially be present and not distinguishable from the signal to noise ratio.

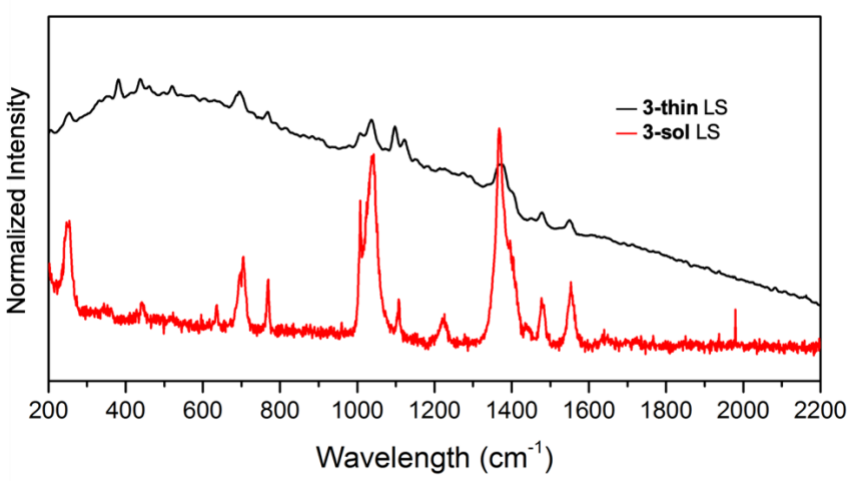

Figure 77: Raman of **3-thin** and **3-sol** in the LS state.

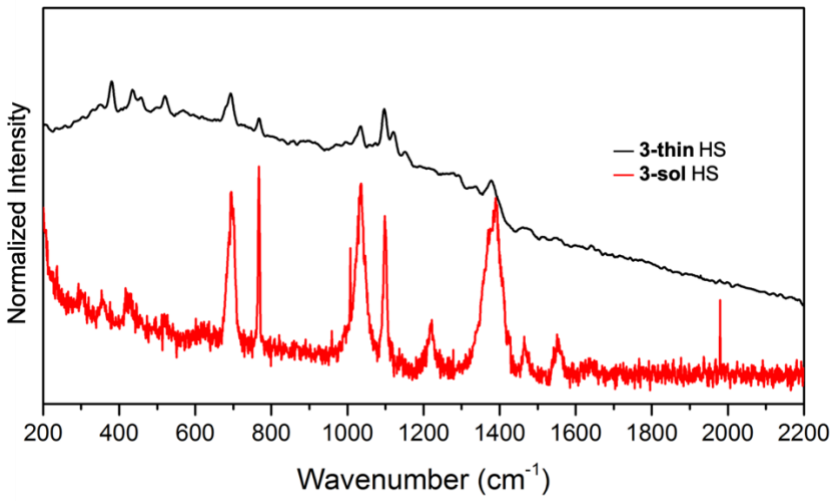

Figure 78: Raman of **3-thin** and **3-sol** in the HS state.

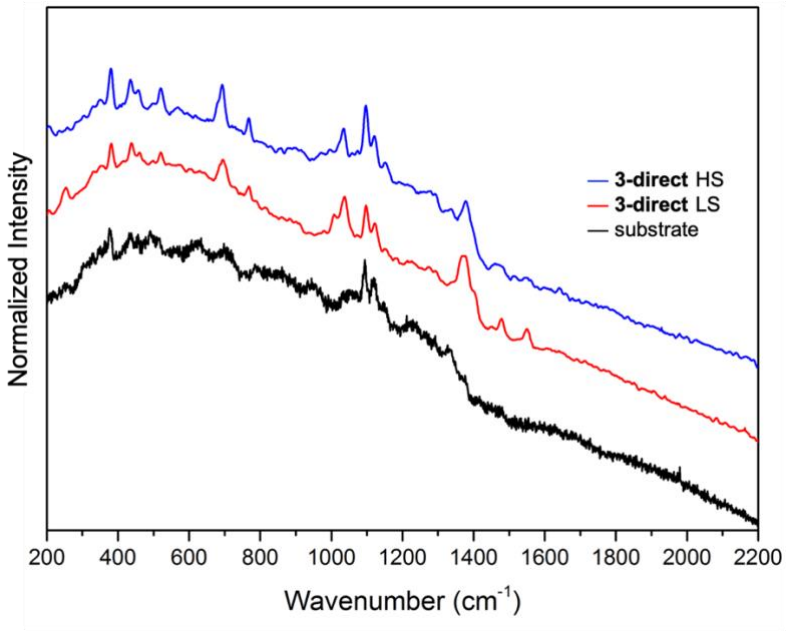

Figure 79: Raman of **3-thin** in the HS and LS state with a blank substrate.

The LS and HS spectra of **3-thin** are directly compared in Figure *79*. Although subtle differences, the HS spectra does show some differences in peak intensities and frequencies. The peak present at 250 cm^{-1} in LS shifts to a lower frequency of 208 cm^{-1} in HS. Notable increases in intensity from LS → HS are peaks at 382 cm^{-1}, 436 cm^{-1}, 458 cm^{-1}, 524 cm^{-1}, 691 cm^{-1}, 767 cm^{-1}, 1095 cm^{-1}, 1120 cm^{-1}, and 1154 cm^{-1}. The peaks at 1008 cm^{-1} and 1481 cm^{-1} exhibit a decrease in intensity. The LS and HS differences in intensities and frequencies are evidential of spin crossover with peak frequencies corresponding to that of **3-sol**.

The PXRD pattern of **3-thin**, shown in Figure *80*, shows extremely weak broad peaks. The large peak at 23.6° and potentially the peaks at 15.8° and 17.4° correspond to the substrate. There is a broad peak at 9.8° that resembles the **3-direct** split peak more so than the single peak of **3-sol**. The weakness in intensity is likely due to the amorphous nature of the substrate and complex and also the small amount present. It is difficult to ascertain with certainty which phase of $[Fe(atrz)_3](BF_4)$ was synthesized.

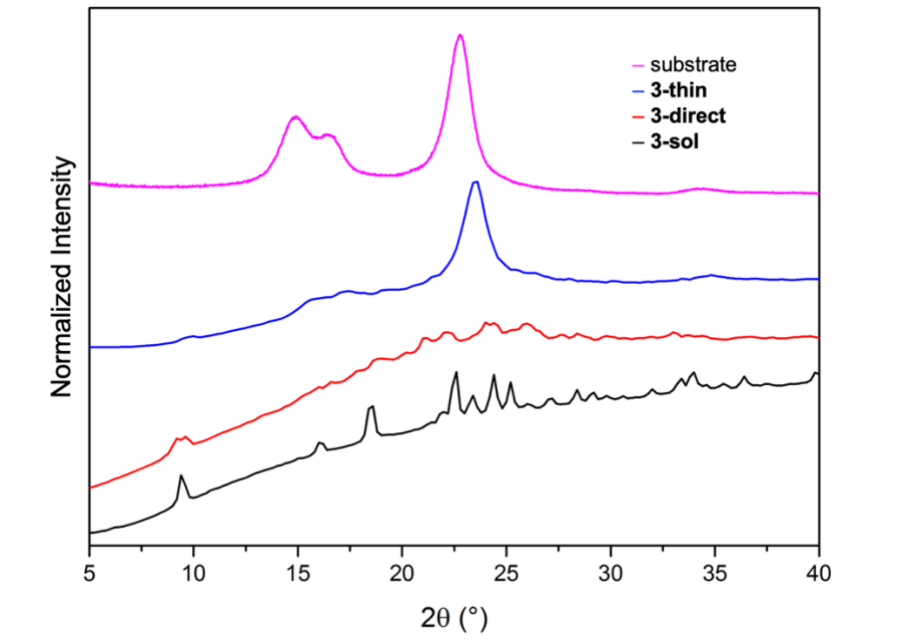

Figure 80: PXRD of – **3-sol**, – **3-direct** and – **3-thin** methods and – blank substrate.

The reflectivity data can be seen in Figure *81*. The complex was cooled to 123 K and heated back to 298 K and revealed $T_{1/2}\downarrow$ = 247 K and $T_{1/2}\uparrow$ = 211 K. However, similar to the two previous synthetic methods, this data suggests that $T_{1/2}\downarrow$ has a higher transition temperature than $T_{1/2}\uparrow$ which has never been reported before. This is mostly due to a systematic error giving false temperature readings rather than an intrinsic thermal phase change occurring. Thus, resulting in unreliable and inconclusive $T_{1/2}$ values. However, the reflectivity montage in Figure *82* does demonstrate that a spin crossover material was synthesized that transitions from white → pink upon cooling below room temperature.

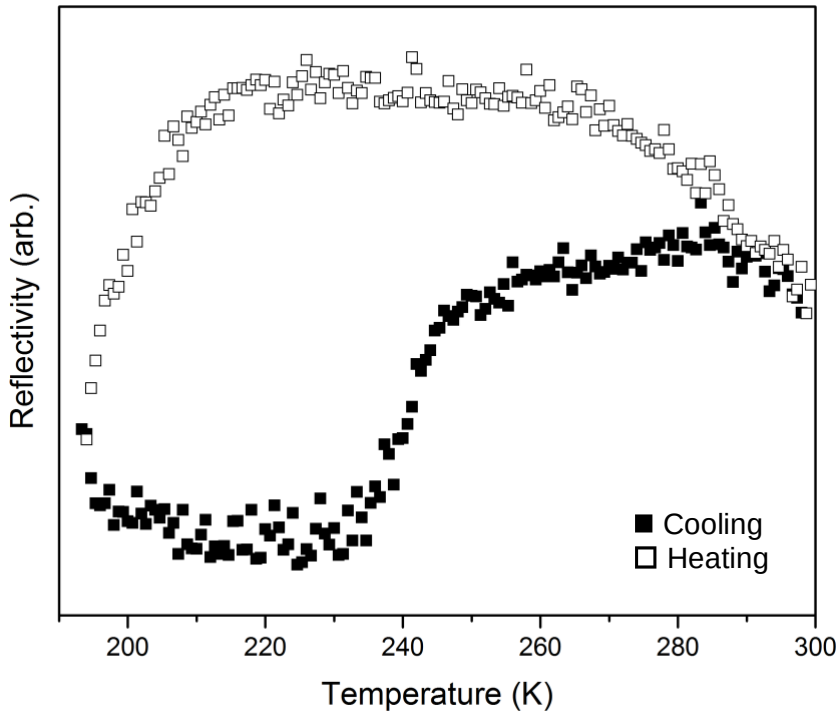

Figure 81: Reflectivity of the ■ heating and □ cooling cycles of **3-thin**.

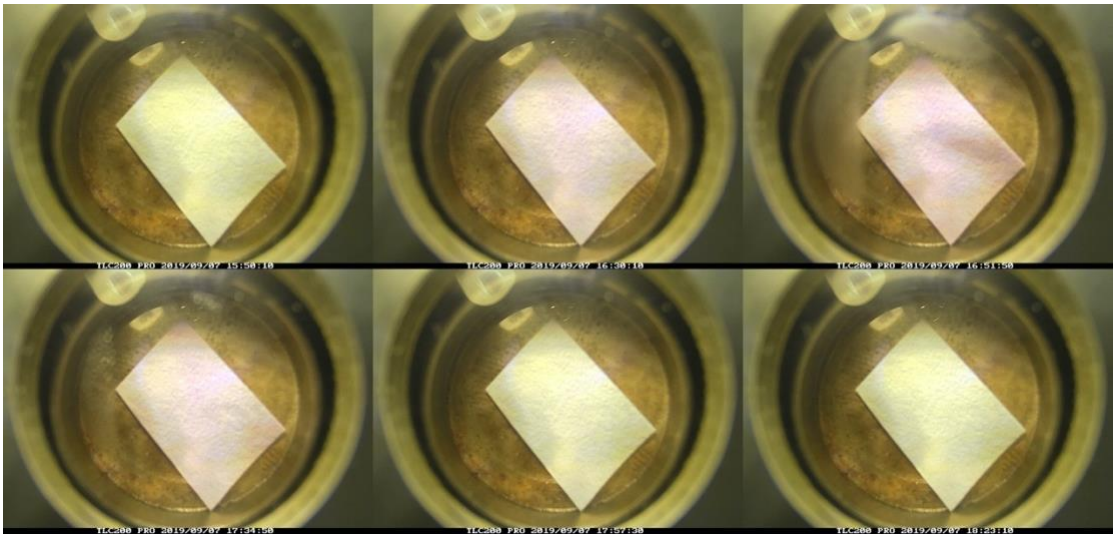

Figure 82: Reflectivity montage of the cooling and heating cycles of **3-thin**. Due to systematic error and thus inaccurate temperatures, temperature readings are not included. However, this montage demonstrates that an SCO active material that transitions from white → pink was synthesized.

8.3.3. Conclusions

The LS Raman spectra for each synthetic technique are shown in Figure *83*. The spectra show comparable peak characteristics, and it is therefore likely that each method likely synthesizes the same compound.

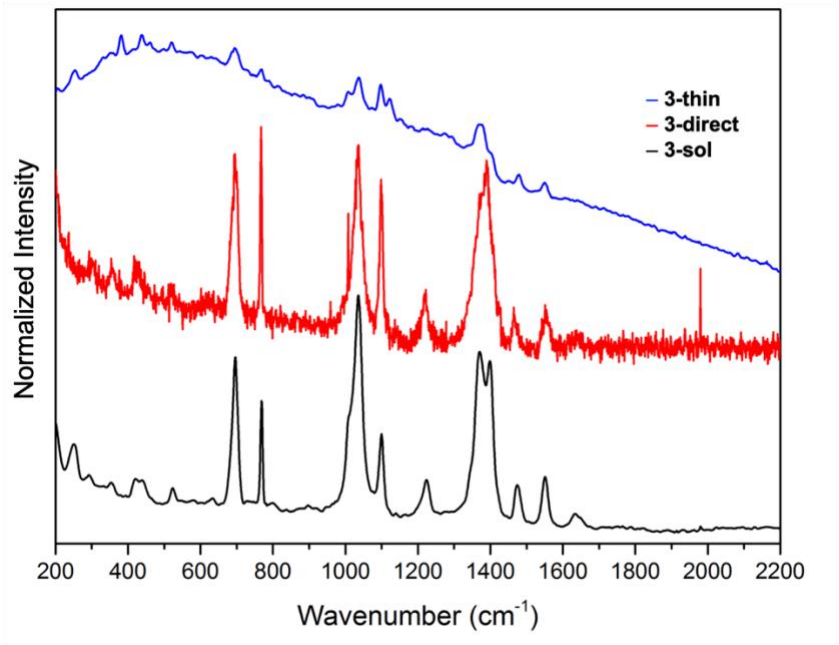

Figure 83: Raman spectra of – **3-sol**, – **3-direct**, and – **3-thin** in LS acquired at 123 K.

Further investigation into the PXRD pattern comparisons shown in Figure *80* and the literature, it is likely that **3-sol** synthesizes the α polymorph of $[Fe(atrz)_3](BF_4)_2$ and **3-direct** synthesizes the β polymorph. The low intensity of **3-thin** makes it hard to ascertain with certainty which form is most likely synthesized by the thin film synthetic method and thus further analysis must be done.

As the reflectivity measurements are a result of a systematic error it is not possible to determine the SCO profiles of this compound and the corresponding synthetic method. However, the reflectivity montages do depict that a spin crossover material was formed and a thermochromic transition of white → pink occurs upon cooling to temperatures below 298 K. Further analysis is required for this compound such as further investigation into the PXRD of **3-thin**, a repeat of the reflectivity measurements and acquiring magnetic measurements for accurate comparison. However, it is likely that from all of the evidence collated that each synthetic method synthesizes a form of $[Fe(atrz)_3](BF_4)_2$.

9. Conclusions & Future Prospects

The reflectivity analytical procedure was developed in order to quantify and characterize the thermochromism exhibited by the compounds investigated. Quantification is of particular importance as potential applications for these materials are optical sensors that are dependent on color change. Methods and parameters, as stated in **Section 2.4**, were successfully established to correct for camera's automatic white balance adjustments that occurs with thermochromism of the sample. This allowed for the formation and the SCO properties of a compound to be successfully monitored over time or temperature.

The synthesis of **1**, **2**, and **3** on *direct-contact* in the absence of force, solvent and heat was observed using optical microscopy, reflectivity, PXRD and Raman. The SCO properties of **1-direct** were generally similar to the traditional synthesis with minor differences in absolute temperature of transition, abruptness and hysteresis. **2-direct** formed a similar compound that consisted of the hydrated and dehydrated polymorphs of compound **2** but yielded similar SCO properties when compared to literature values of the respective compounds. The SCO properties of compound **3** could not be determined due to a systematic error, however vibrational spectroscopy suggests that the compound was likely the same as the traditional solution synthesis. Further analysis is needed to quantify and characterize the SCO properties of compound **3**. Additional investigation will provide a deeper understanding of the formation of different polymorphs of compounds synthesized via the *direct-contact* technique. This method shows a highly promising route to rapidly manufacture large quantities of SCO materials.

The readily reactive nature of these materials displayed by the *direct-contact* synthesis indicates that *in-situ* synthesis is possible. A new synthetic technique for the production of thin film triazole SCO materials has been developed via airbrush technology. This involves spraying a solution of iron salt followed by a solution of triazole to form an SCO material directly onto a substrate. The SCO properties of the thin films show generally similar transition and abruptness SCO properties with slightly narrower hysteresis to the compound formed by the traditional synthetic protocol. Further analysis such as repeated reflectivity and SQUID measurements is required to determine the SCO properties for **3-thin**. The thin films appear homogenous to the

naked eye however, observance of the films at a microscopic level reveals their inhomogeneous nature. Thus, this technique is likely not suitable for the production of high-quality thin films but could be useful for large-scale sensing that relies only on the visual output of the film.

The use of an airbrush to synthesize thin films is a rapid and economically beneficial technique. Already established technologies for airbrushing large surfaces makes it easily scalable. The ability to synthesize these thin films *in-situ* makes them highly versatile and applicable in many different scenarios. These advantages make them ideal for covering large surfaces and potentially surfaces that aren't uniform. It is also highly likely that this could be an ideal method of quick and easy stenciling of thin films. Future applications of large-scale thin films are large reaction vessels that could be sprayed to form an SCO compound with an appropriate $T_{1/2}$ that will optically demonstrate when a specific temperature has been exceeded. Other potential applications include spraying airplanes with SCO materials that switch with changes in pressure. This would be able to visually highlight any areas of an airplane that has incurred damage during a flight instantly and could possibly alleviate the requirement to manually inspect the entire plane.

Further investigation into the *thin-film* method would include SQUID analysis of the thin films to determine SCO properties in comparison to reflectivity measurements. Other analytical methods to provide additional understanding are TGA/DSC and Mossbauer spectroscopy. Further insight could be achieved by probing at the mechanics of the airbrush such as nozzle size, airflow, distance from substrate and examining the corresponding effects on the resultant thin film. It would also be interesting to extend the research beyond triazoles to see if the technique is applicable to all SCO complexes. The preliminary exploration of developing this technique reveals very promising initial results of a viable thin film synthetic method with an extremely encouraging future.

10. Appendix

10.1. Section 6

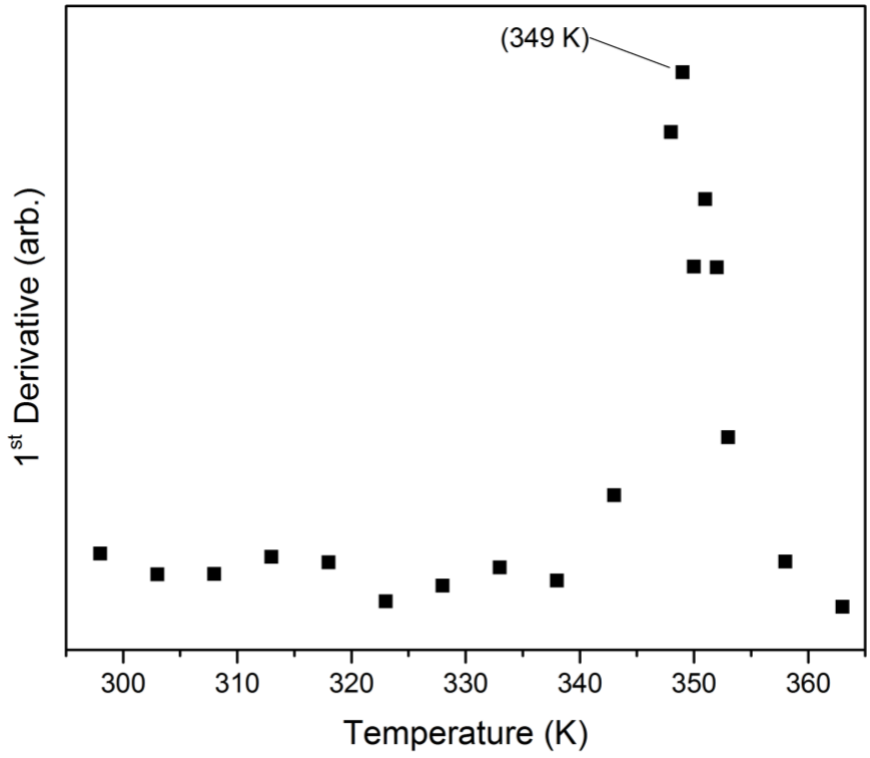

A.1: The first derivative calculating $T_{1/2}$ of the variable temperature Raman for **1-sol**.

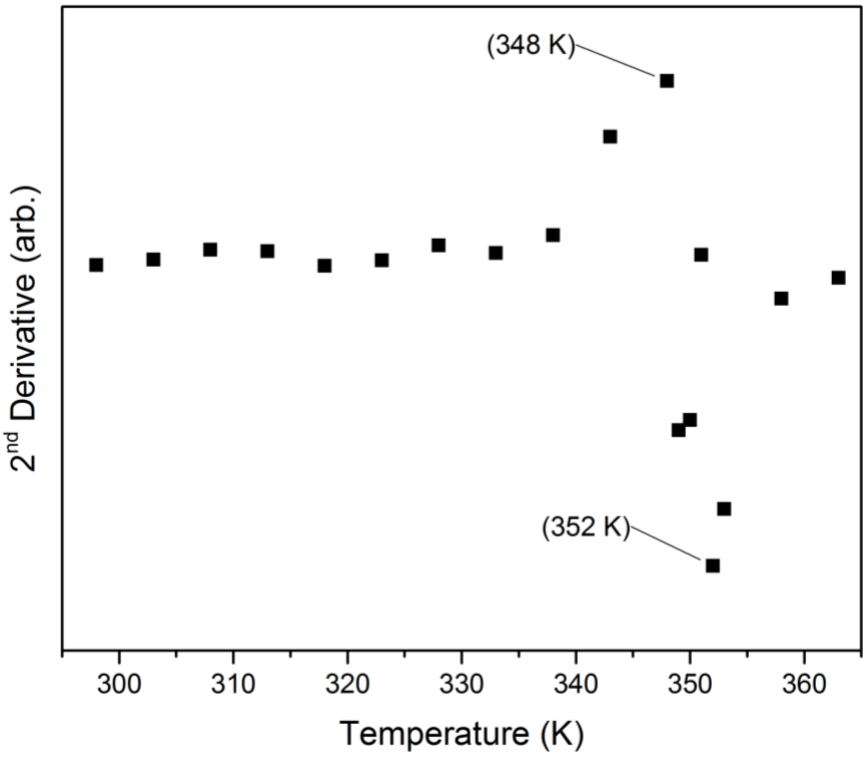

A.2: The second derivative for the variable temperature Raman used to calculate the smoothness of SCO transition for **1-sol**.

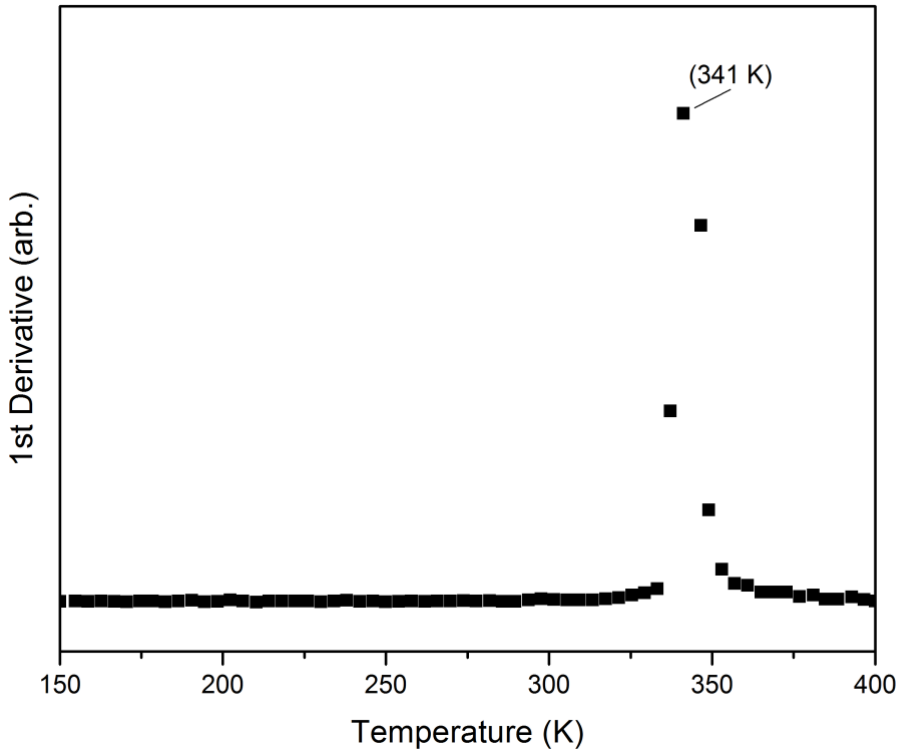

A.3: First derivative of the temperature dependent SQUID measurements to determine $T_{1/2}$ of the heating cycle for **1-sol**.

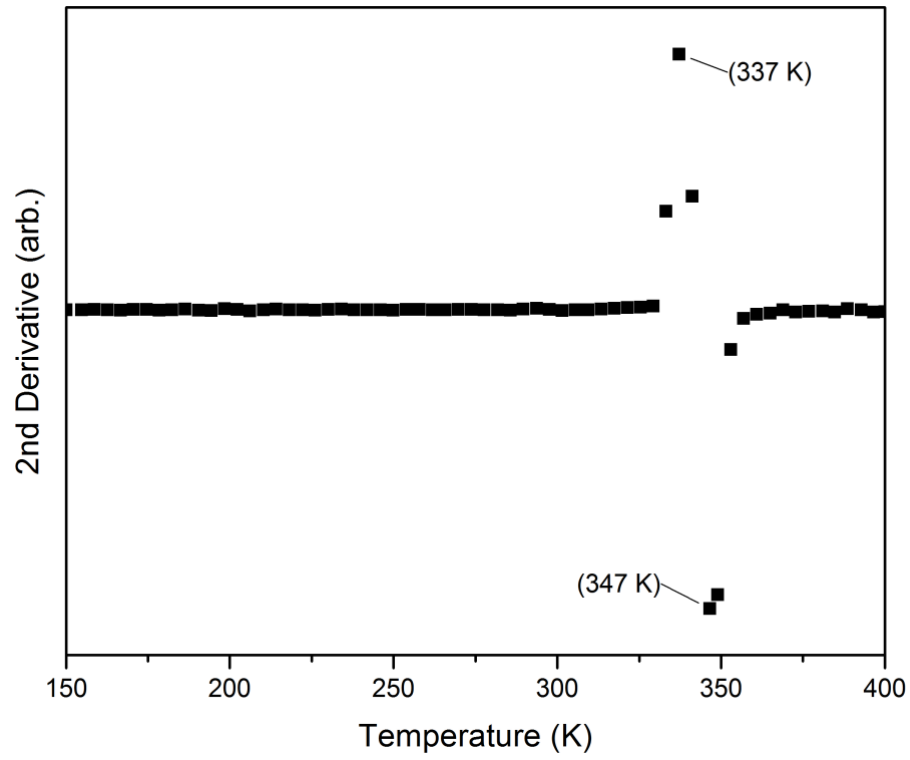

A.4: Second derivative of the temperature dependent SQUID measurements to determine smoothness of SCO transition of the heating cycle for **1-sol**.

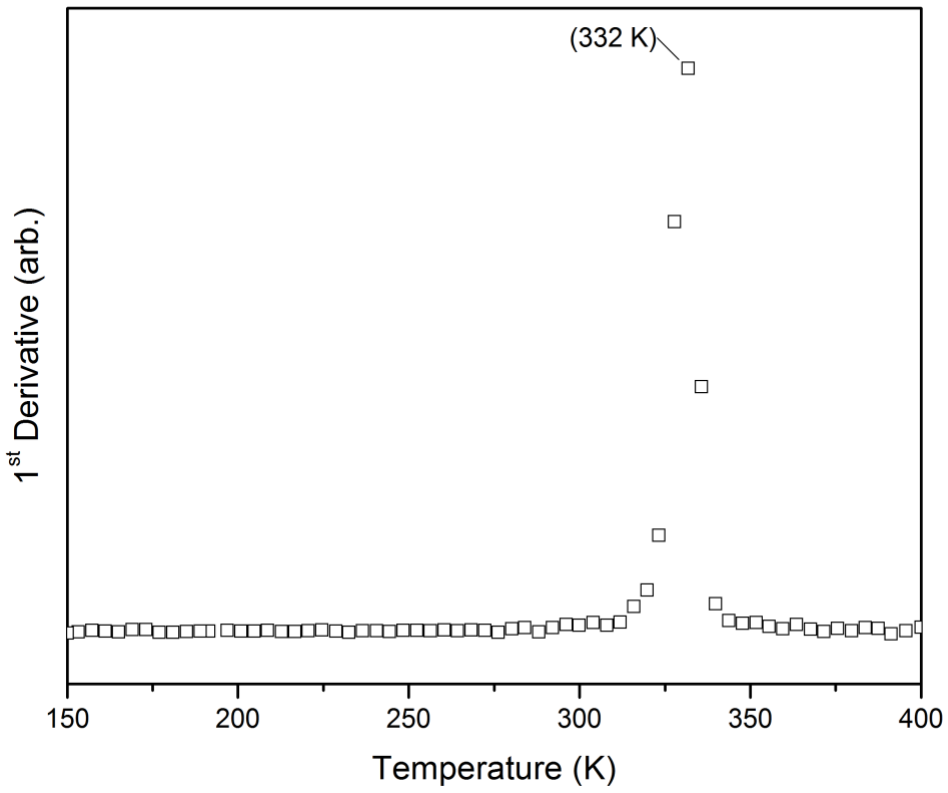

A 5: First derivative of the temperature dependent SQUID measurements to determine $T_{1/2}$ of the cooling cycle for **1-sol**.

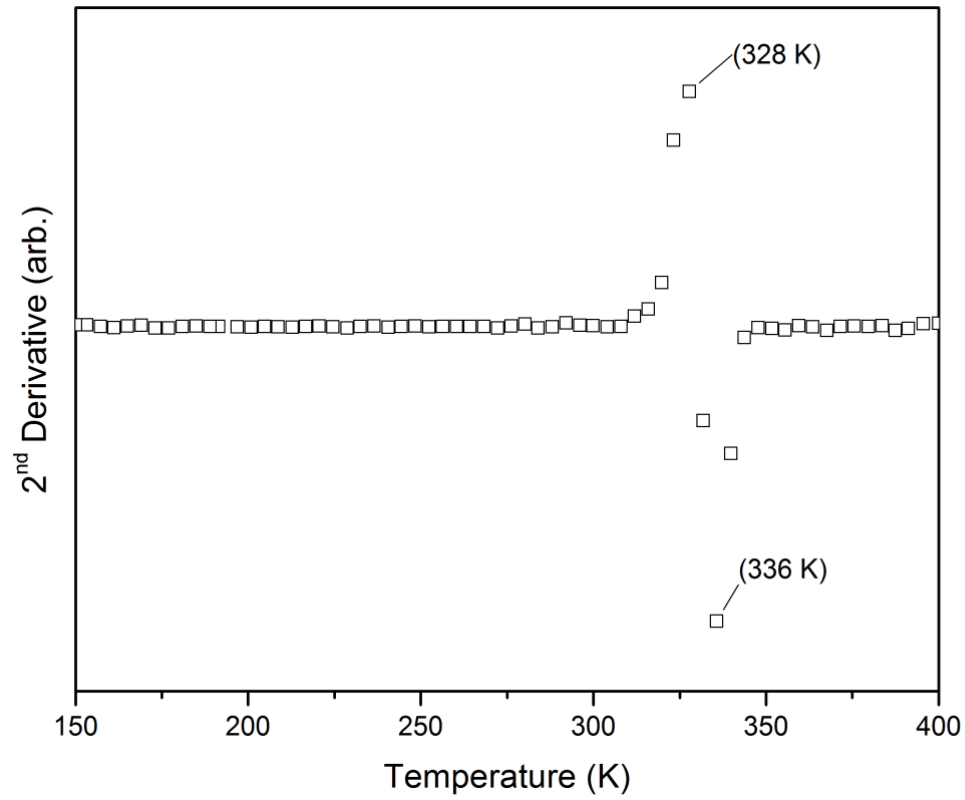

A.6: Second derivative of the temperature dependent SQUID measurements to determine smoothness of SCO transition of the cooling cycle for **1-sol**.

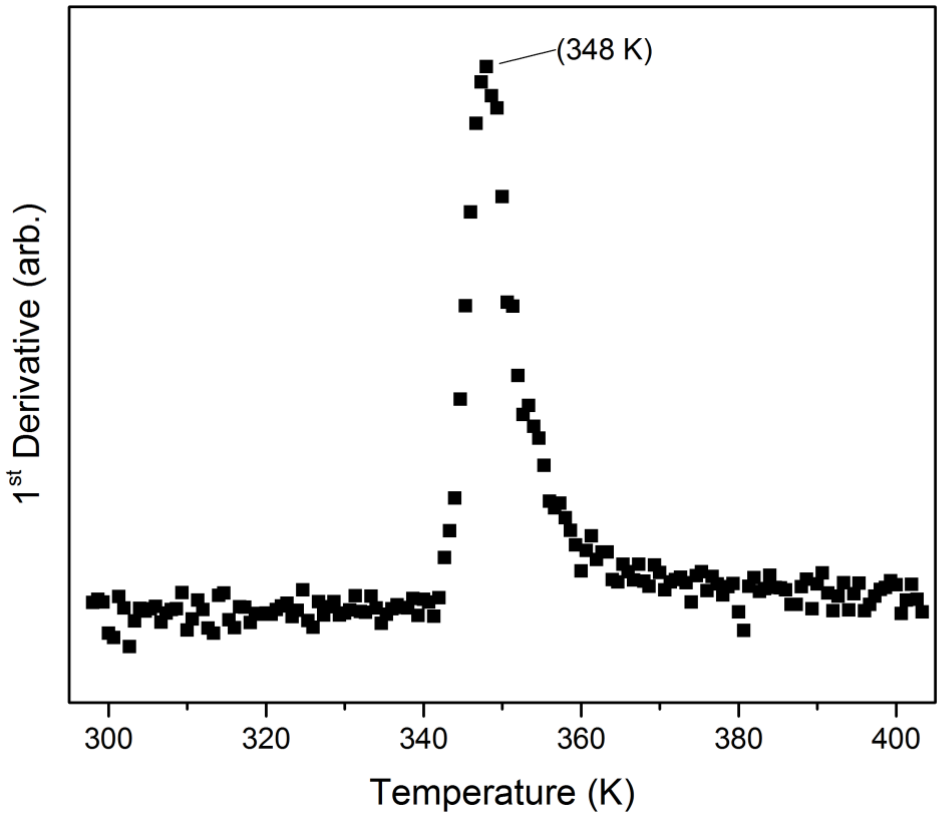

A.7*:* First derivative of the reflectivity measurements to determine $T_{1/2}$ of the heating cycle for **1-sol**.

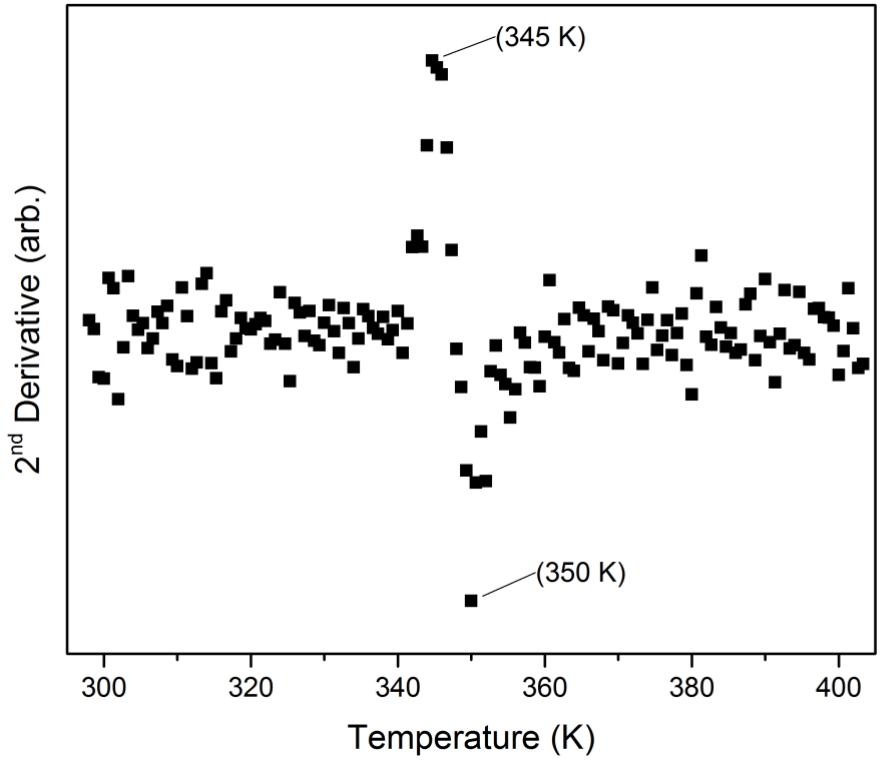

A.8: Second derivative of the reflectivity measurements to determine smoothness of SCO transition of the heating cycle for **1-sol**.

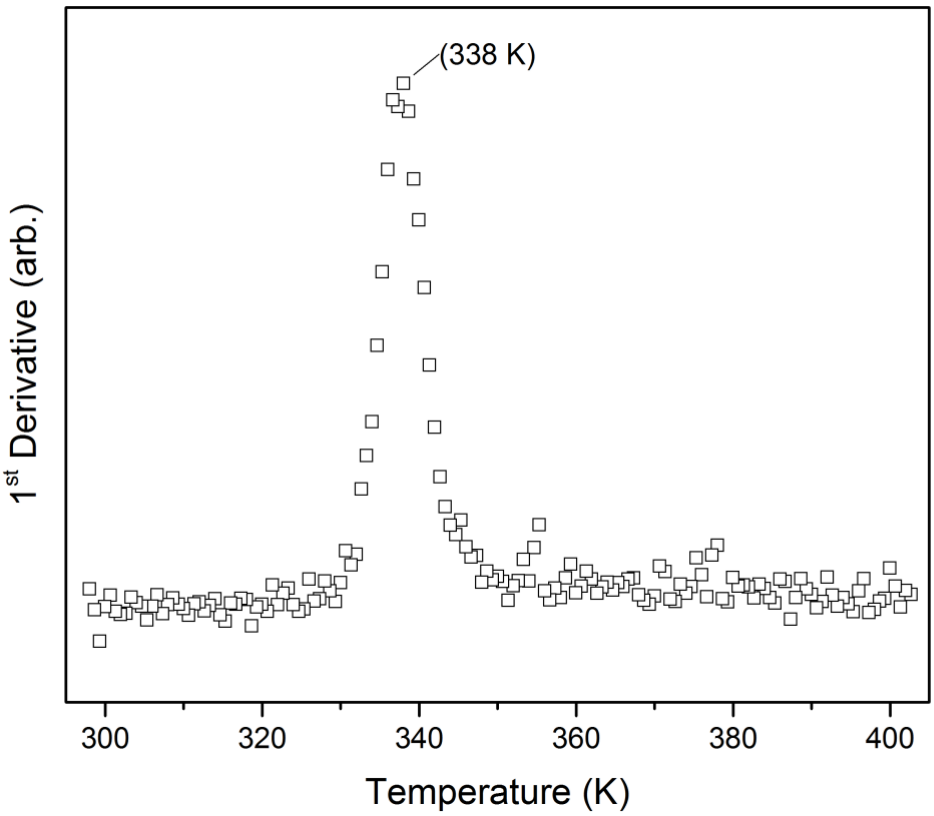

A.9: First derivative of the reflectivity measurements to determine $T_{1/2}$ of the cooling cycle for **1-sol**.

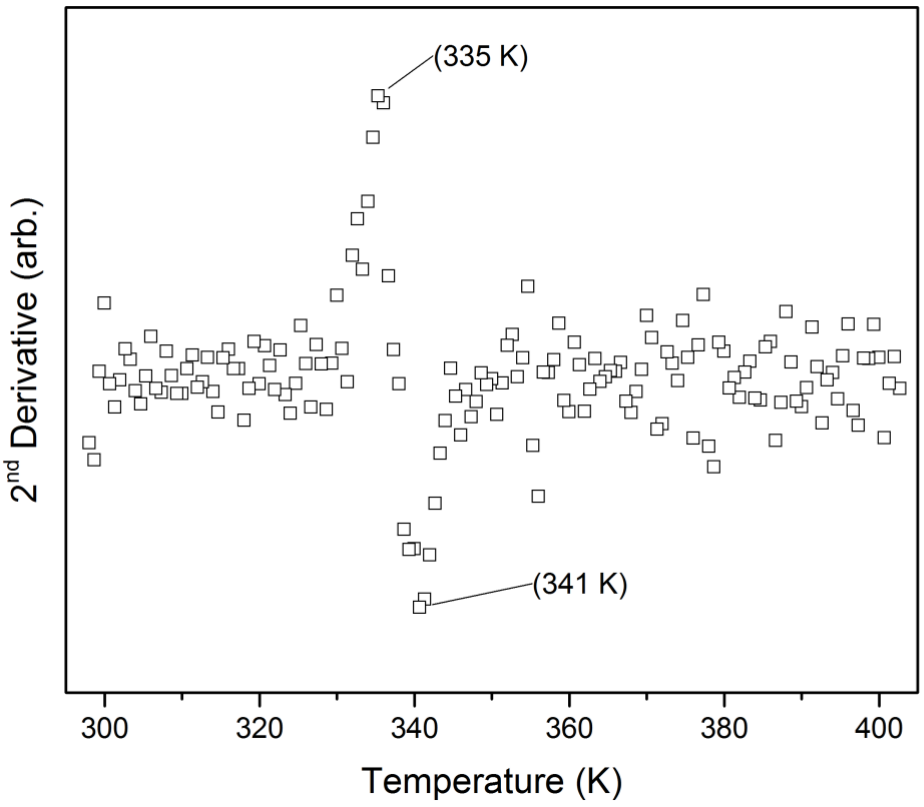

A.10: Second derivative of the reflectivity measurements to determine the smoothness of the transition of the cooling cycle for **1-sol**.

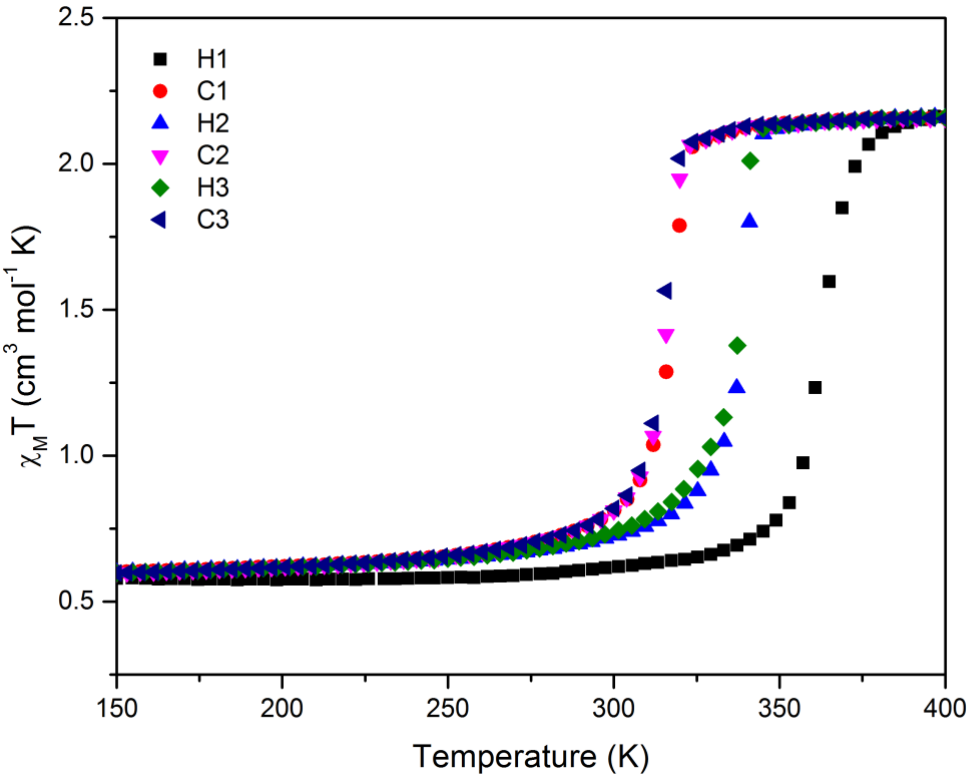

A.11: Variable temperature SQUID measurements including the first heating cycle of **1-direct**.

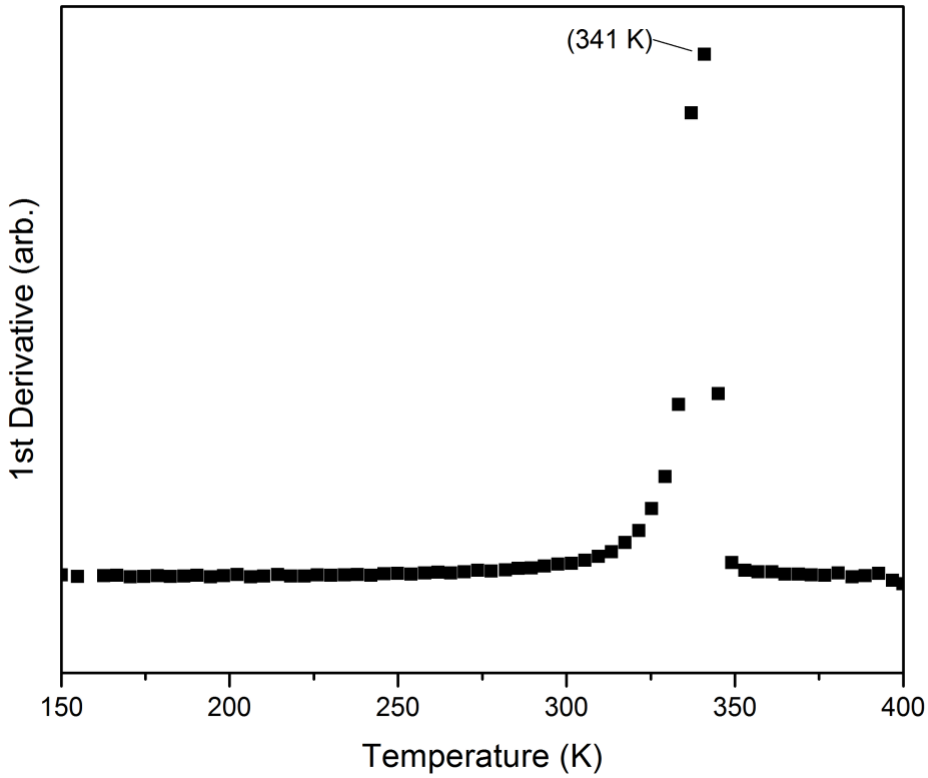

A.12: The first derivative for the variable temperature Raman used to calculate the smoothness of SCO transition for **1-direct**.

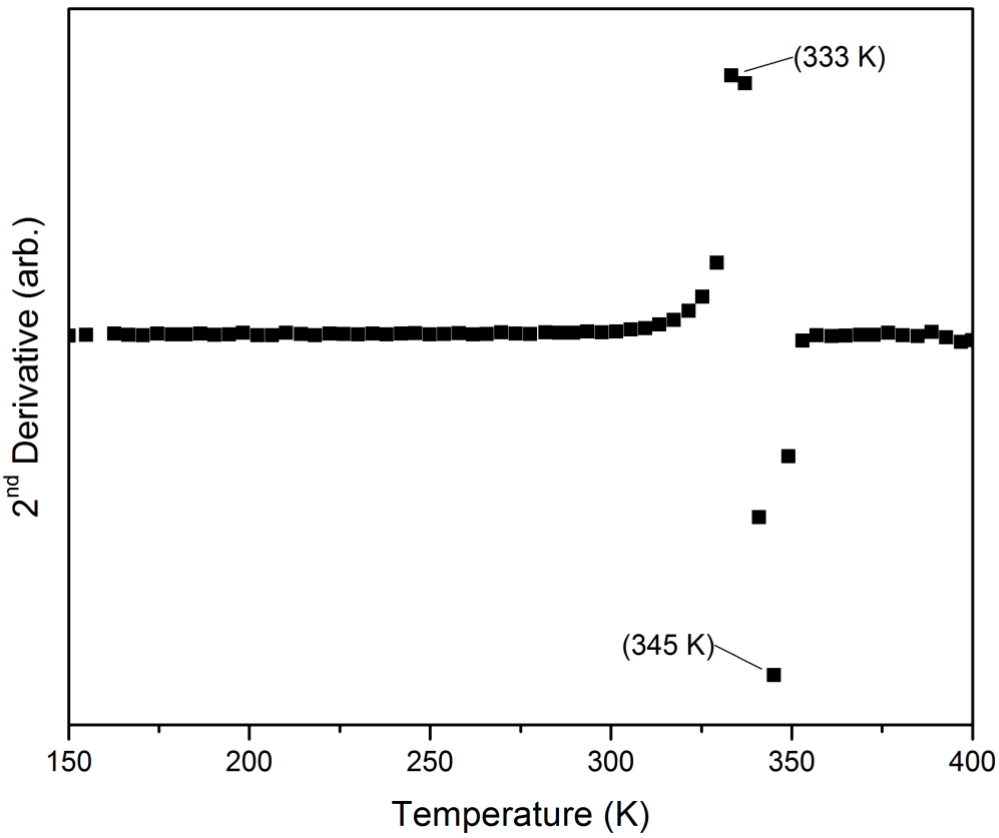

A.13: Second derivative of the temperature dependent SQUID measurements to determine smoothness of SCO transition of the cooling cycle for **1-direct.**

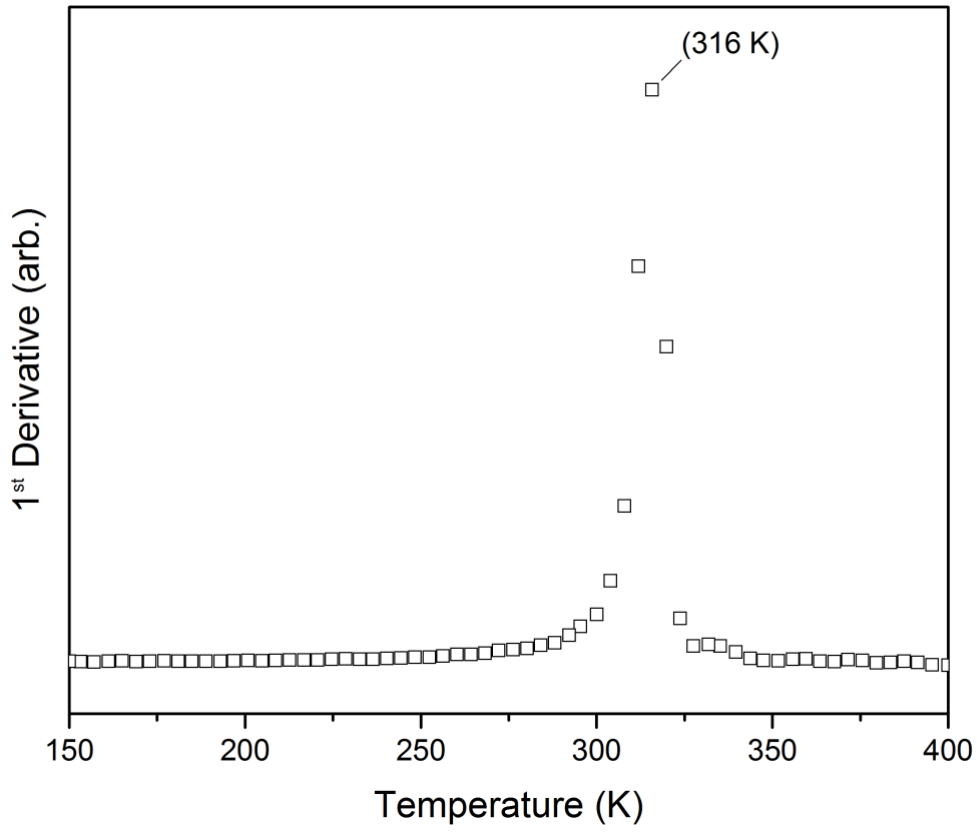

A.14: First derivative of the temperature dependent SQUID measurements to determine $T_{1/2}$ of the cooling cycle for **1-direct**.

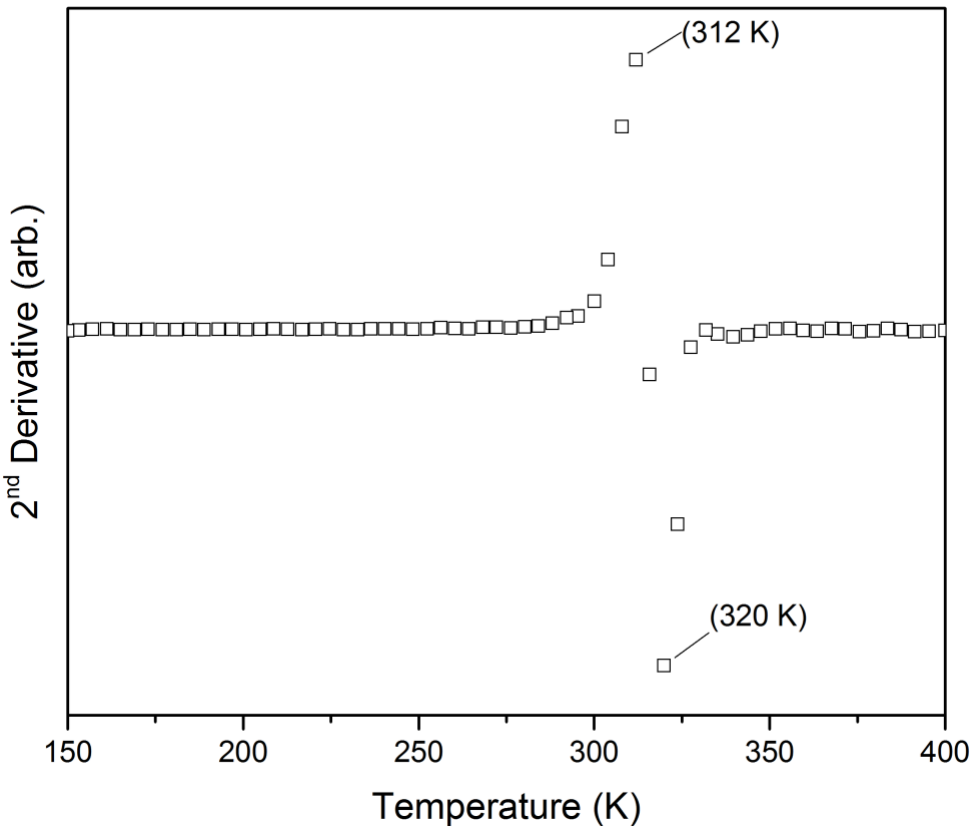

A.15: Second derivative of the temperature dependent SQUID measurements to determine smoothness of SCO transition of the cooling cycle for **1-direct**.

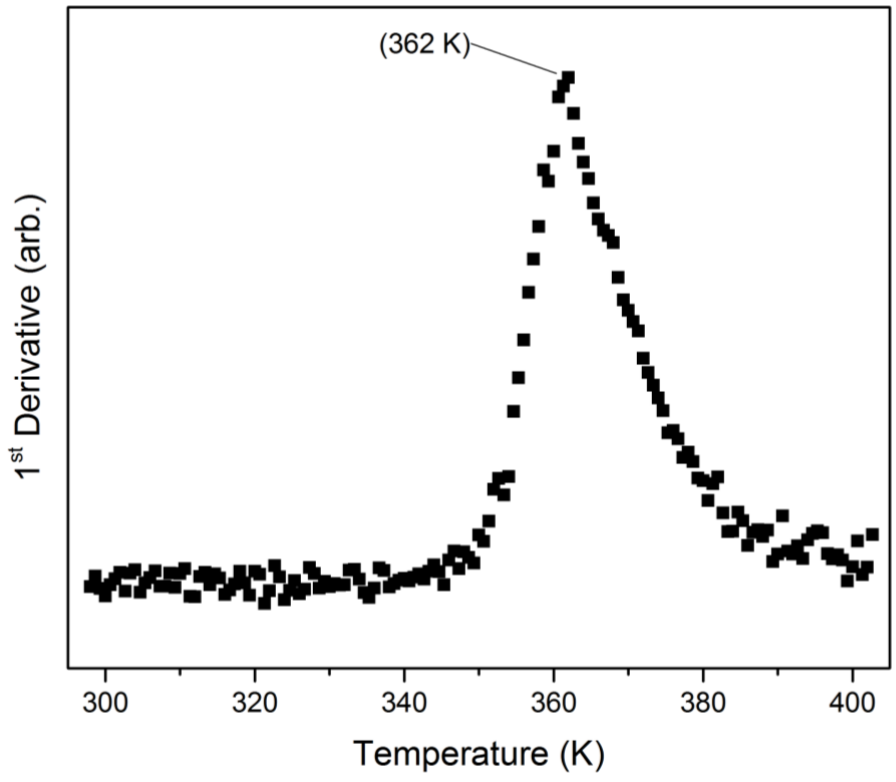

A.16: First derivative of the reflectivity measurements to determine $T_{1/2}$ of the heating cycle for **1-direct**.

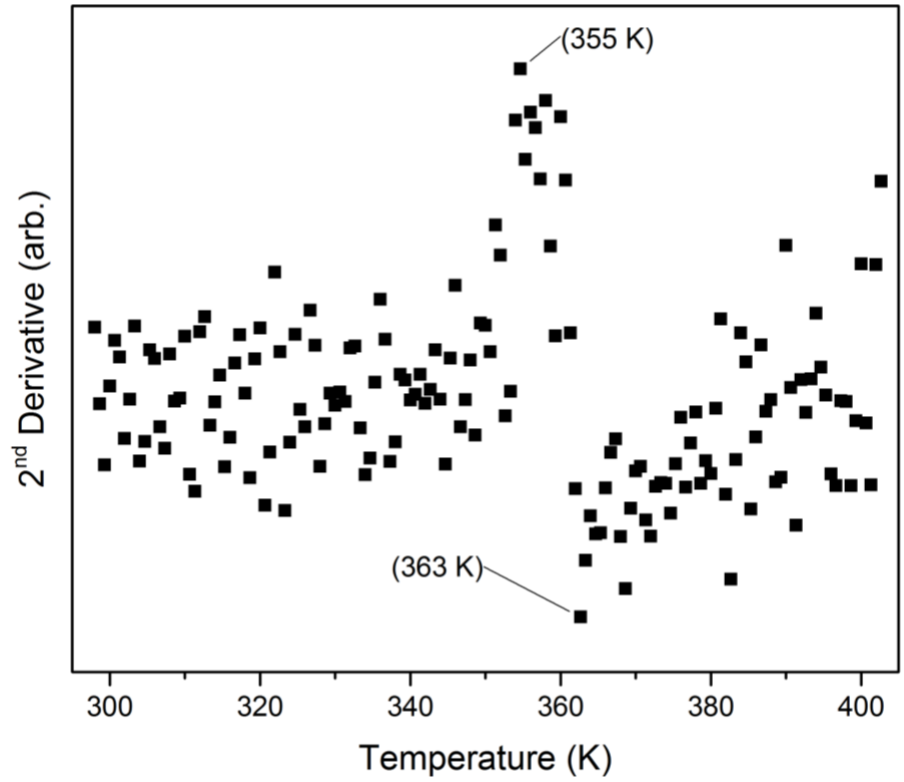

A.17: Second derivative of the reflectivity measurements to determine the smoothness of the transition of the heating cycle for **1-direct**.

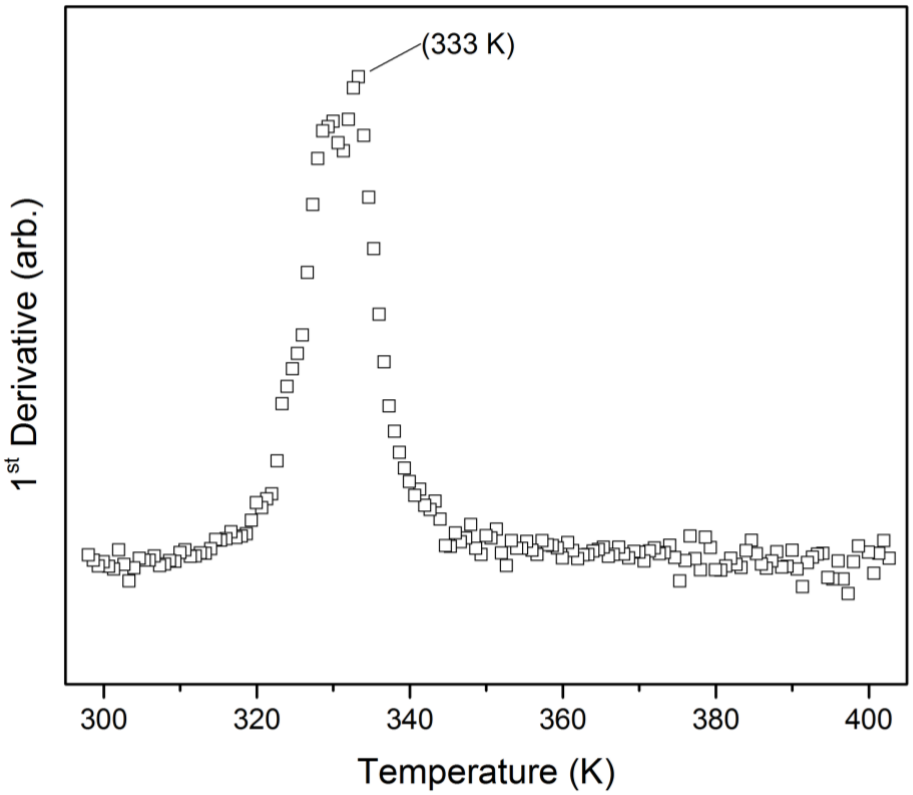

A.18: First derivative of the reflectivity measurements to determine $T_{1/2}$ of the cooling cycle for **1-direct**.

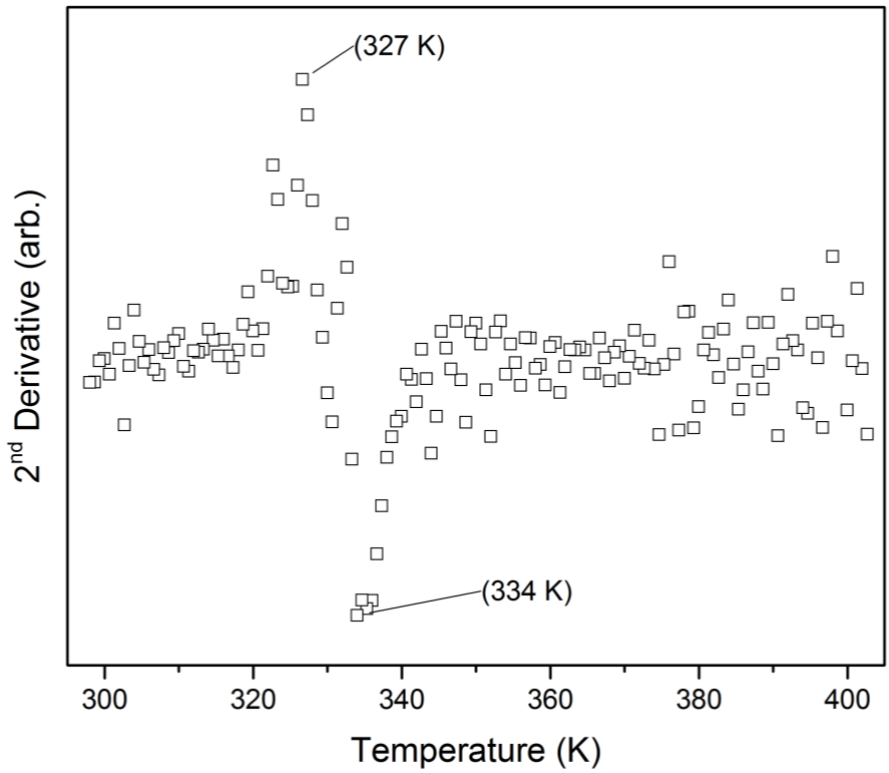

A.19: Second derivative of the reflectivity measurements to determine the smoothness of the transition of the cooling cycle for **1-direct**.

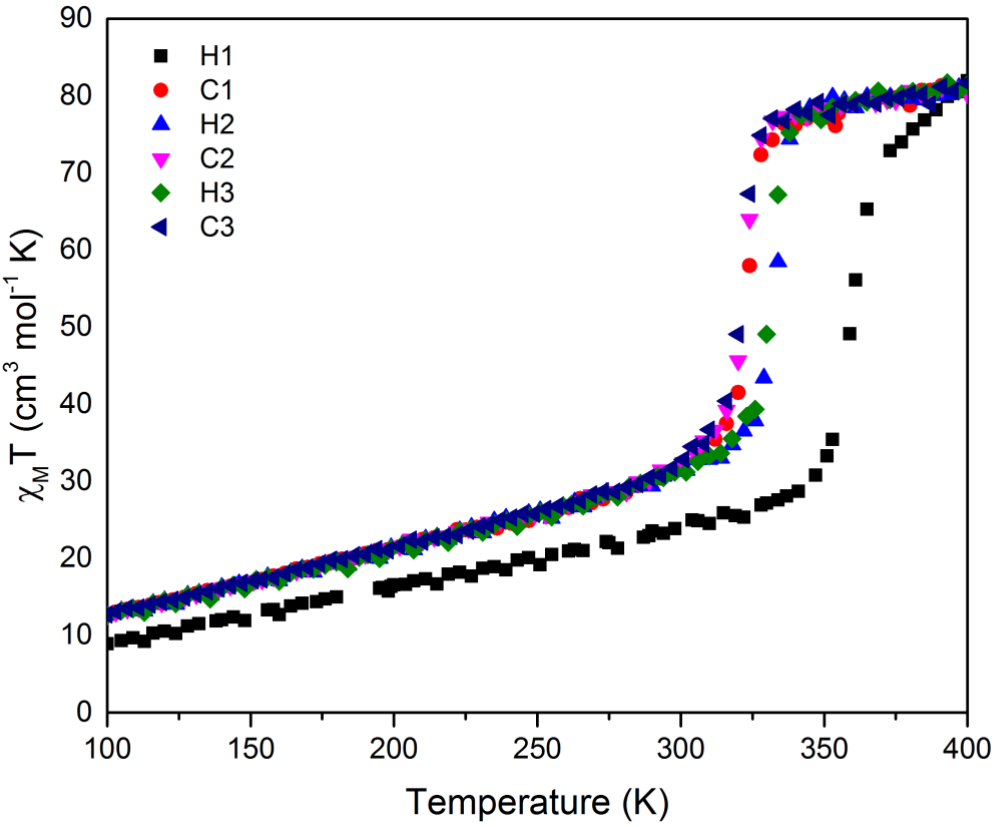

A:20: Variable temperature SQUID measurements including the first heating cycle of **1-thin**.

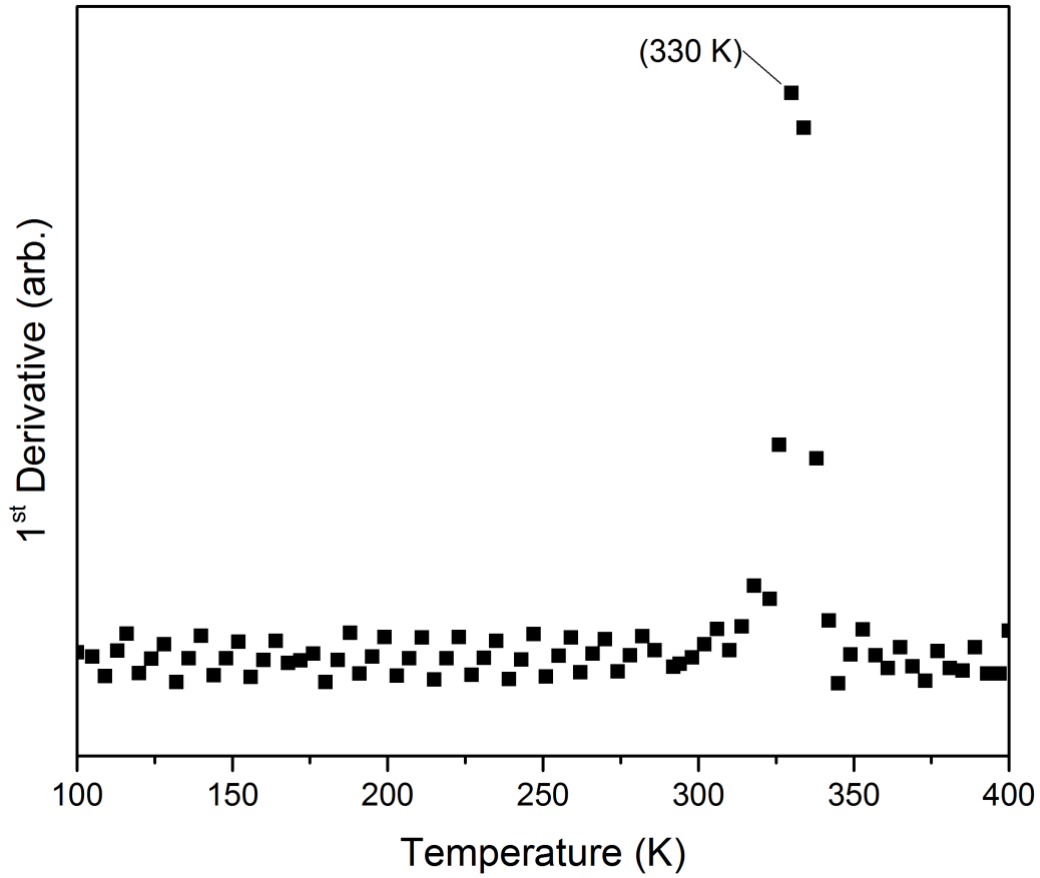

A.21: First derivative of the temperature dependent SQUID measurements to determine $T_{1/2}$ of the heating cycle for **1-thin**.

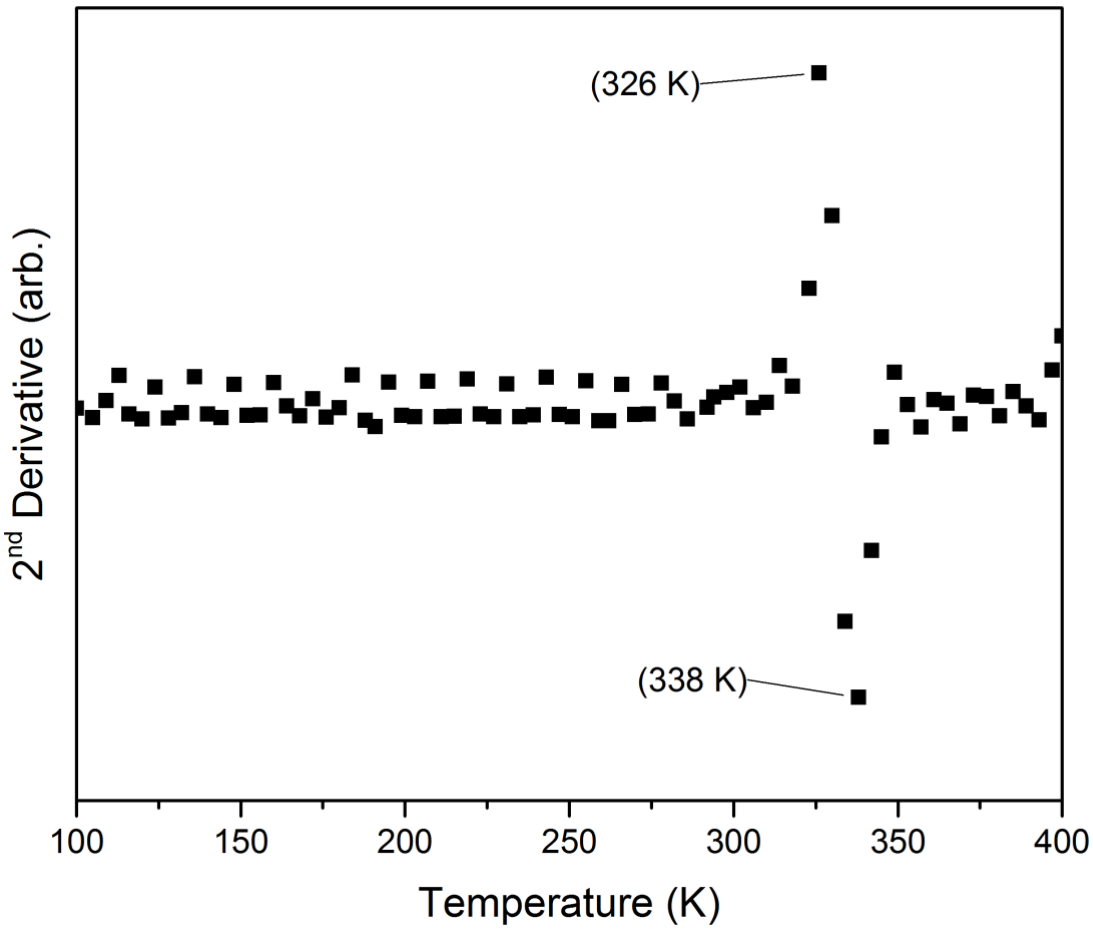

A.22: Second derivative of the temperature dependent SQUID measurements to determine smoothness of SCO transition of the heating cycle for **1-thin.**

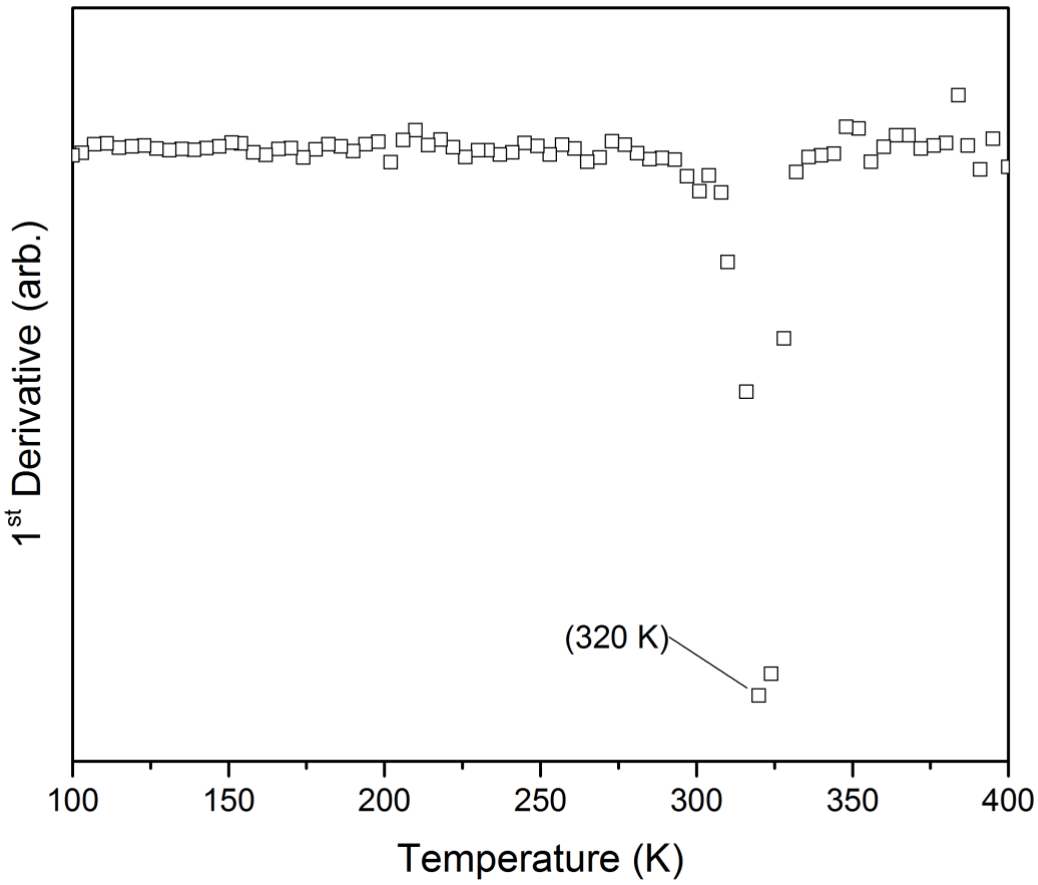

A.23: First derivative of the temperature dependent SQUID measurements to determine $T_{1/2}$ of the cooling cycle for **1-thin**.

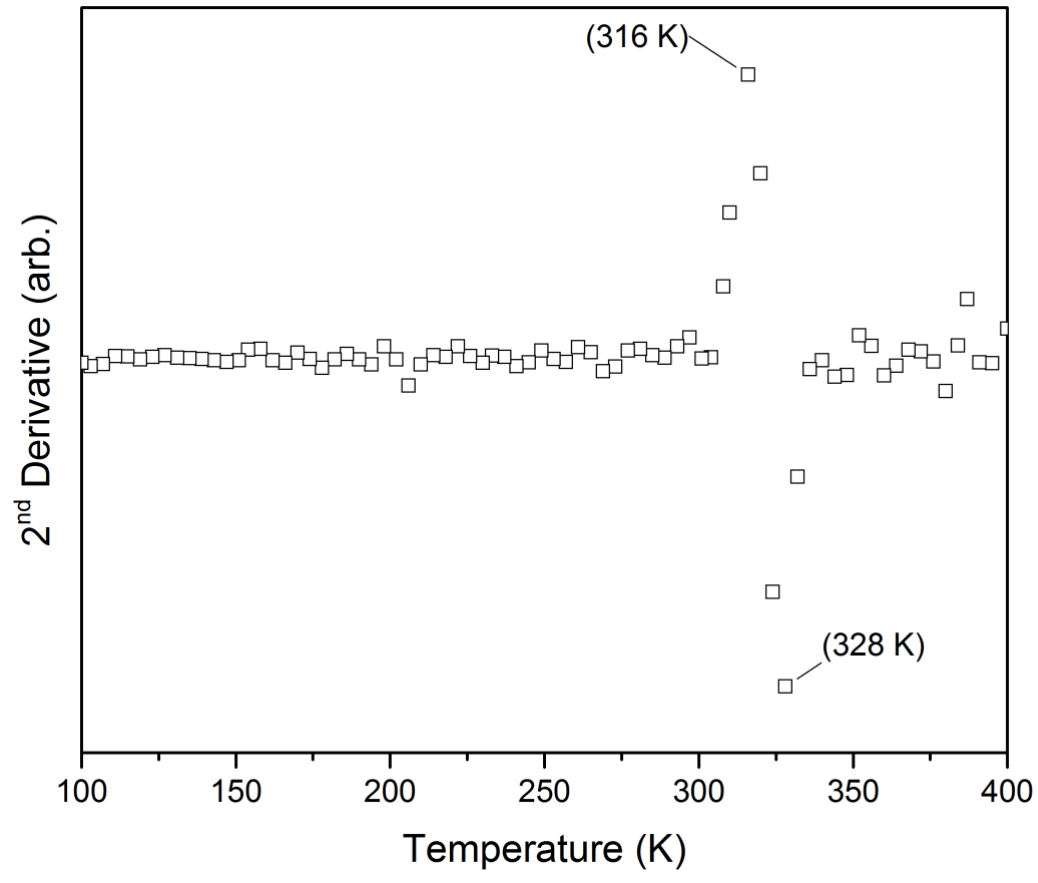

A.24: Second derivative of the temperature dependent SQUID measurements to determine smoothness of SCO transition of the cooling cycle for **1-thin.**

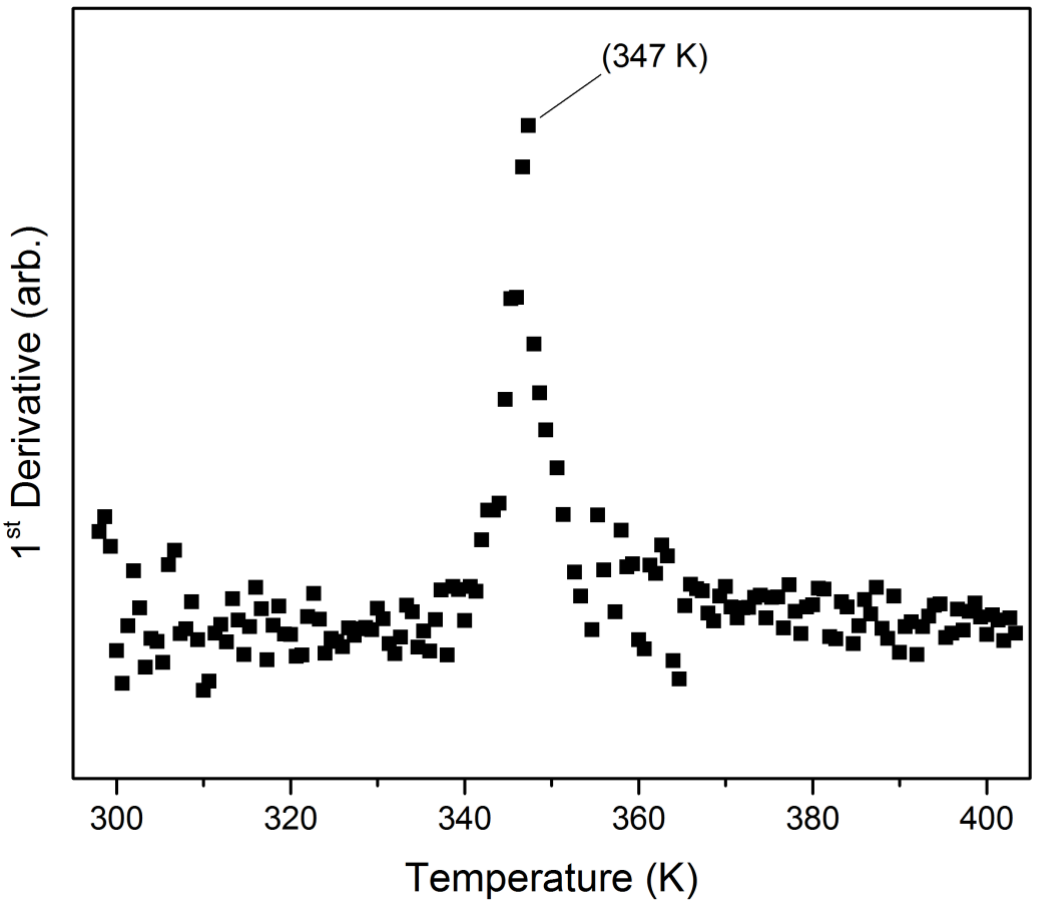

A.25: First derivative of the reflectivity measurements to determine $T_{1/2}$ of the heating cycle for **1-thin**.

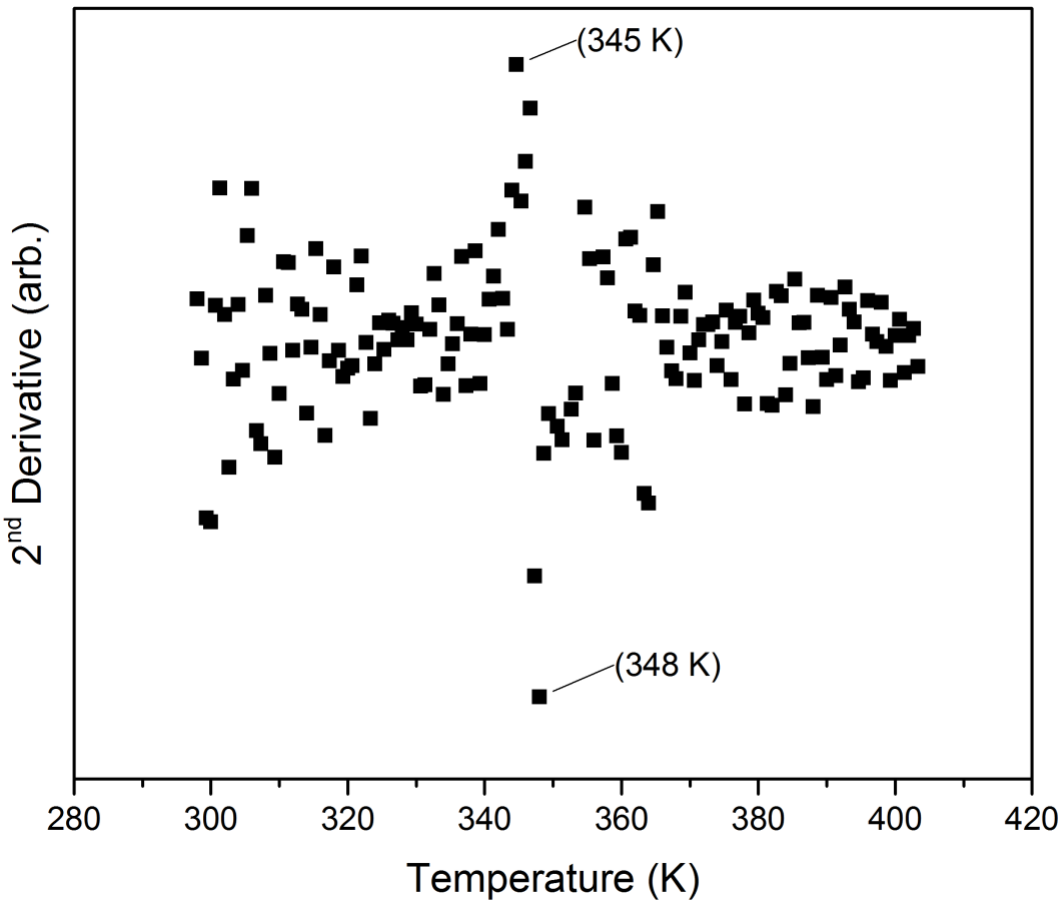

A.26: Second derivative of the reflectivity measurements to determine the smoothness of the transition of the heating cycle for **1-thin**.

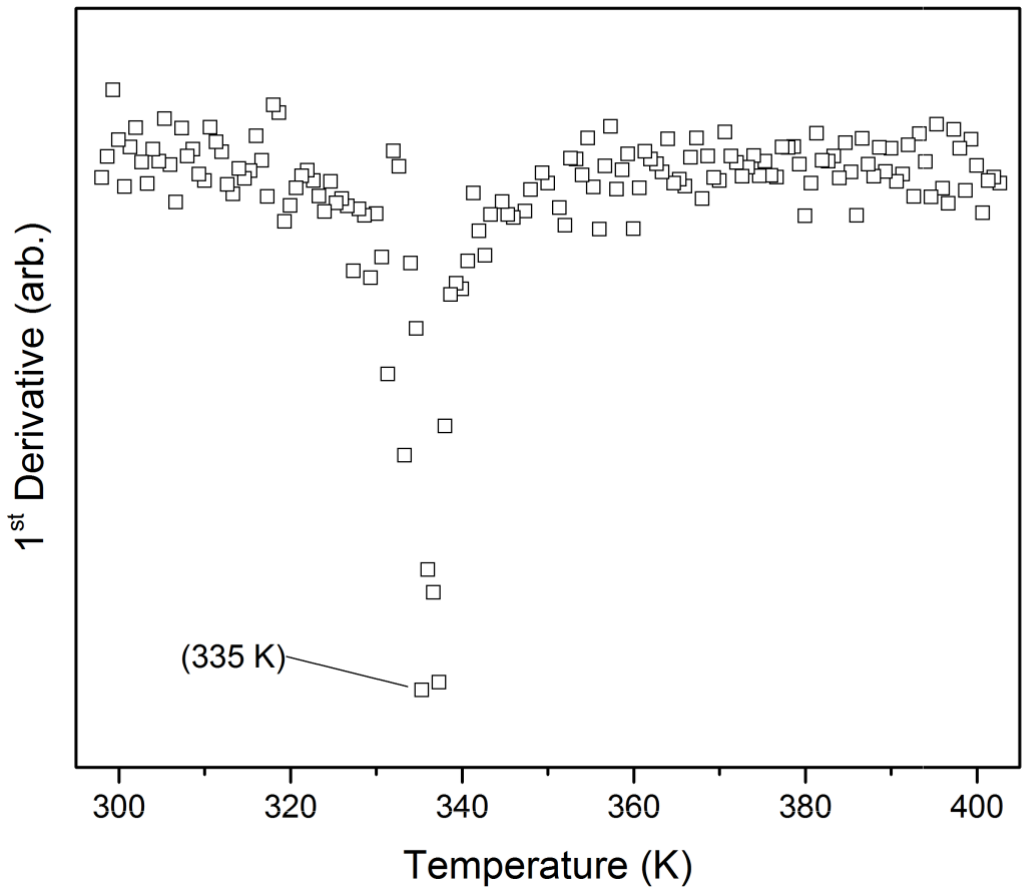

A 27: First derivative of the reflectivity measurements to determine $T_{1/2}$ of the cooling cycle for **1-thin**.

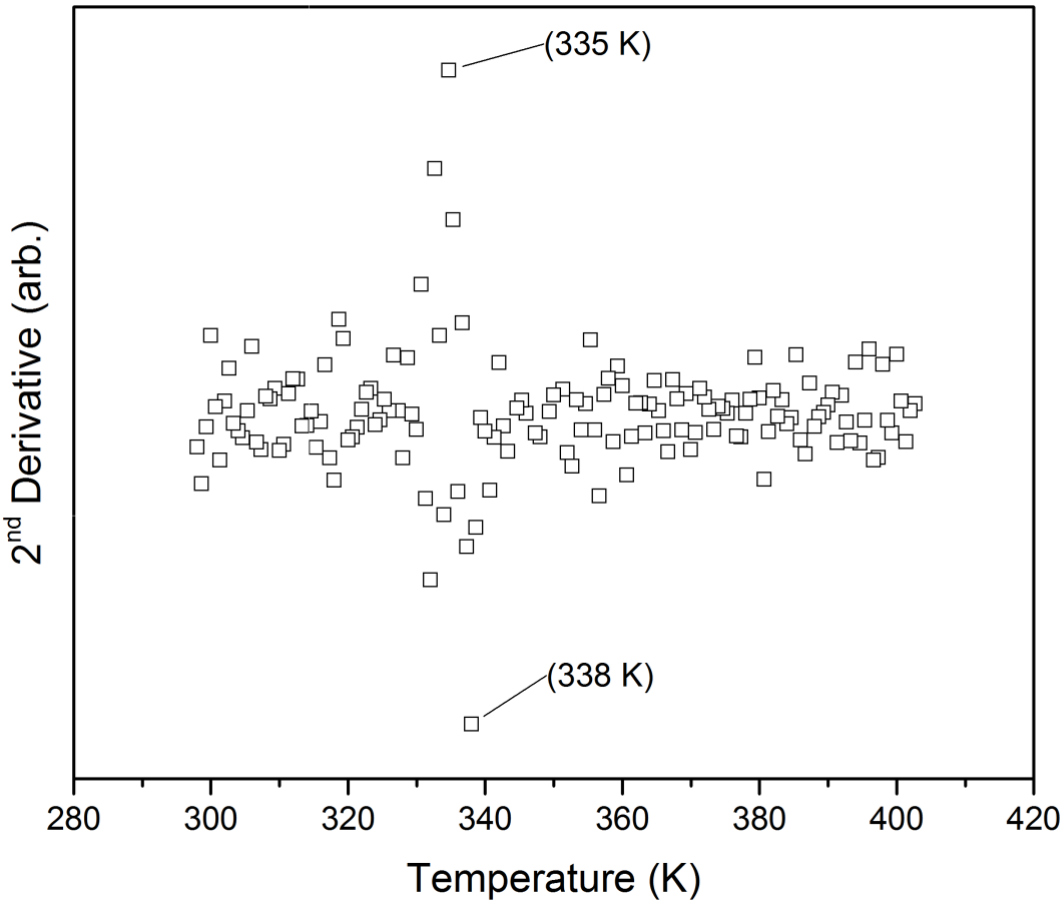

A.28: Second derivative of the reflectivity measurements to determine the smoothness of the transition of the heating cycle for **1-thin**.

10.2. Section 7

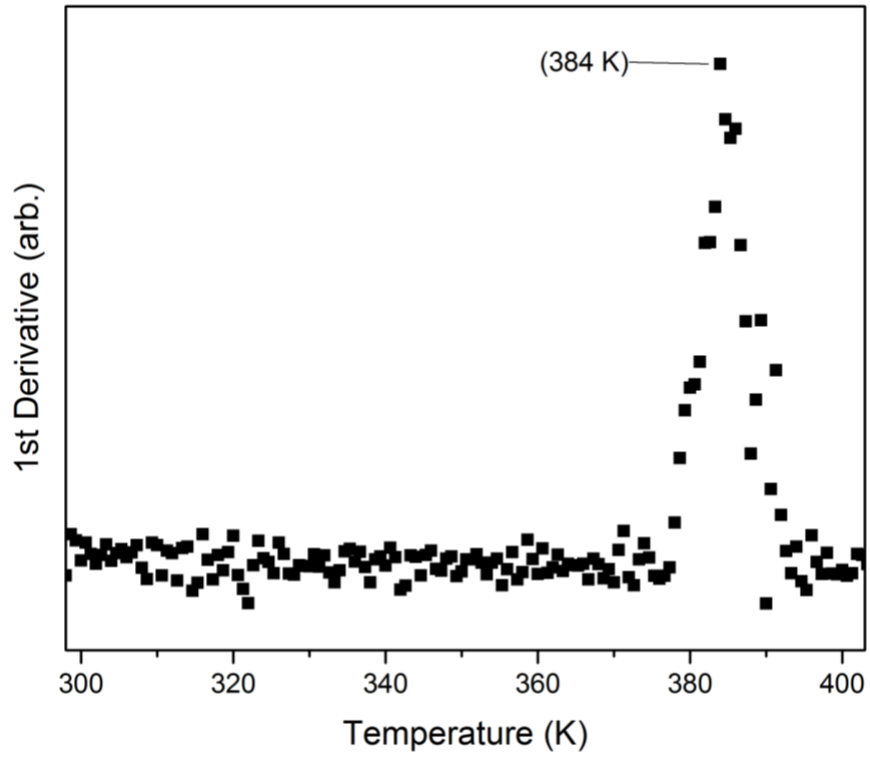

A.29: First derivative of the reflectivity measurements to determine $T_{1/2}$ of the heating cycle for **2-sol**.

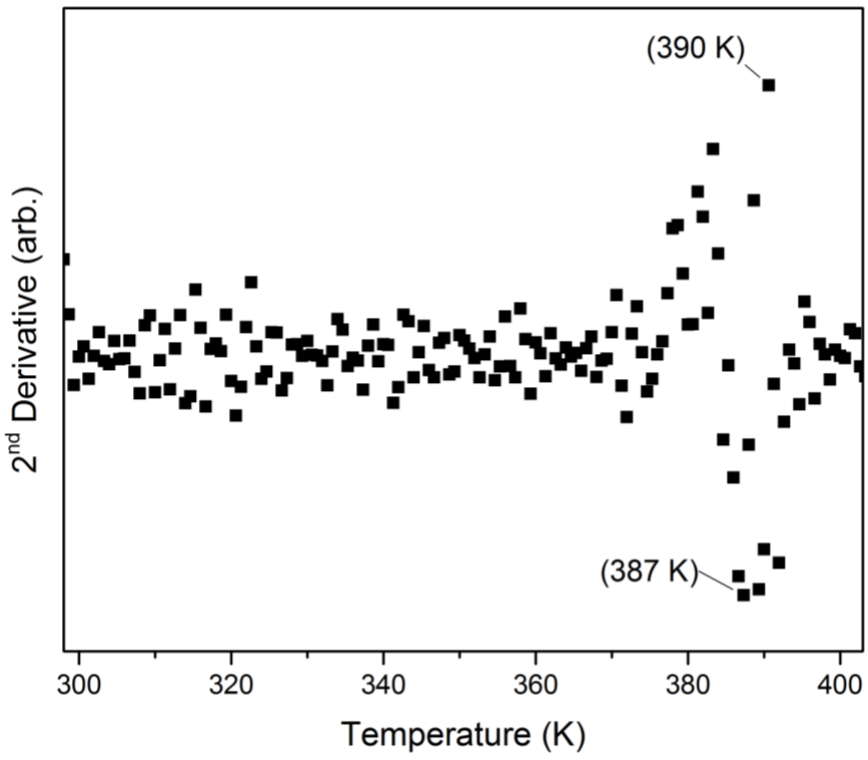

A.30: Second derivative of the reflectivity measurements to determine the smoothness of the transition of the heating cycle for **2-sol**.

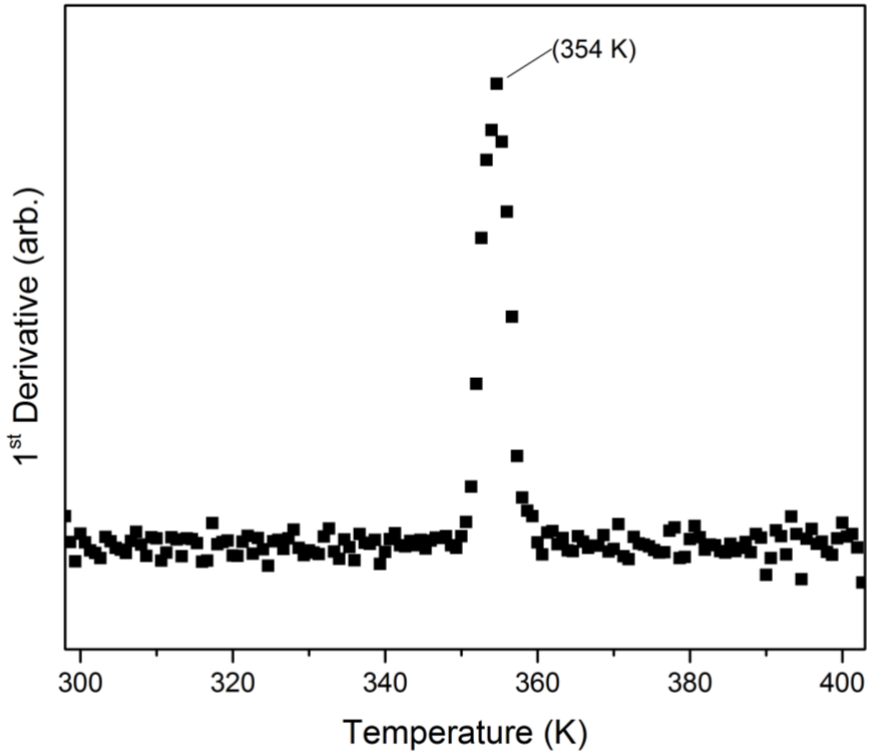

A.31: First derivative of the reflectivity measurements to determine $T_{1/2}$ of the cooling cycle for **2-sol**.

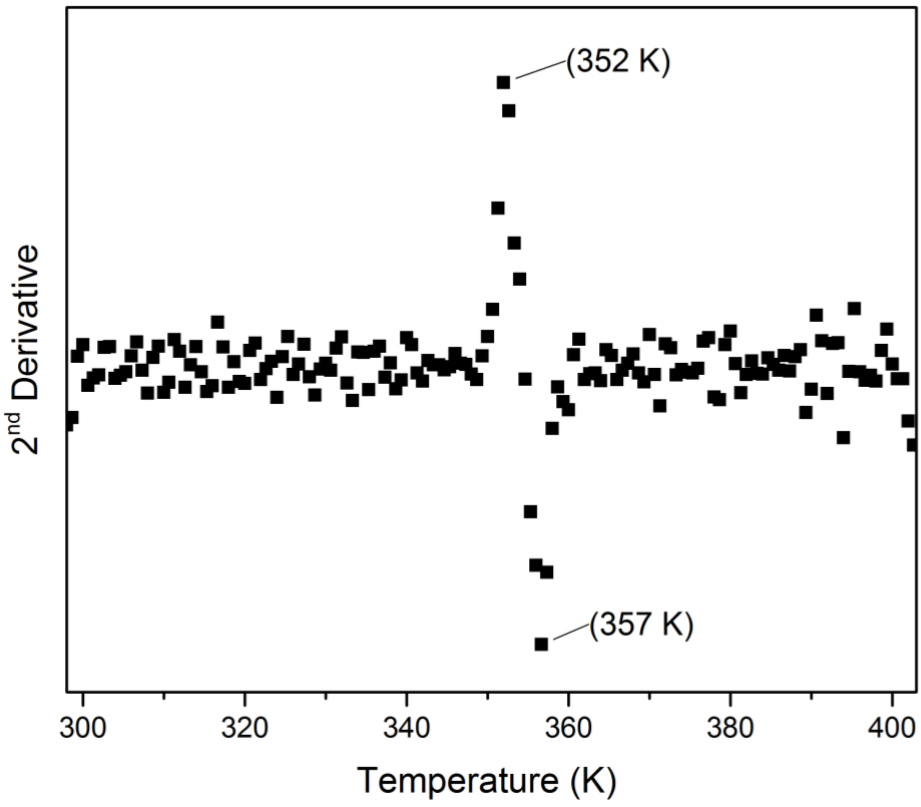

A.32: Second derivative of the reflectivity measurements to determine the smoothness of the transition of the heating cycle for **2-sol**.

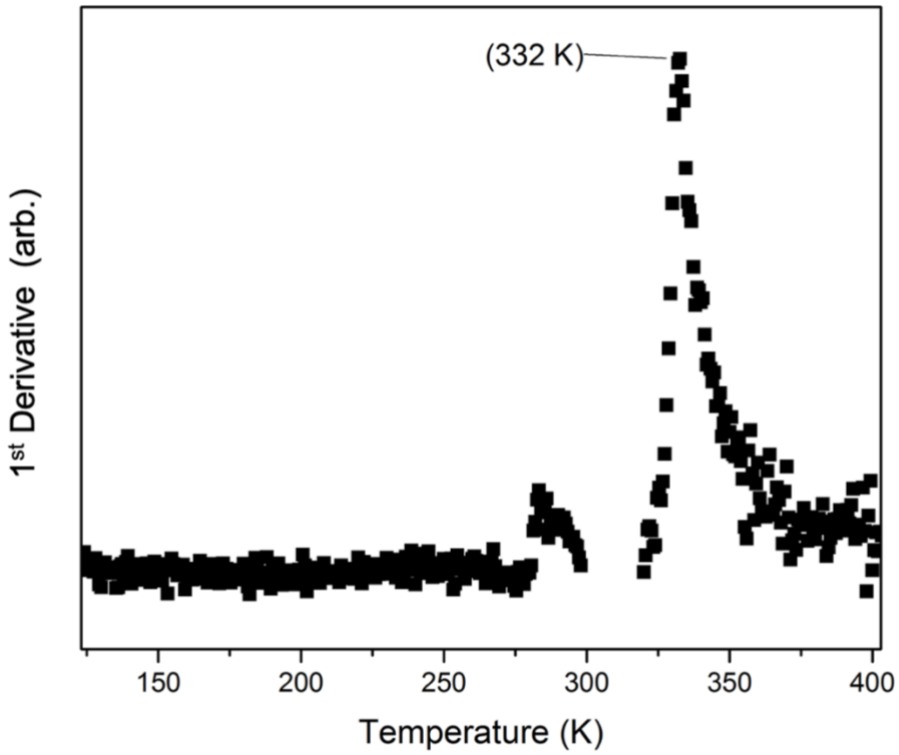

A.33: First derivative of the reflectivity measurements to determine $T_{1/2}$ of the heating cycle for **2-direct**.

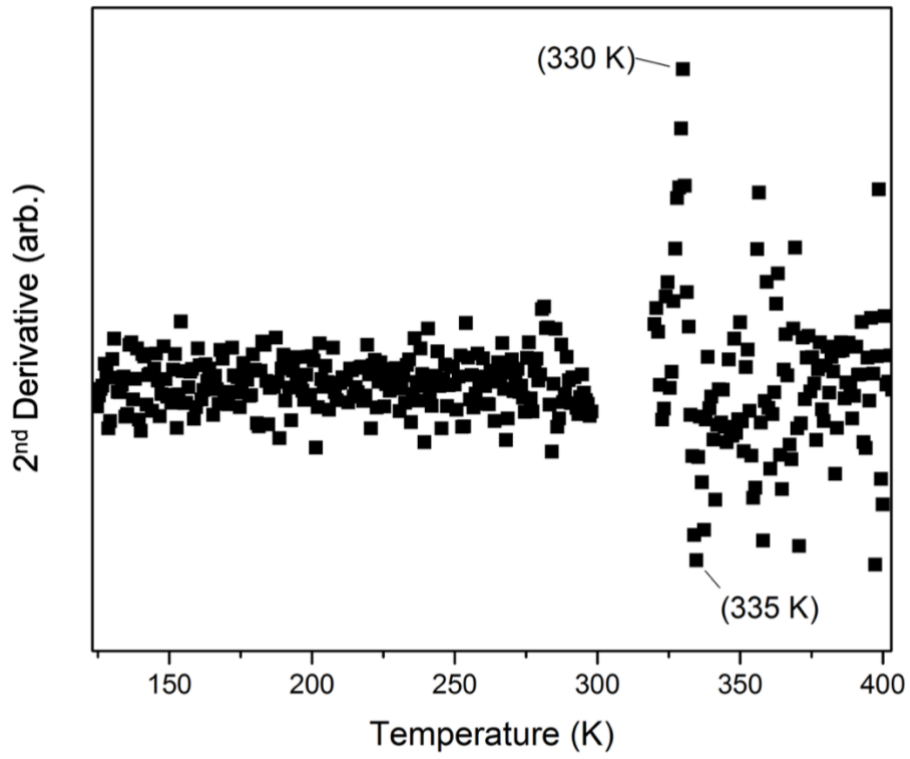

A.34: Second derivative of the reflectivity measurements to determine the smoothness of the transition of the heating cycle for **2-direct**.

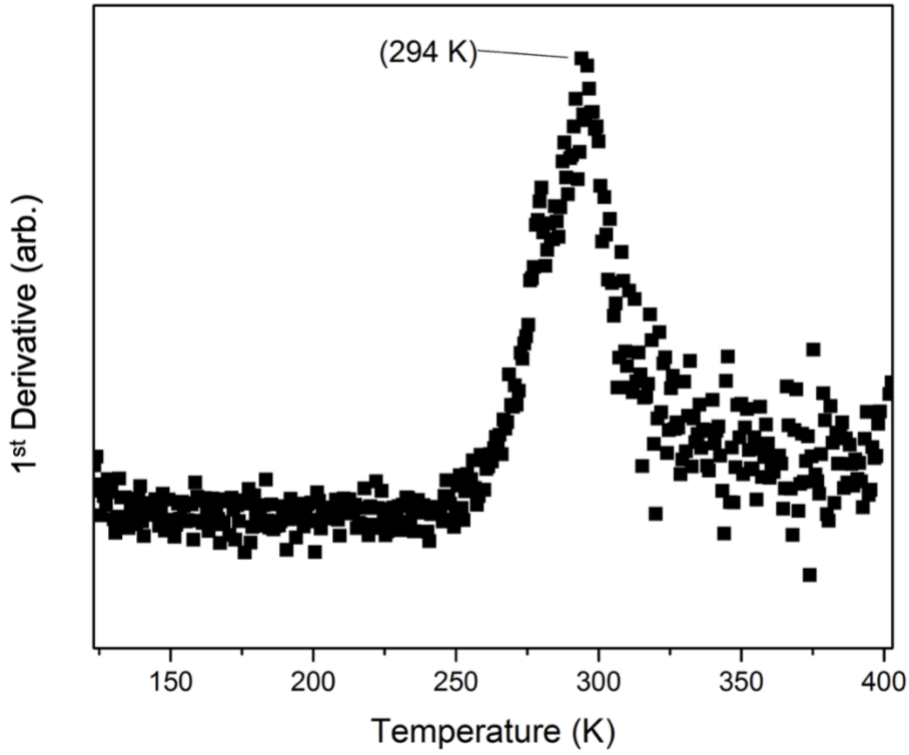

A.35: First derivative of the reflectivity measurements to determine $T_{1/2}$ of the cooling cycle for **2-direct**.

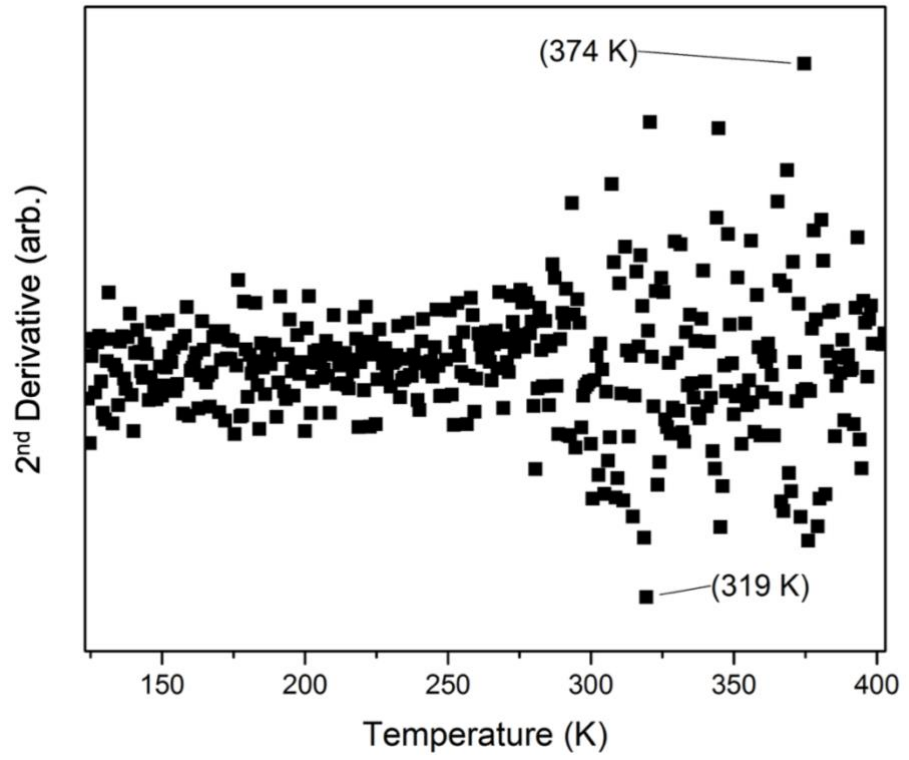

A.36: Second derivative of the reflectivity measurements to determine the smoothness of the transition of the heating cycle for **2-sol**.

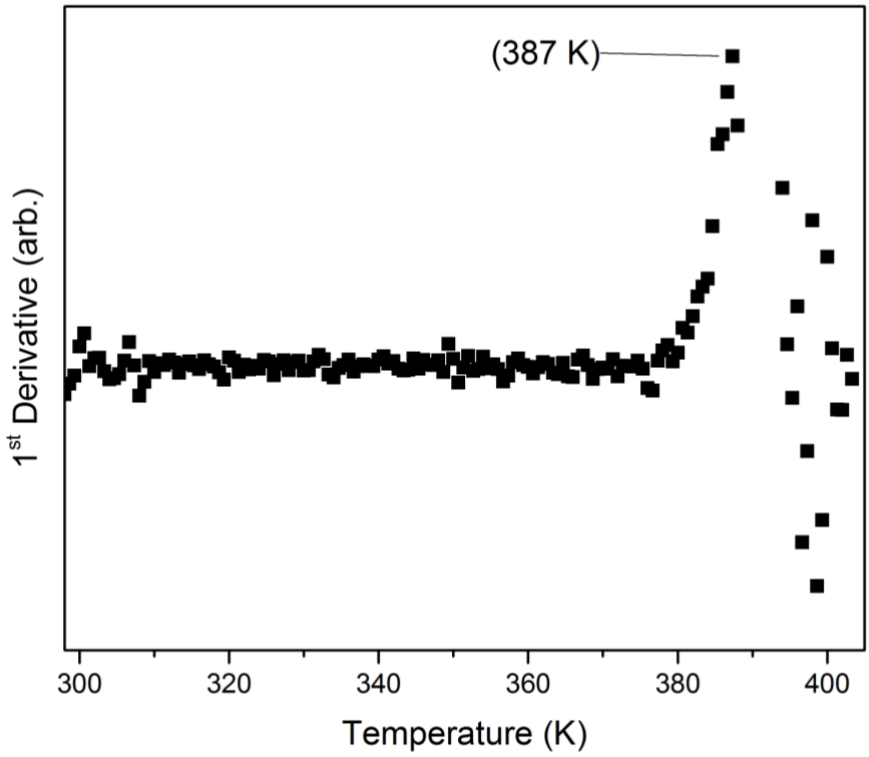

A.37: First derivative of the reflectivity measurements to determine $T_{1/2}$ of the heating cycle for **2-thin**.

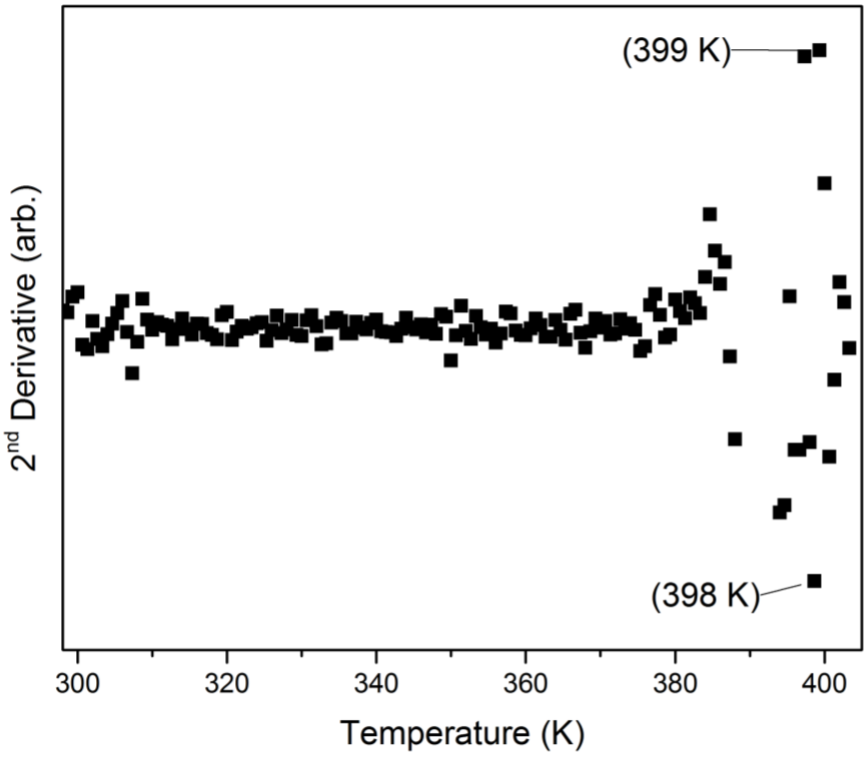

A.38: Second derivative of the reflectivity measurements to determine the smoothness of the transition of the heating cycle for **2-thin**.

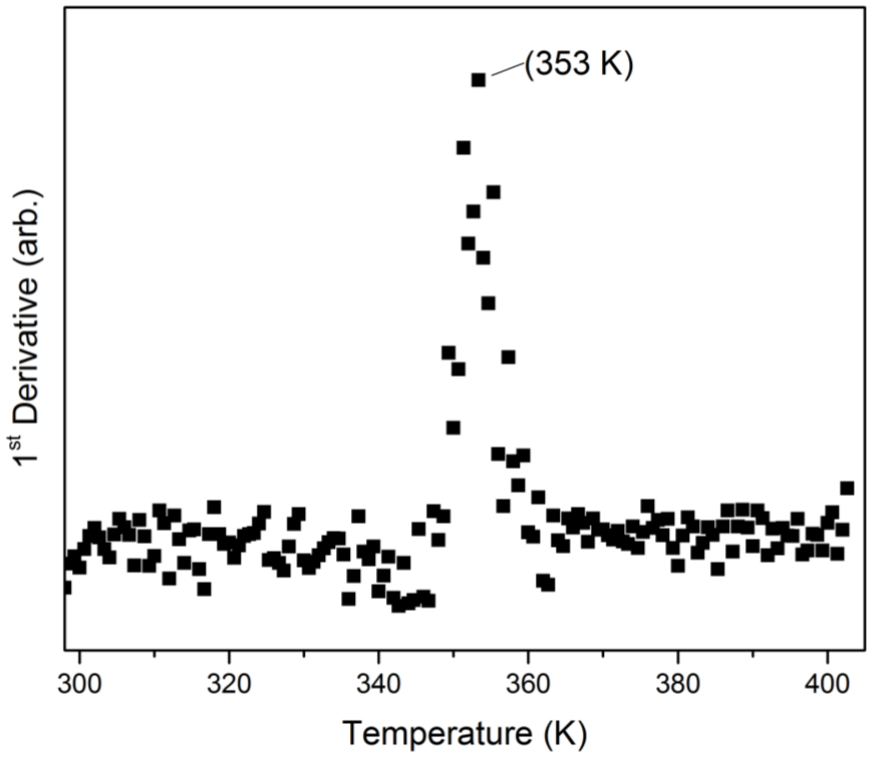

A.39: First derivative of the reflectivity measurements to determine $T_{1/2}$ of the cooling cycle for **2-thin**.

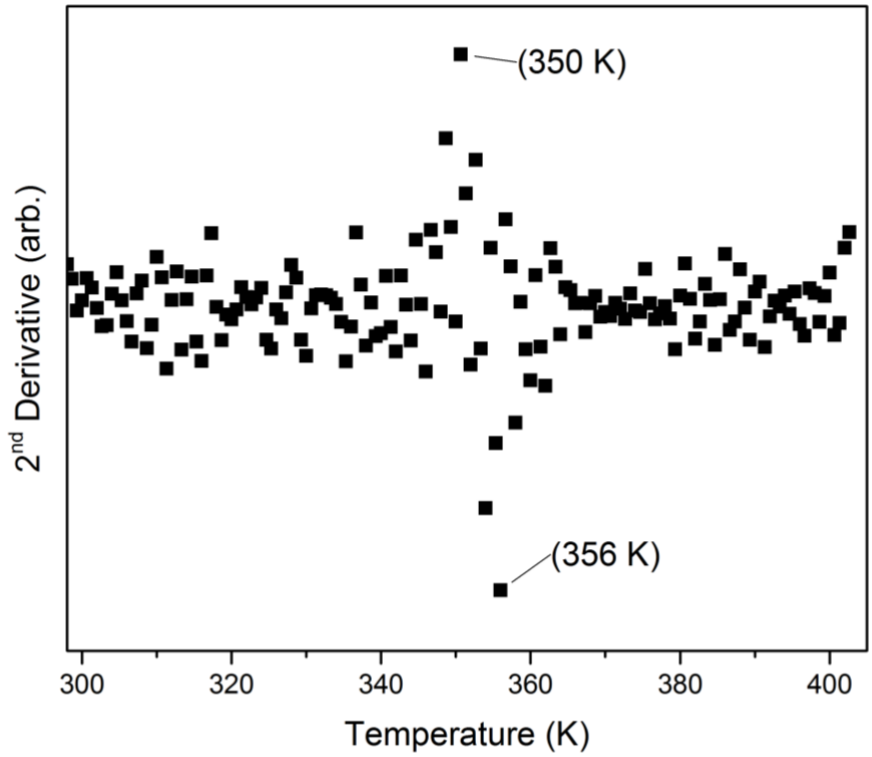

A.40: Second derivative of the reflectivity measurements to determine the smoothness of the transition of the cooling cycle for **2-thin**.

10.3. Section 8

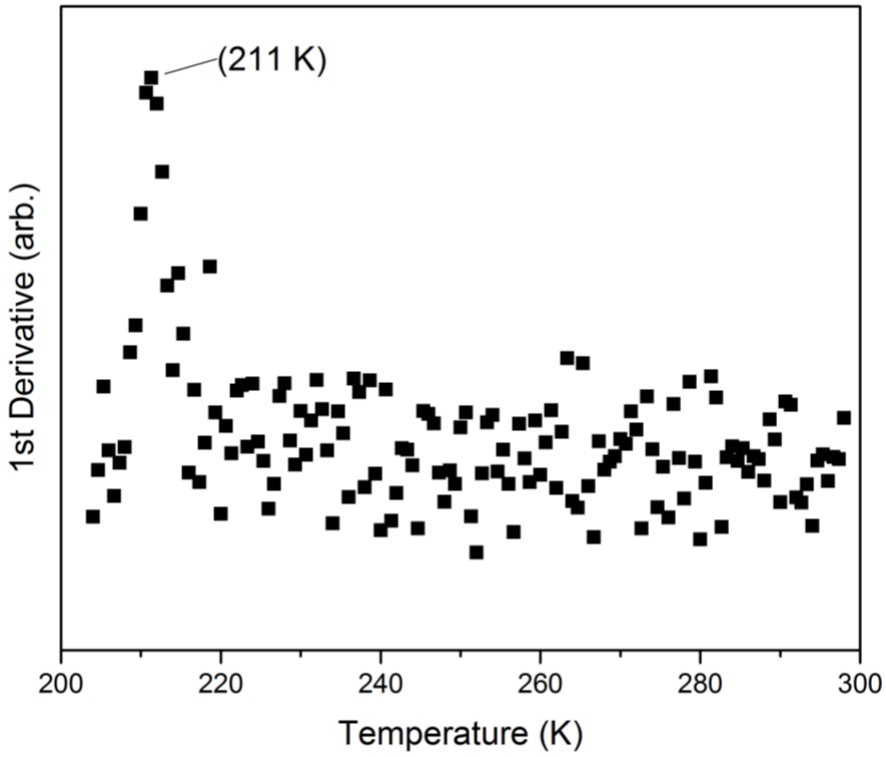

A.41: First derivative of the reflectivity measurements to determine $T_{1/2}$ of the heating cycle for **3-sol**.

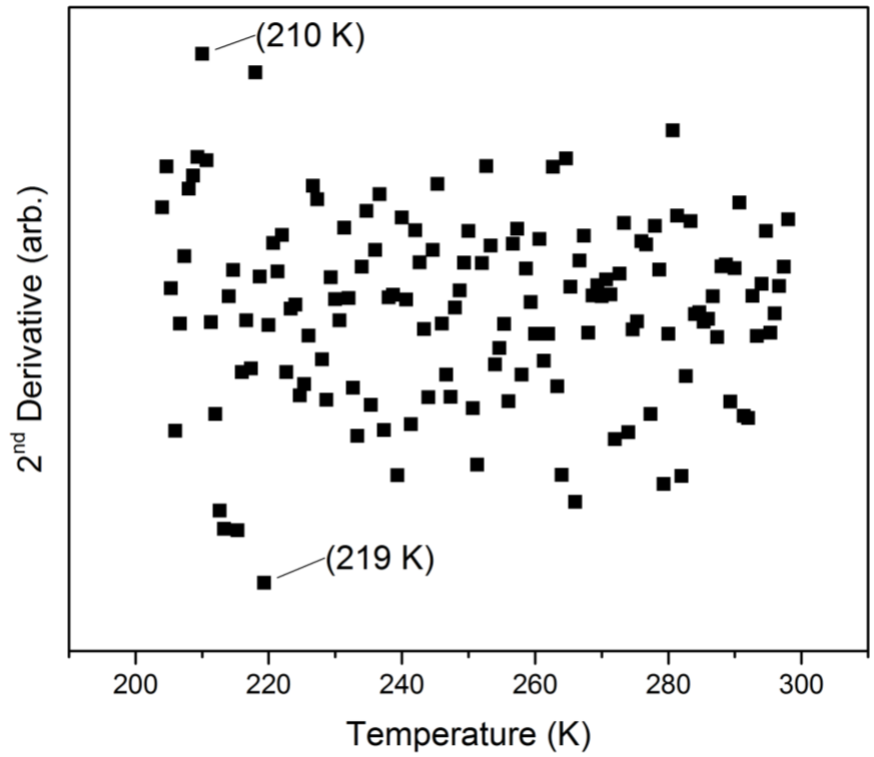

A.42: Second derivative of the reflectivity measurements to determine the smoothness of the transition of the heating cycle for **3-sol**.

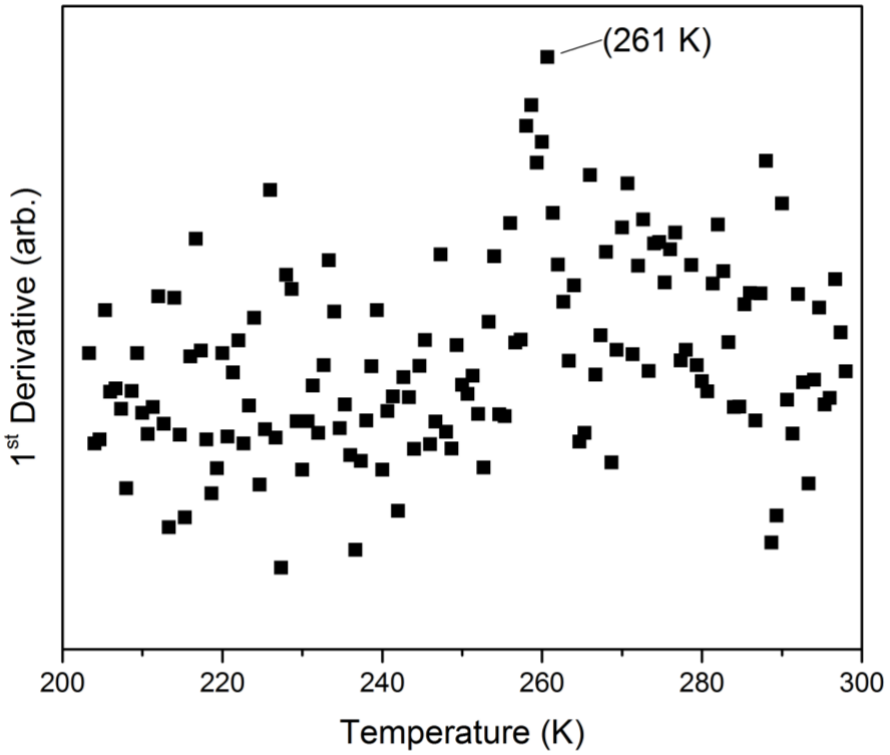

A.43: First derivative of the reflectivity measurements to determine $T_{1/2}$ of the cooling cycle for **3-sol**.

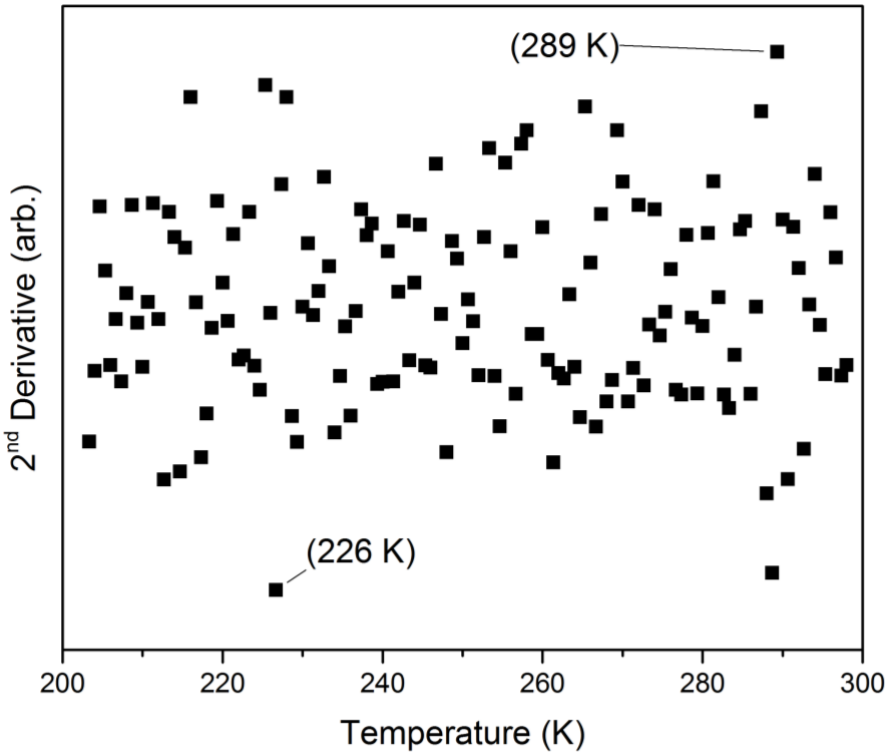

A.44: Second derivative of the reflectivity measurements to determine the smoothness of the transition of the cooling cycle for **3-sol**.

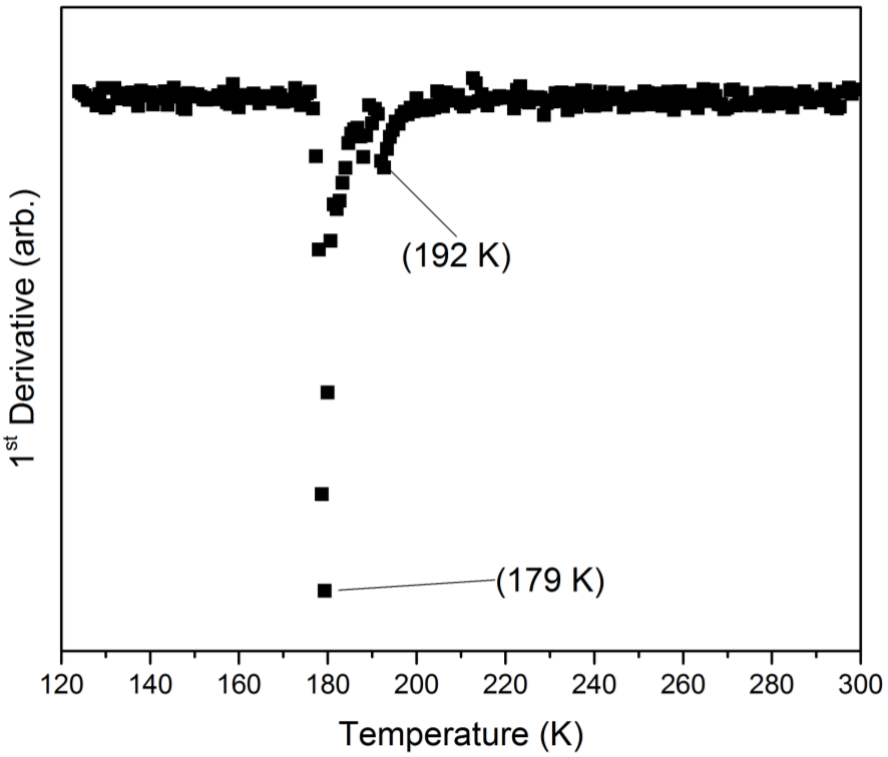

A.45: First derivative of the reflectivity measurements to determine $T_{1/2}$ of the heating cycle for **3-direct**.

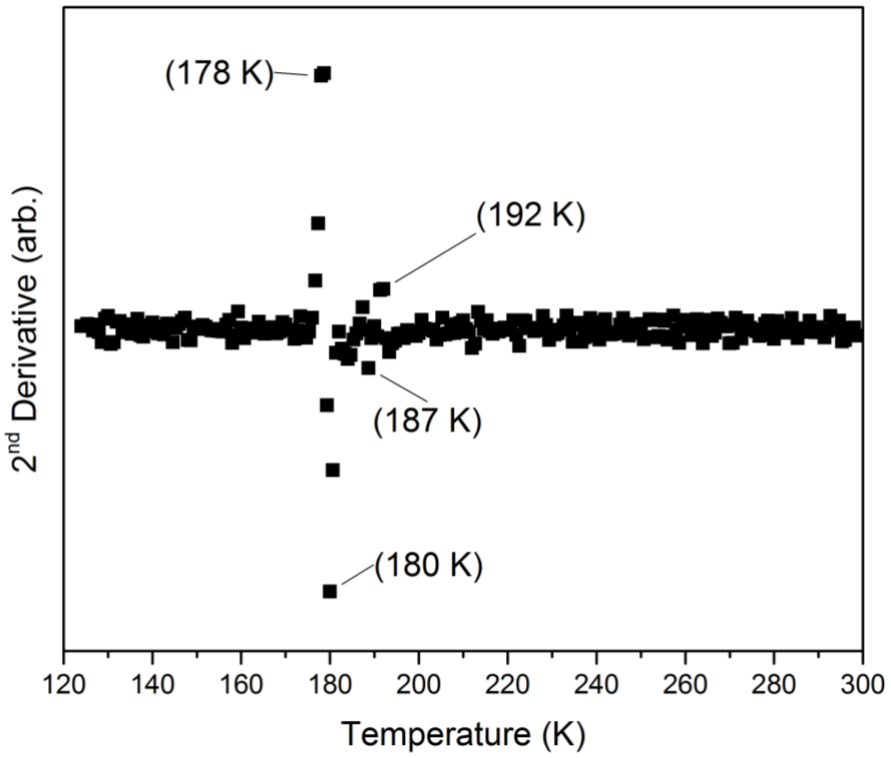

A.46: Second derivative of the reflectivity measurements to determine the smoothness of the transition of the heating cycle for **3-direct**.

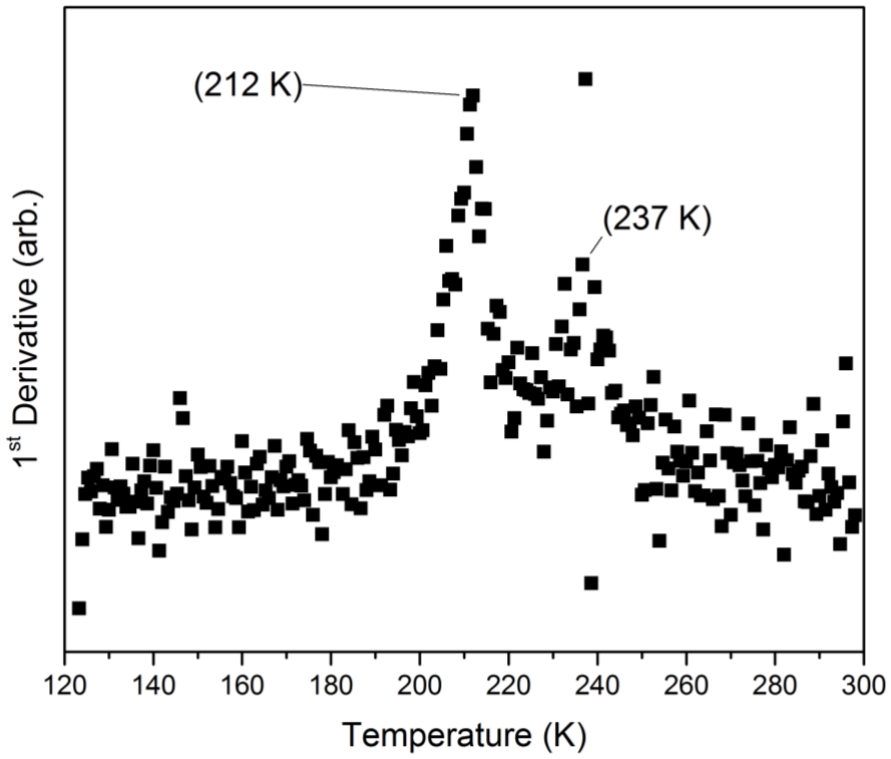

A.47: First derivative of the reflectivity measurements to determine $T_{1/2}$ of the cooling cycle for **3-direct**.

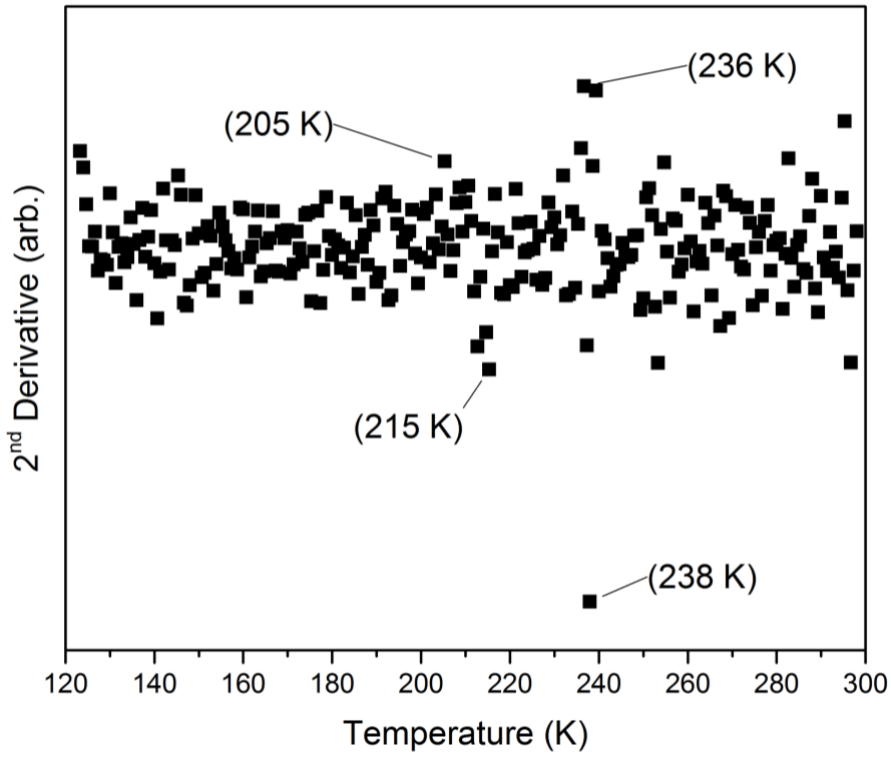

A.48: Second derivative of the reflectivity measurements to determine the smoothness of the transition of the cooling cycle for **3-direct**.

11. References

1 W. Nicolazzi and A. Bousseksou, *Comptes Rendus Chim.*, 2018, **21**, 1060–1074.

2 G. Molnár, M. Mikolasek, K. Ridier, A. Fahs, W. Nicolazzi and A. Bousseksou, *Ann. Phys.*, 2019, **531**, 1900076.

3 P. Gütlich, Y. Garcia and H. A. Goodwin, *Chem. Soc. Rev.*, 2000, **29**, 419–427.

4 P. Gütlich and H. A. Goodwin, 2012, pp. 1–47.

5 C. Enachescu and W. Nicolazzi, *Comptes Rendus Chim.*, 2018, **21**, 1179–1195.

6 S. Brooker, *Chem. Soc. Rev.*, 2015, **44**, 2880–2892.

7 O. Roubeau, *Chem. - A Eur. J.*, 2012, **18**, 15230–15244.

8 G. Aromí, L. A. Barrios, O. Roubeau and P. Gamez, *Coord. Chem. Rev.*, 2011, **255**, 485–546.

9 Y. Garcia, V. Niel, M. C. Muñoz and J. A. Real, pp. 229–257.

10 A. Michalowicz, J. Moscovici, B. Ducourant, D. Cracco and O. Kahn, *EXAFS and X-ray Powder Diffraction Studies of the Spin Transition Molecular Materials [Fe(Htrz>2(trz)](BF4) and [Fe(Htrz)3](BF4)2*H20 (Htrz = 1,2,4-4J/-triazole; trz = 1,2,4-triazolato)*, 1995, vol. 7.

11 O. Kahn, *Science (80-.).*, 1998, **279**, 44–48.

12 L. G. Lavrenova and O. G. Shakirova, *Eur. J. Inorg. Chem.*, 2013, **2013**, 670–682.

13 O. Kahn, J. Kröber and C. Jay, *Adv. Mater.*, 1992, **4**, 718–728.

14 P. Gamez, J. S. Costa, M. Quesada and G. Aromí, *Dalt. Trans.*, 2009, 7845.

15 M. Cavallini, *Phys. Chem. Chem. Phys.*, 2012, **14**, 11867.

16 J.-F. Létard, P. Guionneau and L. Goux-Capes, in *Spin Crossover in Transition Metal Compounds III*, Springer-Verlag, Berlin/Heidelberg, pp. 221–249.

17 L. C. Damonte, L. A. Mendoza Zélis, B. Marí Soucase and M. A. Hernández Fenollosa, *Powder Technol.*, 2004, **148**, 15–19.

18 K. Cho, H. Chang, D. S. Kil, B.-G. Kim and H. D. Jang, *J. Ind. Eng. Chem.*, 2009, **15**, 243–246.

19 N. B. Lihitkar, M. K. Abyaneh, V. Samuel, R. Pasricha, S. W. Gosavi and S. K. Kulkarni, *J. Colloid Interface Sci.*, 2007, **314**, 310–316.

20 N. Tsuchiya, A. Tsukamoto, T. Ohshita, T. Isobe, M. Senna, N. Yoshioka and H. Inoue, *Solid State Sci.*, 2001, **3**, 705–714.

21 E. W. Müller, H. Spiering and P. Gütlich, *Chem. Phys. Lett.*, 1982, **93**, 567–571.

22 J. H. Askew and H. J. Shepherd, *Chem. Commun.*, 2017, **54**, 180–183.

23 L. Salmon and L. Catala, *Comptes Rendus Chim.*, 2018, **21**, 1230–1269.

24 P. Durand, S. Pillet, E.-E. Bendeif, C. Carteret, M. Bouazaoui, H. El Hamzaoui, B. Capoen, L. Salmon, S. Hébert, J. Ghanbaja, L. Aranda and D. Schaniel, *J. Mater. Chem. C*, 2013, **1**, 1933.

25 A. Tissot, X. Kesse, S. Giannopoulou, I. Stenger, L. Binet, E. Rivière and C. Serre, *Chem. Commun.*, 2019, **55**, 194–197.

26 T. Forestier, S. Mornet, N. Daro, T. Nishihara, S. Mouri, K. Tanaka, O. Fouché, E. Freysz and J.-F. Létard, *Chem. Commun.*, 2008, 4327.

27 E. Coronado, J. R. Galán-Mascarós, M. Monrabal-Capilla, J. García-Martínez and P. Pardo-Ibáñez, *Adv. Mater.*, 2007, **19**, 1359–1361.

28 Y.-H. Luo, Q.-L. Liu, L.-J. Yang, Y. Sun, J.-W. Wang, C.-Q. You and B.-W. Sun, *J. Mater. Chem. C*, 2016, **4**, 8061–8069.

29 C. Göbel, C. Hils, M. Drechsler, D. Baabe, A. Greiner, H. Schmalz and B. Weber, *Angew. Chemie Int. Ed.*, 2020, **59**, 5765–5770.

30 N. Daro, L. Moulet, N. Penin, N. Paradis, J.-F. Létard, E. Lebraud, S. Buffière, G. Chastanet and P. Guionneau, *Materials (Basel).*, 2017, **10**, 60.

31 H. Peng, G. Molnár, L. Salmon and A. Bousseksou, *Chem. Commun.*, 2015, **51**, 9346–9349.

32 K. Robertson, P.-B. Flandrin, H. J. Shepherd and C. C. Wilson, *[Fe(Htrz)2(trz)](BF4) nanoparticle production in a milli-scale segmented flow crystalliser*, vol. 35.

33 T. Mallah and M. Cavallini, *Comptes Rendus Chim.*, 2018, **21**, 1270–1286.

34 G. Félix, W. Nicolazzi, L. Salmon, G. Molnár, M. Perrier, G. Maurin, J. Larionova, J. Long, Y. Guari and A. Bousseksou, *Phys. Rev. Lett.*, 2013, **110**, 235701.

35 A. Nakamoto, Y. Ono, N. Kojima, D. Matsumura and T. Yokoyama, *Chem. Lett.*, 2003, **32**, 336–337.

36 N. G. White, H. L. C. Feltham, C. Gandolfi, M. Albrecht and S. Brooker, *Dalt. Trans.*, 2010, **39**, 3751.

37 D. Tanaka, N. Aketa, H. Tanaka, T. Tamaki, T. Inose, T. Akai, H. Toyama, O. Sakata, H. Tajiri and T. Ogawa, *Chem. Commun.*, 2014, **50**, 10074–10077.

38 M. Cavallini, I. Bergenti, S. Milita, J. C. Kengne, D. Gentili, G. Ruani, I. Salitros, V. Meded and M. Ruben, *Langmuir*, 2011, **27**, 4076–4081.

39 H. Soyer, C. Mingotaud, M.-L. Boillot and P. Delhaes, *Langmuir*, 1998, **14**, 5890–5895.

40 H. Naggert, A. Bannwarth, S. Chemnitz, T. von Hofe, E. Quandt and F. Tuczek, *Dalt.*

Trans., 2011, **40**, 6364.

41 J. Zasadzinski, R. Viswanathan, L. Madsen, J. Garnaes and D. Schwartz, *Science (80-.).*, 1994, **263**, 1726–1733.

42 O. Roubeau, B. Agricole, R. Clérac and S. Ravaine, , DOI:10.1021/jp048194i.

43 J. A. Kitchen, N. G. White, C. Gandolfi, M. Albrecht, G. N. L. Jameson, J. L. Tallon and S. Brooker, *Chem. Commun.*, 2010, **46**, 6464.

44 S. A. Jenekhe, *Polym. Eng. Sci.*, 1983, **23**, 830–834.

45 M. Matsuda and H. Tajima, *Chem. Lett.*, 2007, **36**, 700–701.

46 A. Tissot, J.-F. Bardeau, E. Rivière, F. Brisset and M.-L. Boillot, *Dalt. Trans.*, 2010, **39**, 7806.

47 G. Félix, K. Abdul-Kader, T. Mahfoud, I. A. Gural'skiy, W. Nicolazzi, L. Salmon, G. Molnár and A. Bousseksou, *J. Am. Chem. Soc.*, 2011, **133**, 15342–15345.

48 T. Hochdörffer, J. A. Wolny, L. Scherthan, H. Auerbach, S. Sakshath, A. Omlor, S. Wolff, H.-C. Wille, I. Sergeev and V. Schünemann, *Hyperfine Interact.*, 2019, **240**, 116.

49 K. Kuroiwa, T. Shibata, S. Sasaki, M. Ohba, A. Takahara, T. Kunitake and N. Kimizuka, *J. Polym. Sci. Part A Polym. Chem.*, 2006, **44**, 5192–5202.

50 C. K. Knox and G. A. Voth, *J. Phys. Chem. B*, 2010, **114**, 3205–3218.

51 S. Cobo, G. Molnár, J. A. Real and A. Bousseksou, *Angew. Chemie*, 2006, **118**, 5918–5921.

52 C. Bartual-Murgui, L. Salmon, A. Akou, C. Thibault, G. Molnár, T. Mahfoud, Z. Sekkat, J. A. Real and A. Bousseksou, *New J. Chem.*, 2011, **35**, 2089.

53 M. Ohba, K. Yoneda, G. Agustí, M. C. Muñoz, A. B. Gaspar, J. A. Real, M. Yamasaki, H. Ando, Y. Nakao, S. Sakaki and S. Kitagawa, *Angew. Chemie Int. Ed.*, 2009, **48**, 4767–4771.

54 C. Bartual-Murgui, A. Akou, C. Thibault, G. Molnár, C. Vieu, L. Salmon and A. Bousseksou, *J. Mater. Chem. C*, 2015, **3**, 1277–1285.

55 J. Sanchez Costa, *Comptes Rendus Chim.*, 2018, **21**, 1121–1132.

56 R. R. Jones, D. C. Hooper, L. Zhang, D. Wolverson and V. K. Valev, *Nanoscale Res. Lett.*, 2019, **14**, 231.

57 E. Collet and P. Guionneau, *Comptes Rendus Chim.*, 2018, **21**, 1133–1151.

58 L. E. Smart and E. A. Moore, *Solid State Chemistry : An Introduction*, CRC Press LLC, Fourth Edi., 2012.

59 V. A. V. L. G. Lavrenova, O. G. Shakirova, V. N. Ikorskii and and S. V. L. L. A.

Sheludyakova, *Russ. J. Coord. Chem.*, 2003, **29**, 22–27.

60 J. Kröber, J.-P. Audiére, R. Claude, E. Codjovi, O. Kahn, J. G. Haasnoot, F. Groliére, C. Jay, A. Bousseksou, J. Linares, F. Varret and A. Gonthier-Vassal, *Spin Transitions and Thermal Hystereses in the Molecular-Based Materials [Fe(Htrz)2(trz)](BF4) and [Fe(Htrz)3](BF4)2*H20 (Htrz = 1,2,4-4/f-triazole; trz = 1,2,4-triazolato)*, 1994, vol. 6.

61 A. Grosjean, P. Négrier, P. Bordet, C. Etrillard, D. Mondieig, S. Pechev, E. Lebraud, J.-F. Létard and P. Guionneau, *Eur. J. Inorg. Chem.*, 2013, **2013**, 796–802.

62 A. Urakawa, W. Van Beek, M. Monrabal-Capilla, J. R. Galán-Mascarós, L. Palin and M. Milanesio, *J. Phys. Chem. C*, 2011, **115**, 1323–1329.

63 V. A. Varnek and L. G. Lavrenova, *J. Struct. Chem.*, 1995, **36**, 104–111.

64 J. H. Askew, D. M. Pickup, G. O. Lloyd, A. V. Chadwick and H. J. Shepherd, *Magnetochemistry*, 2020, **6**, 44.